Excited State Dynamics of

First-Row Transition Metal Oxide Clusters

by

Jacob Michael Garcia

A Dissertation Presented in Partial Fulfillment
of the Requirements for the Degree
Doctor of Philosophy

Approved October 2021 by the
Graduate Supervisory Committee:

Scott G. Sayres, Chair
Jeffery Yarger
Timothy Steimle

ARIZONA STATE UNIVERSITY

December 2021

ABSTRACT

Transition metal oxides are used for numerous applications, including

semiconductors, batteries, solar cells, catalysis, magnetic devices, and are commonly

observed in interstellar media. However, the atomic-scale properties which dictate the

overall bulk material activity is still lacking fundamental details. Most importantly, how

the electron shells of metals and O atoms mix is inherently significant to reactivity. This

thesis compares the binding and excited state properties of highly correlated first-row

transition metal oxides using four separate transition metal systems of Ti, Cr, Fe and Ni.

Laser ablation coupled with femtosecond pump-probe spectroscopy is utilized to resolve

the time-dependent excited state relaxation dynamics of atomically precise neutral

clusters following 400 nm (3.1 eV) photoexcitation. All transition metal oxides form

unique stable stoichiometries with excited state dynamics that evolve due to oxidation,

size, or geometry. Theoretical calculations assist in experimental analysis, showing

correlations between charge transfer characteristics, electron and hole localization, and

magnetic properties to the experimentally determined excited state lifetimes.

This thesis finds that neutral Ti and Cr form stable stoichiometries of MO_2 (M =

Ti, Cr) which easily lose up to two O atoms, while neutral Fe and Ni primarily form MO

(M = Fe, Ni) geometries with suboxides also produced. TiO_2 clusters possess excited

state lifetimes that increase with additional cluster units to ~600 fs, owing to a larger

delocalization of excited charge carriers with cluster size. CrO_2 clusters show a unique

inversed metallic behavior with O content, where the fast (~30 fs) metallic relaxation

component associated with electron scattering increases with higher O content, connected

to the percent of ligand-to-metal charge transfer (LMCT) character and higher density of

states. FeO clusters show a decreased lifetime with size, reaching a plateau of ~150 fs at the size of $(FeO)_5$ related to the density of states as clusters form 3D geometries. Finally, neutral $(NiO)_n$ clusters all have similar fast lifetimes (~110 fs), with suboxides possessing unexpected electronic transitions involving s-orbitals, increasing excited state lifetimes up to 80% and causing long-lived states lasting over 2.5 ps. Similarities are drawn between each cluster system, providing valuable information about each metal oxide species and the evolution of excited state dynamics as a result of the occupied d-shell. The work presented within this thesis will lead to novel materials of increased reactivity while facilitating a deeper fundamental understanding on the effect of electron interactions on chemical properties.

ACKNOWLEDGMENTS

I knew that obtaining a doctorate degree would be one of the larger challenges in my life, and not much could have prepared me for this task. There were months and years of joy, exhilarating scientific exploration and countless successes along the way. However, just as there are ups, there are equal times of low. To say this was a challenge does not give the last 5+ years of my life any credit. It is partially thanks to those around me that I was able to persevere, and I wouldn't change a single step in my journey.

After deciding that a life of research was for me, I made the jump over to Phoenix from Colorado, partially to escape the cold and partially to explore a new city. Soon after starting the program at ASU, I randomly attended a talk from Dr. Scott Sayres. A young and passionate scientist, he drew me into his lab and became my mentor along with Jeff Yarger and Tim Steimle. Through the years, they have taught me many things, helped me to stay motivated, and provided me some of the freedoms to make ASU my home. Scott and I have published several papers in reputable journals together and have had many things to celebrate over the years. I would not have become the successful physical chemist that I am today without him, and I am proud to be the first full PhD to graduate from his lab. I know there are many more successes in store for the both of us. Additionally, starting in Sayres' lab alongside Lauren and Ryan, I couldn't have asked for a better team. We pushed each other and supported one another through many obstacles and situations. Best of luck to the both of you going forward. I know you'll reach your goals and end up in the place that makes you happiest.

I also must acknowledge some of the people that got me to pursue my PhD in the first place, such as my undergraduate professor, Surendra N. Mahapatro, who got me

involved in the Western Alliance to Expand Student Opportunities (WAESO) and fueled my passion for research along-side my Biochemistry advisor, Stacy Chamberlin. Through them and the WAESO program, I found a passion for conducting scientific research. Additionally, it is through WAESO that I was led to ASU, inevitably granted a two-year fellowship, and provided several outlets to present my research at competitive conferences, winning numerous awards. I feel that it is due to them, that I was able to excel and standout to my potential future employers.

Also, my family has constantly supported me and helped shape me into the individual that I am today. Whether through good or bad times, I have learned to be dedicated, stubborn, inquisitive, patient, skeptical, and strategic with my endeavors. Shaun, Nic and Marc, thank you for the lessons you have provided me and experiences which helped shape me into the scientist that I am today. To my parents, Carol and Rich, thank you for the unconditional support and belief in my abilities. On some of the more difficult days, it always helps to have someone to reach out to for kind words and uplifting thoughts. Thank you!!

My friends have supplied enormous support, and without them I fear that I would not have made it through this experience successfully. As soon as I joined the program, I felt greeted by people ready to be friends and cultivate a community. By the time I was in my third year of the program, I was living in a supportive environment that provided healthy outlets to keep me focused on the program. Although I was almost constantly annoyed by living with an engaged (and eventually married) couple, it was a great environment that I wouldn't change. Alex and Emily, thank you for years of friendship, a clean home, and always telling embarrassing stories. For all the other numerous friends

(Veto, Matt, Mongoose, Nate, the Shore-Person, In-Hye, Edgar, Berta, John, Zach, Aerial, Kirstie, Will, MoMac and many others), you make all of this worth it. Keep killin' it and I'll be seeing you all again soon.

During the PhD program, I'll say that it was tough staying in lab all day, desperately trying to collect data. I found solace in being physically active, often needing to break out of the lab to go for a walk, spend an hour at the gym, and then continue to tackle my experiments, aligning laser pulses for hours on end. Changing one pulse generator for hours, hoping to see a single spike of signal on an oscilloscope... Those nights I would close my eyes and still see the static on a blank screen! I began brewing beer more casually, trying to find expensive whiskeys, joined the Graduate and Professional Student Association (GPSA), founded the Chemical and Biological Sciences Society (CaBSS), and helped start the School of Molecular Sciences Graduate Student Council (SMS-GSC). I have even played numerous intramural sports, leading to tearing my ACL the first year of my PhD career but also a championship volleyball victory. These activities gave me deeper purpose in an environment I felt like I would never conquer.

Nevertheless, for better or for worse, it seems all chapters in life must come to an end. I eagerly place my time at ASU behind me and move forward with the lessons and experiences that I have gained. Thank you to everyone that helped me to get here and the lessons along the way. Cheers!

TABLE OF CONTENTS

LIST OF TABLES

LIST OF FIGURES

CHAPTER 1

INTRODUCTION

1.1 Cluster Chemistry

Clusters are broadly defined as a collection of atoms bound together, with unique properties that change with the addition or subtraction of a single atom. As early as 1984, the importance of clusters was demonstrated by the ability to resolve Na clusters of specific composition with uniquely high stability.[1] It was concluded that it is more appropriate to consider the valence electrons as evenly distributed across the surface of the cluster rather than isolated to a specific atomic orbital, and clusters with filled shells should exhibit enhanced stability.[1,2] This became well known as the jellium model, describing closed shell clusters with enhanced stability as "magic clusters", leading to the growth of the field and countless investigations into molecular physics.[2]

Metal oxide materials are commonly used in industrial chemical processes, have high reactivity and unique properties, but typically suffer from a lack of fundamental molecular understanding. Bulk systems have been examined in detail, highlighting the reliance on surface structures and atomic defects.[3,4] At the cluster scale, where every atom counts, the factors which affect bulk reactivity and the active defect sites may be examined in more detail. Examination of transition metal oxide clusters provides a unique and exciting window to understand numerous intricate processes which dictate the reactivity and dynamics of commonly used bulk-scale materials.[5] In addition, at this ultimate size limit, special reactivities and magnetic properties of atomically precise materials may be resolved. The reactivity of metal oxide clusters have been summarized in detail,[6] highlighting their dynamics and especially high reactivity,[7] potentially aiding

1

in numerous mechanisms such as acid dissolution, solvation, proton transfer, and more.[8] The specific properties of transition metal oxides and the techniques used to interrogate clusters is outlined in this thesis, leading to crucial fundamental information and deeper insights into the overall reactivity of transition metal oxides.

1.1.1 Electronic Properties – From Clusters to Bulk

Transition metal oxide clusters are highly useful for studying the fundamental interactions of strongly correlated materials, or systems which effectively share electronic properties with spin, orbital, lattice and magnetic properties.[9] Upon photoexcitation exceeding the optical gap, an exciton is produced, or electron-hole pair, that can recombine through non-radiative processes such as internal conversion or relax through electron scattering.[10] In strongly correlated materials, such as metal oxides, charge carriers are coupled to lattice vibrations to form polarons, which serve to trap mobile carriers by reducing their mobility and photoconversion. Polaron formation is affected by the local geometry of the material, spin, and lattice parameters which may be altered by introducing defects[10] but the magnitude of change is not fully understood. The effect of defect sites and mechanisms of charge carrier dynamics have been discussed,[3,4,11] but require further molecular-level insights. Ultimately, reactivity and industrially useful charge transfer characteristics are governed by charge carrier recombination, which may be altered by single atomic changes to a material.

Transition metals bind to oxygen through strong interactions between the d-orbitals of the metal and p-orbitals of the O atoms.[12] Oxygen typically withdraws two electrons, leaving the metal with a formal oxidation state of +2. Therefore, the reactive valence band of transition metal oxides typically consists of O-2p and metal-d electrons,

with the excited electron transitions becoming extremely important to the overall reaction dynamics. At the molecular size of clusters, excited electron energy levels are discrete and well-separated. The energy around the highest occupied molecular orbital (HOMO) and the lowest unoccupied molecular orbital (LUMO), or HOMO-LUMO gap, is therefore quantized with the number of energy levels, or density of states, above this region becoming important to the overall excitation and ionization of clusters. Due to their size, the ground state geometries and excited states of clusters as they evolve to the bulk scale are computationally feasible to determine, providing valuable bulk-scale insights.

At the molecular scale, the addition or removal of an O atom may result in structural rearrangement, a change in the number and distribution of energy levels above the HOMO-LUMO gap, and therefore change the overall electron properties. The metallicity and insulator-like properties of clusters have been discussed in detail,[13] which depends heavily on the cluster size, symmetry, gaps between energy levels near the fermi-energy, and other intramolecular electron properties such as spin. Although clusters have many unique characteristics, such as a well-defined density of states, they may also provide a window into the bulk effects caused by surface-level atomic vacancies, defect sites, and the evolution of nanoparticles towards bulk-scale reactivity.

Clusters are uniquely capable of being examined with atomic specificity, providing electronic properties that may be related to bulk-scale materials. Many techniques have been used for the measurement of energy levels of clusters, including photoelectron spectroscopy, IR spectroscopy, and other laser-based spectroscopic

techniques discussed in detail elsewhere.[2,13–15] This thesis utilizes a specific set of experimental methods briefly discussed in the following chapters.

1.2 Laser Techniques and Cluster Science

Light amplification by stimulated emission of radiation, also known as a laser, was first considered a "solution looking for a problem", but has since been utilized in virtually all realms of science.[16] The properties and physics of laser production have been reviewed in detail,[17] where the profile of the laser energy and pulse time becomes extremely important to light-matter interactions. The wavelength of light, also described as photon energy, will interact with a molecule or material surface, promoting the interacting species to a higher energy level with equal energy to the incident photon. The overlap of two or more laser pulses spatially and temporally can be utilized to create laser pulses of short duration and well-defined energy, further improving overall resolution. Due to the creation of lasers with specific energy and time profiles, the electronic properties of clusters and bulk-scale materials may be examined in high precision. Excited states may be resonantly accessed, and the control over reaction dynamics may be realized.

Laser-based techniques have continued to advance in the energy and time regime since its inception. With the production of a laser pulse with sufficient energy but of extremely short duration, the experimental resolution of molecular dynamics has drastically improved. On the attosecond to femtosecond timescale, electron motion may be visualized as temporal snapshots of electrons as they naturally move around a molecule. Ultrafast spectroscopy has used many techniques to resolve electronic motion

depending upon molecular size, the energy supplied to the environment, and numerous external interacting factors.

Gas-phase spectroscopy of neutral clusters provides a wealth of information, including their structures, size, geometry, electron dynamics, vibrational and rotational energy levels, catalytic properties, fragmentation patterns, and time-resolved dynamics.[8] Neutral cluster mass spectrometry has many advantages due to the ease of theoretical calculations in determining their electronic ground states, stable cluster geometry, and serve as better models for bulk materials. Mass spectrometry of neutral gas-phase clusters has emerged as an extremely fruitful technique for the production and analysis of cluster electron dynamics and is utilized within this thesis.

1.2.1 Mass Spectrometry

Numerous methods have been developed for the production of gas-phase clusters to study reactions with atomic specificity.[6] Typically, laser ablation is a common and very efficient process, where an incident laser pulse interacts with the surface of a material and causes atomization from the breaking of molecular bonds. The atoms then collide numerous times, nucleating and producing stable clusters. The introduction of a backing gas expands adiabatically into the ablation region and assists in cooling the clusters, where ablation results in a kinetically hot plasma. Helium gas is highly effective over other noble gases due to the thermal conductivity, which is much higher than other noble gases and aids the thermal cooling of metal plasmas.[18] The overall ablation and nucleation process results in the production of a wide distribution of ionized and neutral clusters, discussed in detail previously.[18]

Of particular importance to this thesis, neutral cluster mass spectrometry has been reviewed in detail, [19] showing the ability to do numerous experiments related to bulk-scale materials. For example, various metal clusters reacting under the presence of molecules such as O_2, CO_2, NO, H_2O, alcohols, and other hydrocarbons are well documented, showing enhanced reactivity and catslysis.[6] Specific to commonly used bulk-scale industrial materials and highlighted in this thesis is the production and analysis of neutral metal oxide clusters by using an ablation source under O_2 gas.

One of the most used methods of gas-phase cluster detection is time-of-flight mass spectrometry (TOF-MS), which separates molecular ions by the travel time to a detector. In these instances, the molecules or ions are given an electrostatic push of acceleration, which is felt the same on all gas-phase species as described in Chapter 2. However, depending on their mass and charge, they are accelerated to a different speed. Over a certain distance, these ions will separate in time and provide a spectrum based on the number of ions detected and the relative time in which they traveled to the detector after the initial acceleration.

TOF-MS utilizes high vacuum to minimize the number of external effects and isolate specific molecules. Ambient reactions can possess any number of factors, including atmospheric gases, light-triggered excitation, and side reactions with unknown materials. Under vacuum, these factors are greatly limited, leading to the isolated probing of molecules void of external effects. After the ablation process, clusters expand into the vacuum and may be considered isolated based upon the mean free path, or the average distance molecules travel prior to collision with another species. The mean free path can

be calculated using the pressure (ρ), temperature of the system (T), and molecular cross section (σ) shown in Equation 1.1.

$$\lambda = \frac{kT}{\sigma\rho\sqrt{2}} \qquad (1.1)$$

With "k" being the Boltzmann constant, sub-nm gas-phase molecules under high to ultrahigh vacuum (~7-8 x 10^{-7} Torr) typically have a λ greater than 600 m. With such a large distance before colliding with another species, this allows for the sufficient probing of molecules void of external reactions.

1.2.2 Ultrafast Pump-Probe Spectroscopy

The realm of ultrafast laser spectroscopy has seen tremendous growth as the world continues to push the boundaries of what atomic properties can be resolved. Most notably, with the use of femtosecond and attosecond laser pulses, the motion of electrons can be manipulated, and their mechanistic properties can be well understood. Where a single laser pulse of adequate energy may ionize a molecule through single or multiphoton excitation providing important structural information,[12,20] introducing a second laser pulse has numerous added advantages. Most-importantly, pump-probe spectroscopy allows for the visualization of intermediate excited energy levels by introducing a time-delayed secondary laser pulse, resolving time-dependent excited state properties.

As a bulk surface or molecule is excited, the electron is promoted to a higher energy level, leaving a void, or "hole", in the vacant location. The excited electron and hole, known as charge carriers, may behave separately, localize at different locations, and either remain separated or recombine through nonradiative mechanisms. Catalytic

activity and reactions mediated by electron excitation is ultimately dictated by charge

carrier dynamics, which depend on the ability to localize and recombine. In addition, if

the excited electron transitions from the ligand to the metal center, known as a ligand-to-

metal charge transfer (LMCT), and how strong the transition is, becomes highly

important to charge localization and recombination. Excitation of molecular-scale

clusters by a photon below the ionization energy may result in the change of molecular

geometry, spin flips, dissociation, nonradiative decay back to the ground state, and long-

lived charge separation.

Quantum confinement effects help describe the electrons of atoms and molecules

in terms of quantized energy levels, or potential energy surfaces, dependent on the

molecular bond length and total energy (Figure 1.1). As the probe pulse with finite

energy is delayed in time, the transient ionized population is dependent on the excited

state relaxation as the molecule traverses towards the ground state, dissociation, or

remains bound in an excited state of higher energy.
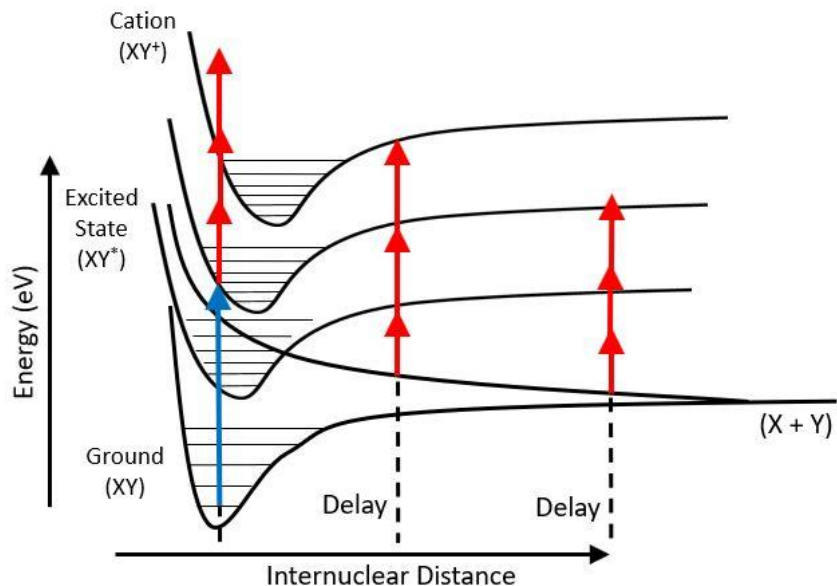
Figure 1.1: Representation of pump-probe spectroscopy using a single high-power pump photon (blue arrow) and low energy multiphoton (red arrows) probe excitation from the ground state potential energy well to an excited state of a molecule (XY).

As two laser pulses overlap temporally, multiphoton excitation takes place, with multiple photons of potentially different energy interacting with a material to eject an electron. Depending on the species being excited, ionization may occur for several fs to hundreds of ps after the pump pulse arrives. For pure noble gases such as argon, the overlap of two laser pulses will simply produce immediate multiphoton ionization over a period based on the interacting pulse widths. Ultimately, the resolution of the photoexcited properties is only limited by the temporal profile of the laser pulses, which is typically on the atto- or femtosecond timescale. A detailed explanation of femtosecond dynamics and pump-probe spectroscopy is detailed in other works.[14,15,21,22]

The excited states accessed by the pump laser pulse may possess different relaxation mechanisms dependent upon that molecular composition that accounts for the observed change in ion signal intensity. A response on the order of the interacting laser

9

pulses (10s of fs) may account for a portion of the transient signal, related to

instantaneous relaxation back to the ground state or to an excited state of lower energy

than the following probe pulse. A sub-ps relaxation may occur in materials that possess

charge carrier trapping, stable carrier localization, low density of states, and excited states

which survive for a long period prior to relaxation to the ground state. Highly stable

excited states may also be accessed which survive for many ps to nano- or microseconds.

A representative spectrum with long and short dynamics is show in Figure 1.2, with the

ion signal decaying as a result of the excited state relaxation.
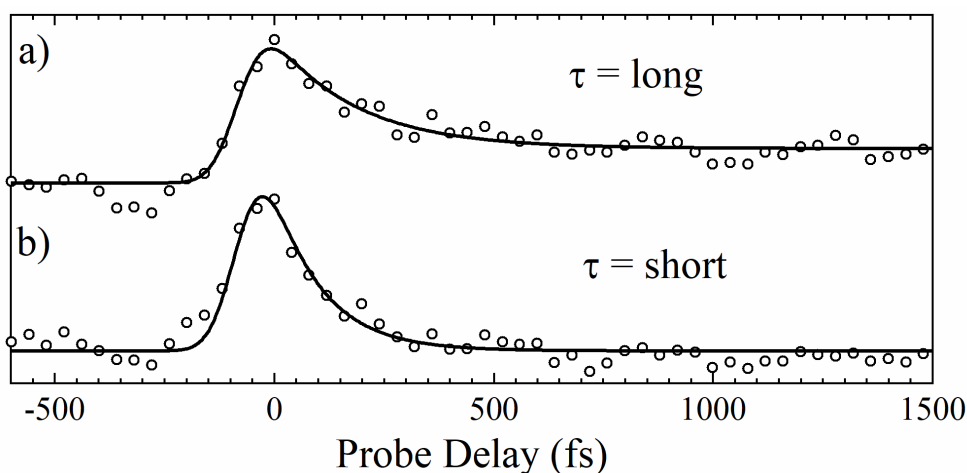
Figure 1.2: Representation of pump-probe dynamics showing a) long relaxation dynamics and b) short relaxation following photoexcitation.

The properties which affect excited state lifetimes are still not well understood,

which can be better resolved using cluster-based experiments. This thesis uniquely

possesses the ability to experimentally investigate atomically precise electron dynamics,

discussing the change in excited state relaxation as a result of atomic changes and

improving the overall interpretation of excited state mechanisms.

1.3 Cluster Electron Dynamics

  Photoexcitation is governed by quantum mechanical models used to describe proton transfer, electron transitions, and relaxation mechanisms described in detail previously.[22] Charge transfer in bulk materials depend heavily on the bandgap of the system, with insulators having a large energy separation of the valence (HOMO) and conduction (LUMO) band, or bandgap, whereas metals have little-to-no band separation. At the bulk scale, excited charge carriers (electrons and holes) may be dissipated throughout the material in the form of lattice vibrations (phonons) or similar charge carrier recombination. A common type of relaxation is electron-electron (e-e) scattering, or recombination of charge carriers via the movement of electrons through the bulk structure. In addition, Auger-type relaxation may occur, where electrons are removed from an inner molecular orbital, leaving a vacancy which is filled by a higher-level electron. Bulk material electron transport properties are reviewed in detail elsewhere,[23,24] and may be altered in order to change the insulating or metallic properties, through electron and hole doping.

  Ultrafast excited state dynamics are dominated by electron-electron and electron-phonon scattering, which may take place on the femtosecond to attosecond regime.[25,26] Although many bulk processes are not possible at the cluster scale, including relaxation through lattice vibrations, the descriptions which are related to metallic and insulator-like properties are maintained. For instance, the metallic behavior of e-e scattering typically takes place over 10's of fs, while charge carrier trapping in bulk insulators may last over ps to μs, also potentially occurring in isolated clusters. Upon excitation, clusters undergo similar mechanisms to redistribute the energy and return to the ground state, such as

intramolecular vibrational redistribution (IVR) or dissociation.[8] Excited, or "hot"

electrons, may behave quite differently and depend on the material and the number of

unoccupied d-electrons,[25,26] which becomes especially important in transition metal

oxides. However, the transition from atomic to bulk systems is not well understood and

the factors which affect charge carrier dynamics in bulk systems is lacking in

fundamental information.

This thesis aims to help bridge the gap between atomic and bulk-scale transition

metal oxide materials through the analysis of clusters with varying d-electron character as

the clusters change in size and oxidation. All experimental measurements described in

this thesis were carried out using a home-built time-of-flight mass spectrometer coupled

to an ultrafast pump-probe setup detailed in Chapter 2. The TOF-MS was used for

production and detection of gas-phase clusters while the pump-probe instrumentation was

used for the analysis of neutral cluster electron dynamics.

1.4 Dissertation Overview

This introduction discussed clusters with their application to bulk-scale materials

and showcased how lasers were adapted from their early history to their current

functionality of determining electron motion of materials in their native states. The

following chapters will highlight my recent findings on different first-row transition

metal oxide cluster systems and their experimentally resolved excited state lifetimes. In

addition, theoretical calculations will be briefly discussed to assist in the analysis of

select cluster systems.

Chapter 2 provides a description of the experimental apparatus used for the

production of gas-phase clusters and the determination of pump-probe transients. Time-

of-flight mass spectrometry is discussed in detail, including the specific parameters required to detect clusters in this system. Additionally, the analysis of pump-probe data specific to the systems discussed in this thesis is outlined, providing the instrumental response function necessary for determining the resolution of data.

Chapter 3 provides information on the pump-probe experiments of neutral iron oxide clusters. The neutral cluster distribution is discussed, pointing out the stable species which are produced from laser vaporization and their relative distributions. Following excitation from the 3.1 eV photon pump, excited state dynamics are resolved and analyzed as a function of oxidation and size, showing a heavy reliance on the cluster size and density of states.

Chapter 4 applies the same pump-probe technique to nickel oxides, showing the first stable neutral nickel oxide cluster distribution. The pump-probe transients of neutral nickel oxide clusters show several unique characteristics related to the density of states and strongly bound excited states which are accessed. Changes due to oxidation and size are analyzed with the assistance of DFT calculations, showing that the excited state lifetimes depend heavily on the nature of the photoexcited transition.

Chapter 5 resolves the ultrafast dynamics of titanium oxide clusters. The neutral clusters produced in the molecular beam are briefly analyzed, and the experimental transients are discussed in detail in concert with DFT calculations. The relation between the electronic shells, size, oxidation, and charge carrier dynamics is discussed. Unique to this system, a clear change from closed- to open-shell electron configurations is shown, which heavily influences electron dynamics. Additionally, the change in the overall LMCT character is related to the photoexcited cluster lifetimes.

13

Chapter 6 provides a discussion on chromium oxide clusters, their neutral cluster distribution, and the effects of these cluster's excited state dynamics as a function of size and oxidation. Interestingly, these clusters show a special metallic character which is related to the LMCT character resolved using DFT calculations. The unique electron configurations and spin states of chromium as they bind with oxygen is discussed, showing unusual changes due to oxidation.

Finally, Chapter 7 concludes this dissertation and offers future outlooks and potential applications. The transition metal oxides discuss in this thesis are touched upon, relating the systems and their unique characteristics. The similarities and differences between each transition metal oxide system are examined and related to the d-shell electron configurations of the specific metal. The important characteristics of their strongly correlated bonding to oxygen and their potential implications on catalytic properties is resolved.

CHAPTER 2

EXPERIMENTAL METHODS

2.1 Cluster Production and Detection

The production, detection, and analysis of laser ablated gas-phase clusters
required numerous systems working in-tandem. Neutral gas-phase cluster studies were
performed using a home-built Wiley-McLaren[27] type time-of-flight mass spectrometer
(TOF-MS) coupled to a fs laser system. Initial cluster production utilized the second
harmonic of a Nd:YAG (neodymium:yttrium aluminum garnet) laser (10 Hz, 8 ns, 532
nm) for ablation of the surface of a 0.25" metal rod which was set to rotate and
translationally move for ablation of a fresh surface with each laser shot. A DG535 pulse
generator was used to trigger the ablation laser, gas pulse valve (He, 100 psi), and TOF
grids in sync with the ionization laser (Figure 2.1). An external wave-form signal viewing
instrument (oscilloscope) was connected to the pulse generator to begin collecting
voltage data simultaneously to the triggered TOF pulse. Ionized species were accelerated
by a 10 µs high voltage (~4 kV) pulse on the TOF grids and focused onto the detector
using an Einzel lens with an applied variable voltage of 1.5-3.5 kV. The clusters were
separated in arrival time through a 1.1-meter-long field-free region and detected by a
chevron-type microchannel plate (MCP) detector. The observed signal was averaged over
~1000 shots, recorded by a digital oscilloscope, and transferred to a computer via an
IEEE-488 interface for analysis. The vacuum pressure of ~7.5 x 10^{-8} Torr was maintained
by three turbomolecular pumps.
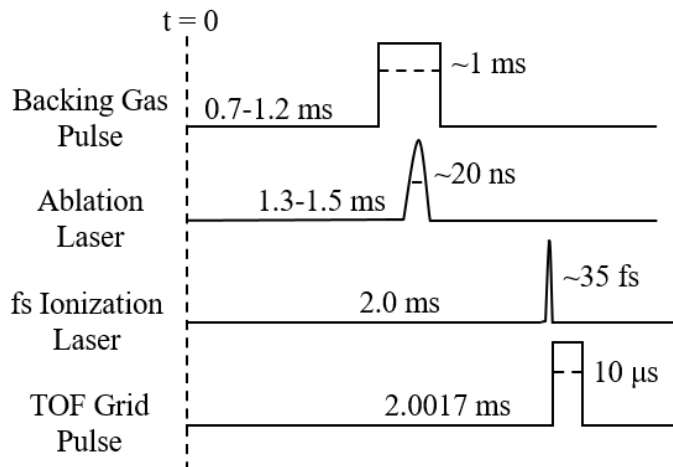
Figure 2.1: Timing diagram showing the delay between each laser, gas, and TOF acceleration pulse. Each data collection cycle occurs every 100 ms (10 Hz).

Ablation of the metal rod used a variable laser intensity of 50-300 mW with a focal spot size of ~4 μm and peak power of ~6 x 10^5 to ~4 x 10^6 W/cm^2 calculated using Equation 2.1 below, utilizing a 25 cm N-BK7 focal lens and 8 ns pulse width:

$$d = \frac{f\lambda}{\pi\omega\eta\sqrt{1 + \left(\frac{f\lambda}{\pi\omega^2\eta}\right)}}$$

(2.1)

Where "f" is the focal distance of the lens, λ is the wavelength, ω is the original beam diameter and η is the index of refraction (N-BK7 η = 1.515).

Instrumental calibration used standard metal rods (Mg, V, Fe) and mathematical calculations (detailed below) to standardize flight time (μs) to mass/charge (m/z). mMass (v5.5) was used to quadratic fit data and visualize scans. After the ablation process, the molecular plume is skimmed to a molecular beam diameter of 2 mm as the clusters move into the ionization and acceleration region of the instrument. Once in between the TOF grids, all positively charged species are accelerated and subsequently detected after passing through a series of regions on the way to the detector (Figure 2.2). An ionization laser is used for the detection of neutral cluster species described in section 2.2.

16
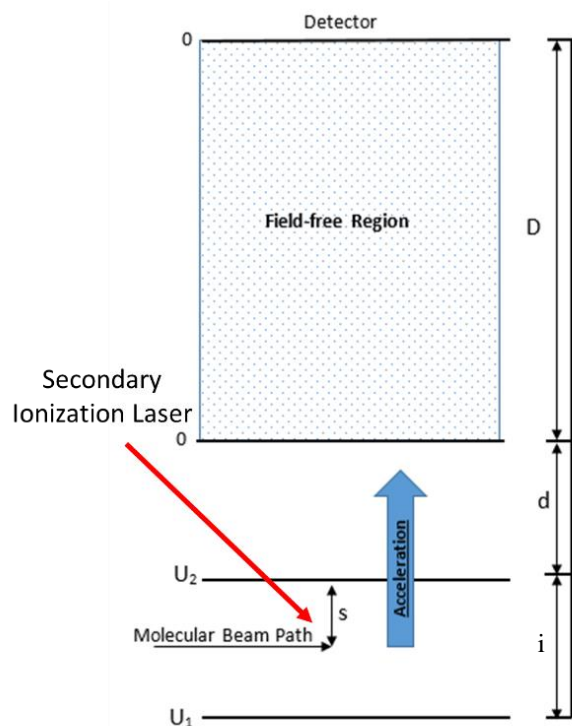
Figure 2.2: Time of flight region showing the separate locations ions will travel prior to detection, including the first ionization region (i), second region to the grounding plate (d), and field-free region (D). TOF grids (U_1, U_2 and 0) and the ionization laser path of the neutral cluster molecular beam are drawn.

All ions are provided a push of energy (U) related to their charge (q), distance from the molecular beam to the first charged plate (s), and distance of the second charged region (d) using Equation 2.2 below, where U_o is the initial energy, E_s is the electric field between the TOF plates U_1 and U_2, and E_d is the electric field strength between TOF plates U_2 and the grounding plate, 0:

$$U = U_o + qsE_s + qdE_d \qquad (2.2)$$

In my system, the distance s, d, and total field-free distance D of 1.25 cm, 2.5 cm, and 110 cm, respectively, is used for estimation of ion flight time. With a typical applied pulsed voltage of ~4800 V on U_1 and ~4600 V on U_2, the electric field strength E_s and E_d

17

becomes ~200 V/cm and ~1800 V/cm, respectively. U_o is assumed to be 0 due to the perpendicular path of the molecular beam to the induced ion flight path.

Flight time of all molecules was calculated theoretically using a series of equations discussed in detail previously.[27] The total flight time is a combination of three separate regions which ions travel through (Eq. 2.3). The total flight time is determined by the location of initial ionization to the first charged plate (T_s), the travel time through the second region which has a single charged plate and a grounded plate (T_d), and the final field-free region to the detector (T_D).

$$T(U_o, s) = T_s + T_d + T_D \tag{2.3}$$

Here, each region will have separate flight times which are calculated using Equations 2.4-2.6. In addition to the distance of each region, flight time is dependent upon mass (m) and charge (q) shown below:

$$T_s = 1.018 \left(\frac{2ms}{qE_s} \right)^{1/2} \tag{2.4}$$

$$T_d = 1.018 \frac{(2m)^{1/2}}{qE_d} \left(U^{1/2} - (qsE_s)^{1/2} \right) \tag{2.5}$$

$$T_D = 1.018(2m)^{1/2} \frac{D}{2U^{\frac{1}{2}}} \tag{2.6}$$

After obtaining the TOF spectrum of separate metal rods used for calibration, the spectra were overlayed, and the masses were calibrated using Equation 2.3. The calculated theoretical mass conversion was compared to the experimental values with excellent agreement, showing minor fluctuations due to experimental variables such as the total flight time, variable Einzel lens energy, and total distance of initial cluster ionization to the detector.
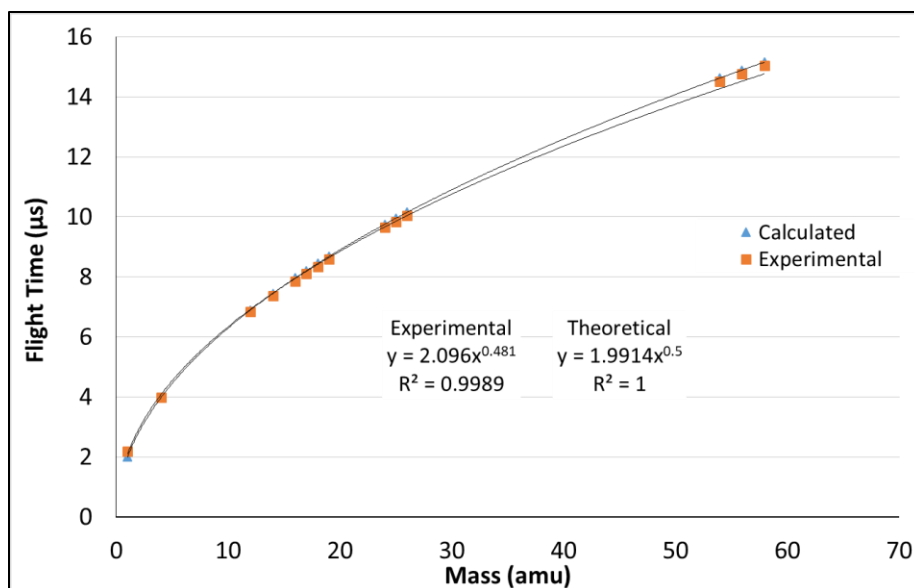
Figure 2.3: Calibration curves showing the theoretical (blue triangles) and experimental (orange squares) values from the flight time to mass of ions produced.

After calibration of the combined cation mass spectrum (Figure 2.4), the total spectrum

and the theoretical values were used for future mass calibrations.
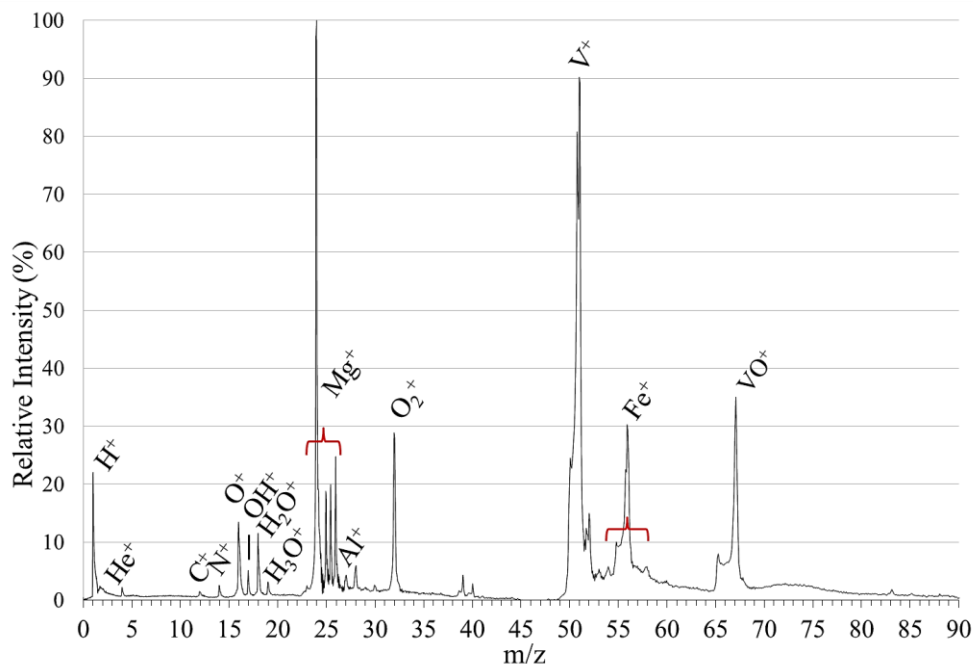
Figure 2.4: Calibrated mass spectrum showing the major ions used to calibrate the instrument. Each metal ion was produced from a separate ablation process.

19

Neutral gas-phase metal oxide clusters were produced using a synchronized pulse of 1-10% O_2 seeded in a helium carrier gas (100 psi) introduced directly over the metal rod. The plasma plume was confined to a 2 x 60 mm collision cell to aid in cluster formation. The ions produced through laser ablation were deflected by high voltage (200 V) placed on the skimmer, allowing only neutral clusters to enter the ionization region of the mass spectrometer. Neutral clusters were ionized through the interaction with a sequence of pulses from a Ti:Sapphire laser system (Spectra Physics Solstice Ace 1 kHz rep. rate, 800 nm central wavelength). The entire TOFMS instrument with optics and laser paths is shown in Figure 2.5.
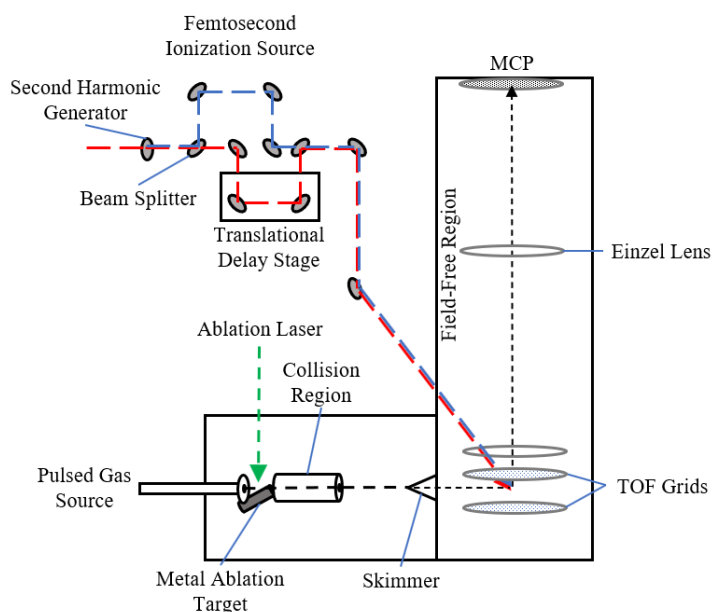
Figure 2.5: Schematic of the TOFMS instrument with ablation laser and fs pump-probe laser pulses drawn.

2.2 Pump Probe Transients

Excitation and ionization of the neutral cluster beam was performed by a series of fs laser pulses via a two-color pump-probe setup. 1 mJ of the fundamental 800 nm (1.55 eV) fs laser pulse was sent through a second harmonic doubling crystal (KDP crystal) to

generate the 400 nm (3.1 eV) pump beam. The two beams were separated using a dichroic mirror and the 800 nm laser pulse was sent through a programmable delay stage with steps as short as 0.1 μm before recombining with the 400 nm beam using another dichroic mirror (Figure 2.5). The 400 and 800 nm laser beams were focused through a 50 cm lens to reach intensities of up to 8.5 x 10^{14} and 2.4 x 10^{15} W/cm^2, respectively. Pump-probe transients were recorded by integrating the ion signal over an average of spectra at each time delay as the 800 nm beam was scanned over several ps.

An instrumental response function of ~35 fs was calculated using the FWHM from the Gaussian response of pure Ar gas (Figure 2.6).
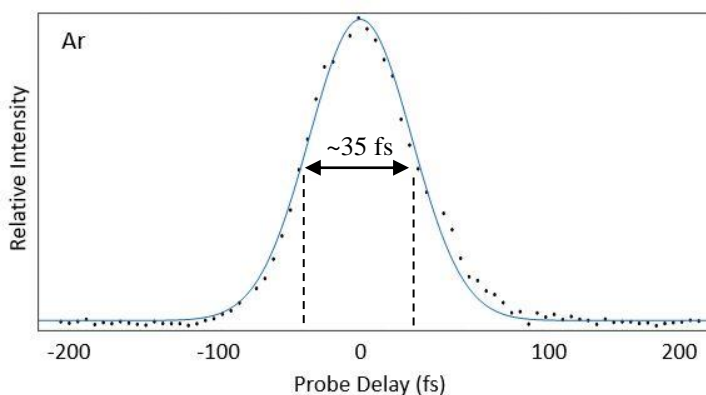
Figure 2.6: Pump-probe transient of pure Ar gas showing the change of ion intensity with probe delay.

Transient ion signals were analyzed using either the Ar or background O_2 signal. Using the fitting functions below (Eq. 2.7-2.9), a representative pump-probe scan (Figure 2.7) shows the change in ion signal with probe delay, highlighting the separate relaxation mechanisms.
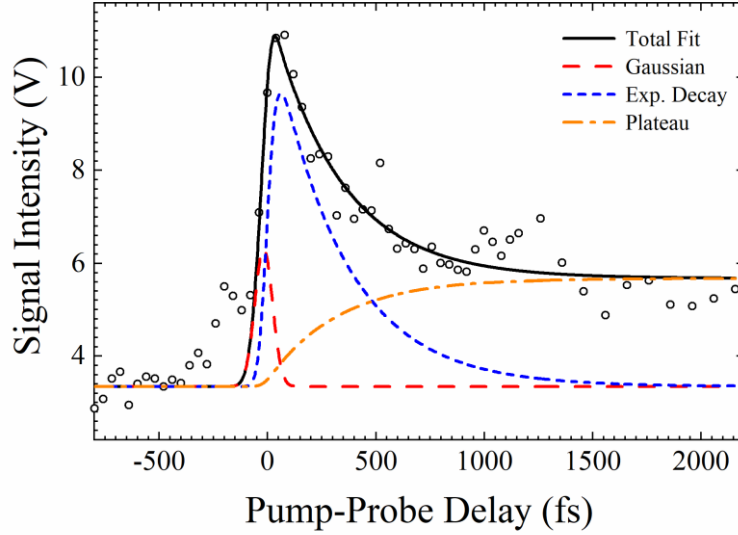
Figure 2.7: Typical pump-probe transient highlighting the total fit (solid black) of the change in signal intensity due to the probe delay with separate fitting functions encountered as a Gaussian (red long dash), exponential decay (blue short dash), and plateau function (orange dot dash).

Transient signals for each ion are analyzed by fitting a combination of a Gaussian, an exponential decay and plateau function to the data using a least squares method that has been described in detail elsewhere.[28–30] The Gaussian function (Eq. 2.7) is calculated using a as the intensity scalar, c as the center of the function, and σ as the standard deviation of the function which is used to find the full-width at half-maximum of the curve.

$$f(x) = ae\left\{-\left(\frac{x-c}{2\sigma^2}\right)^2\right\} \tag{2.7}$$

An exponential decay function (Eq. 2.8) is convoluted with the Gaussian instrumental response function and accounts for the relaxation in transient signals associated with an intermediate metastable state of a neutral species that decays with the measured lifetime (τ). Here, σ is the laser pulse width, τ is the time constant, t is the probe delay, and c is the adjustable center for the fit.

$$I(t, \tau) = a \left[1 - erf \left\{ \frac{\sigma}{2\tau} - \frac{t - c}{\sigma} \right\} \right] exp \left\{ \left(\frac{\sigma}{2\tau} \right)^2 - \frac{t - c}{\tau} \right\} \tag{2.8}$$

A plateau function (Eq. 2.9) is included to account for excited states with lifetimes longer than timescales addressed in the conducted experiments.

$$I_p(t) = a \left[1 - erf \left\{ -\frac{t - c}{\sigma} \right\} \right] \tag{2.9}$$

All transient signals in this thesis used a combination of these fitting functions to account for the electron dynamics which may evolve on timescales on the order of the laser pulse or over several hundred of ps. The usage of each fitting function depended heavily on the cluster system and is described in more detail within each chapter.

CHAPTER 3

ULTRAFAST PUMP–PROBE SPECTROSCOPY OF

NEUTRAL Fe_nO_m CLUSTERS (n, m < 16)

3.1 Introduction

Iron oxide clusters have been the subject of many gas-phase studies due to their ease of production and ability to provide a molecular level understanding of bulk-phase catalytic mechanisms. Ionic iron oxide clusters have been used for the oxidation of CO,[31–33] methane,[34] methanol,[35,36] and various hydrocarbons.[34,37] Neutral clusters have also shown activity for CO oxidation,[38] methanol dehydrogentation,[39] and oxidation of isoprene.[40]

The ionic cluster distribution of iron oxides have been explored under a variety of laser ablation conditions,[41–44] and neutral cluster distributions have been recorded using multiphoton ionization (MPI) and single photon ionization (SPI) with nanosecond duration laser pulses.[45,46] Unlike bulk iron oxides, which are known in three stoichiometries (FeO, Fe_2O_3, Fe_3O_4), the gas phase clusters show a strong preference for the stoichiometric combination $(FeO)_n$ below n = 10. Additionally, the geometric and electronic structures of iron oxide clusters, determined by several quantum approaches, differ substantially from bulk structures.[47–50] There is direct Fe-Fe bonding in the clusters that is not observed in bulk FeO. Small stoichiometric clusters ($(FeO)_n$, n < 4) form highly stable monocyclic 2D ring structures, where each oxygen atom bridges two iron

atoms. Computational studies suggest that larger clusters form through the assembly of these rings which stack to form layered structures, adopting a more compact spherical shape.[47] However, multiple isomers have been observed with ion mobility mass spectrometry and attributed to both 2D and 3D structures.[51] The vibrational spectra of many cationic iron oxide clusters have been explored with IR absorption and IR-induced dissociation spectroscopy to confirm structures.[52–54] Structurally, no significant changes are calculated between the neutral and charged clusters.[48]

The low-lying electronic states of FeO have been explored both theoretically[55–57] and experimentally.[58–60] Anion photoelectron spectroscopy has explored the evolution of the electronic states of iron monoxide (Fe_nO) clusters up to $n = 6$,[61] as well as other stoichiometric compositions up to Fe_4O_6.[62,63] However, variations with respect to electronic structures, spin multiplicities, and the richness of accessible structural isomers has posed considerable theoretical challenges for understanding iron oxide clusters.

Quantitative information about bond energies has been obtained by studying the dissociation patterns of small iron oxide cluster cations using collision-induced dissociation (CID),[64–67] thermal desorption,[68] and photodissociation experiments.[69] These experiments have shown that the bridging oxygen atom in Fe-O-Fe is strongly bound, and that O rich clusters contain O_2 units with low binding energy. For example, the dissociation energies for O rich clusters, containing up to six iron atoms have been measured showing O_2 units are weakly bound (< 0.8 eV).[68] The per atom binding energy of stoichiometric iron oxide clusters is high (~4.5 eV), independent of cluster size from n = 2 to 16,[47,70] and increases to > 5 eV for the cations.[48] These strong bonds require multiphoton absorption with 3.5 eV photons for significant photodissociation.[69] O rich

cation clusters have low thresholds for O_2 dissociation (< 0.7 eV[67]) for the Fe_2 series, except for $Fe_2O_3^+$ which has a threshold energy of 1.14 eV.[68] $Fe_2O_2^+$ and Fe_2O^+ have dissociation energies exceeding 4 eV and 5 eV,[67] respectively. The binding energy of FeO units are also high (~4 eV) for neutral $(FeO)_n$ clusters.[70] Due to the large binding energy, fragmentation is considered to be a local process, where clusters typically lose a single FeO or O_2 unit to produce a stoichiometric cluster upon excitation.

Time-resolved photoexcitation experiments of neutral iron oxides are used to explore the relationship between the relaxation dynamics of iron oxide clusters and their size and composition. Patterns in the relaxation dynamics of clusters from the pump probe transients are presented using 400 (3.1 eV) and 800 nm (1.55 ev) photons which is adequate for probing excited states without inducing dissociation. The ratio of amplitude coefficients between the fast fs response and the longer picosecond response is utilized as a method to interpret the changes in the relaxation dynamics of iron oxide clusters due to size and stoichiometry. With the data presented herein, details are provided regarding the electronic relaxation timescales and stability of iron oxide clusters following photoexcitation.

3.2 Results and Discussion

The IP of FeO is 8.56 eV,[71] requiring the absorption of one 400 nm and four 800 nm photons for ionization. After ionization, the cation contains up to 0.74 eV of energy above the ground state, and is stable by remaining below the dissociation limit of FeO^+ (3.52 ± 0.02 eV).[71] This photon dependence in my experiments is supported by a power study (Figure 3.1). The ionization of any given molecule by MPI can be shown by Equation 3.1:

$$W = \sigma_N I^N \qquad (3.1)$$

With σ_N representing the laser pulse cross section and N number of photons required for ionization. This equation can be linearized (Eq. 3.2) by taking the log of each side, creating:

$$\log_{10}(W) = N \log_{10}(I) + \log_{10}(\sigma_N) \qquad (3.2)$$

Through lowest order perturbation theory, the slope gives an approximation of the number of photons involved in ionization.[72] As only whole photons will be involved in ionization below the saturation limit, values of $N > 0$ are assumed to be 1. The slopes are rounded to the nearest integer values, which is assumed due to changes in the pump-probe response over traditional MPI. For $(FeO)_{1-3}$, the number of 400 nm photons was determined to be 1, and the number of 800 nm photons required for ionization was determined to be 3-4 (Figure 3.1), in agreement with their ionization potentials below.
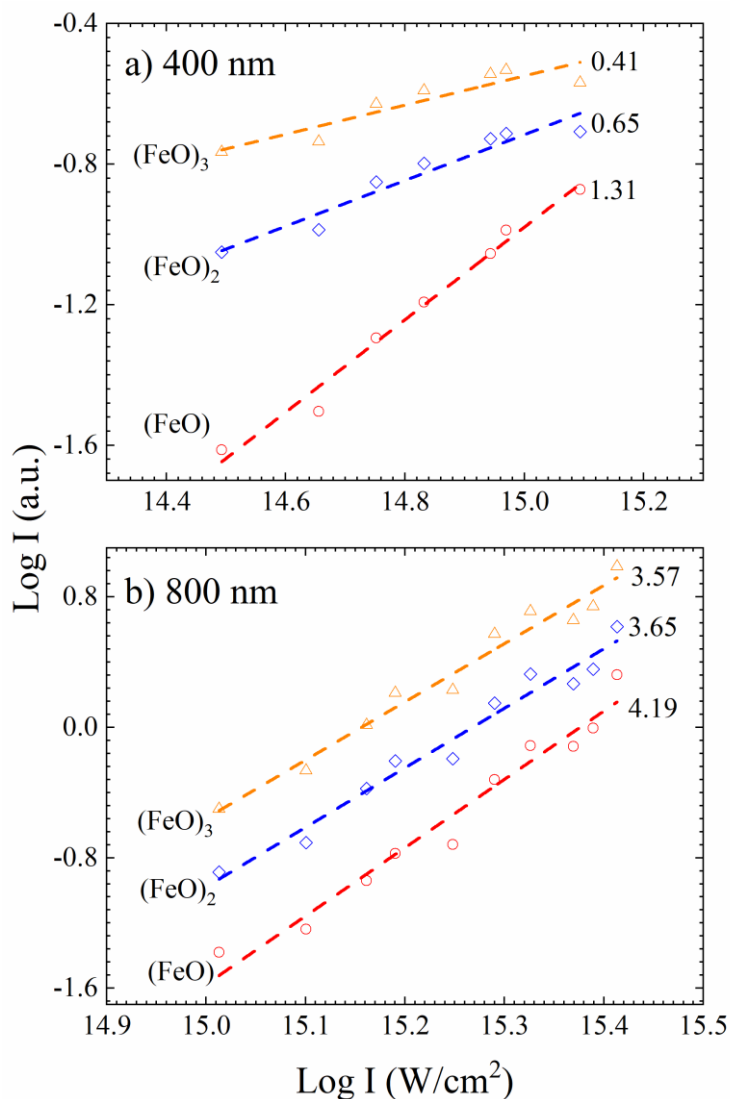
Figure 3.1: Power study of select $(FeO)_n$ clusters ($n < 4$) showing the number of photons involved in ionization from a) the 400 nm and b) 800 nm pulses.

The combined photon energies of the pump and four probe laser beams (9.3 eV) exceeds the IP for all clusters, with the IPs of $(FeO)_{2-5}$ calculated to be 7.46, 7.59, 7.39, and 7.60 eV, respectively.[47] Therefore, the absorption of one pump and three pump photons (total 7.75 eV) is sufficient for ionization. Alternatively, four probe photons by each of the $(FeO)_{2-5}$ clusters leaves an excess of 1.84, 1.71, 1.91, and 1.70 eV above the cation ground states, respectively. For the long-lived states of these clusters to be ionized

28

with four probe photons, the wavepacket must remain at least 1.16, 1.29, 1.09, and 1.3 eV above the ground states of $(FeO)_{2-5}$. Although the IPs of larger cluster have not yet been reported, they are predicted to decrease slightly with size.[45]

3.2.1 Neutral Cluster Distribution

The iron oxide cluster distribution recorded in the mass spectrometer depends on several experimental parameters such as ablation laser power, relative timing of the nozzle expansion, O concentration, and backing gas pressure. The cation distribution produced via the fs laser ionization of neutral clusters (Figure 3.2) is generally consistent with previous photoionization mass spectra of neutral Fe_nO_m beams,[45,46] and cations generated directly from laser vaporization sources.[69] However, single photon ionization with vacuum ultraviolet (VUV) lasers may be free of fragmentation, allowing weakly bound O rich clusters to be observed from the ionization of neutral clusters.[38–40,45] In these experiments, O rich clusters are observed in the distribution with small intensity. I suspect that most O rich clusters above Fe_nO_{n+2} are either not present in the initial neutral distribution or dissociate during or after the ionization process due to low binding energies.
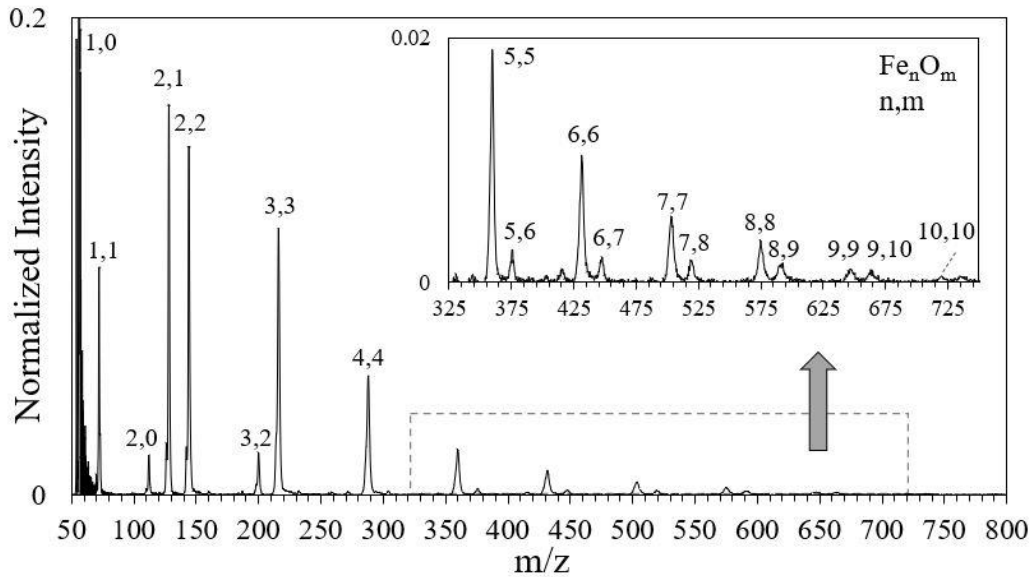
Figure 3.2: Mass spectrum of neutral Fe_nO_m clusters produced from ionization of both the 400 nm pump and 800 nm probe pulse at temporal overlap.

Above n = 3, the relative intensities of the $(FeO)_n$ clusters decay exponentially with the addition of each FeO unit. This is consistent with a typical thermodynamic cluster distribution and suggests that the ions accurately represent the neutral distribution. The Fe_nO_{n+1} cluster series has significant intensity above n = 5 and exceeds the signal intensity of the stoichiometric species above n = 10, where the binding energy of an additional O atom becomes comparable to that of an FeO unit. The largest cluster observed is $Fe_{15}O_{16}$.

3.2.2 Size Effects on Cluster Lifetime

The transient dynamics of the stoichiometric $(FeO)_n$ cluster series are presented in Figure 3.3. The increase in the temporal profile of the clusters indicates that a state, or band of states, with an appreciable lifetime is being accessed by the pump laser. Two

distinct relaxation pathways are observed in the transient signals and will be described separately.

The fs lifetime of the $(FeO)_n$ transients is plotted against their cluster size (Figure 3.3) and shows that the excited state lifetimes of the clusters decreases as they grow in size. The fs relaxation timescale is likely too short to be attributable to a fragmentation event and instead is related to the timescale of intramolecular vibrational redistribution (IVR) that assists in returning the excited electron back to the ground state. The decreasing lifetime of the clusters as more FeO units are incorporated shows that the fs relaxation component is assisted by the larger cluster's additional vibrational degrees of freedom. The excited state lifetime decreases steadily from $n = 1$, which has a lifetime of 352 ± 33 fs, before reaching a consistent value for clusters larger than $n = 5$. Above $n = 5$, the relaxation dynamics ($\tau = 103\text{-}143$ fs) are a factor of ~2.5x faster than in FeO. This saturation in lifetime coincides with the cluster size known to be the onset of 3D cluster geometries. The fitting coefficients and lifetimes of the $(FeO)_n$ ($n < 13$) series are summarized in Table 3.1.
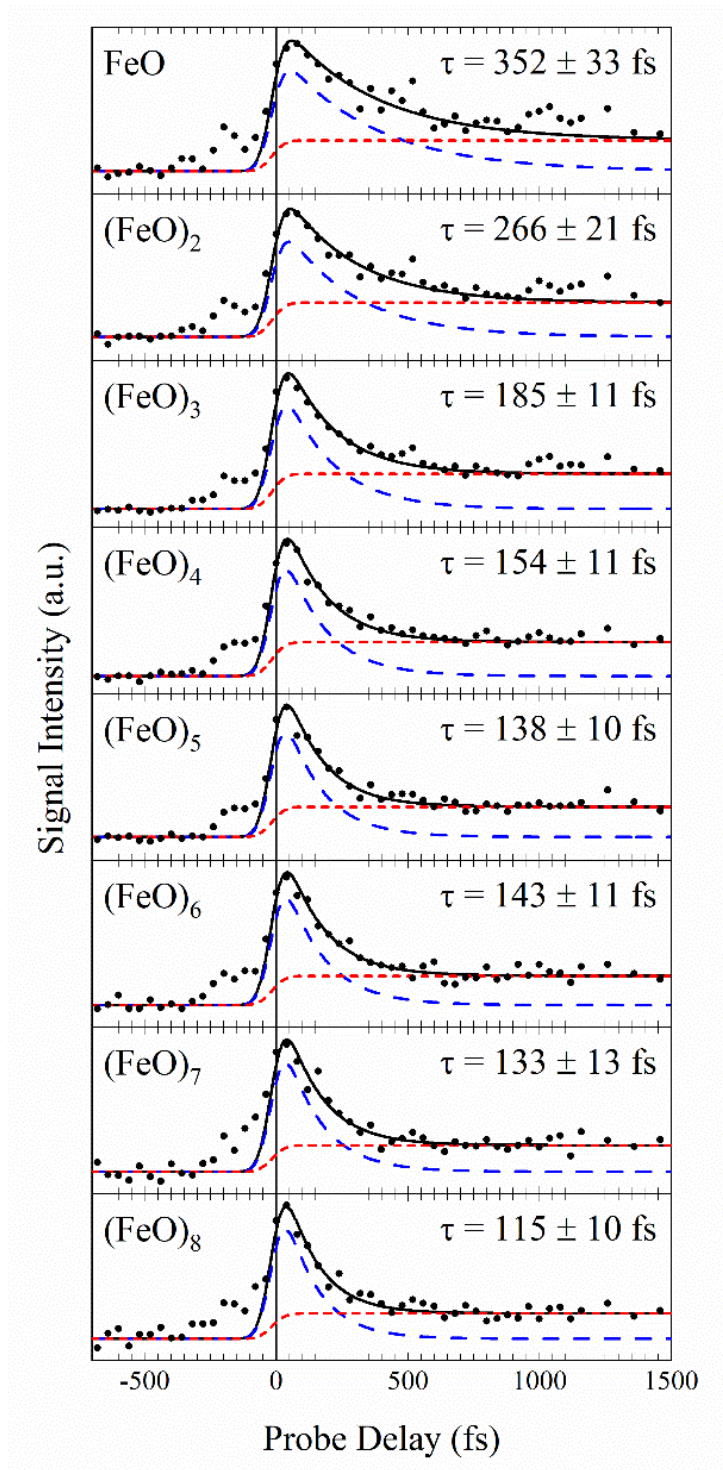
Figure 3.3: Pump-probe transients of the $(FeO)_n$ clusters (n < 9) with separate fitting functions shown as the exponential decay (blue long dash) and long-lived state (red short dash). Lifetimes are shown in each frame.

Stoichiometric clusters have a similar transient signal, suggesting a common chromophore is being accessed. The electronic structure of FeO is well understood and serves as a starting point to describe the nature of the larger cluster's excited states prepared by the absorption of a 400 nm photon. The manifold of excited states for FeO is dense,[56] having 49 states within an energy range of 3.1 eV.[56] Several low-lying bands have been well characterized below the dissociation limit of 4.20 ± 0.13 eV.[73] The ground state molecular orbital configuration of FeO is $8\sigma^2 3\pi^4 4\pi^2 1\delta^3 9\sigma^1$, where the O-derived orbitals lie below the Fe 3d-derived orbitals, formally resulting in a charge transfer of two electrons from the Fe to O atom. The lower lying electronic A and B/C states recorded in photoelectron spectroscopy are attributed to excitation from the Fe 3d-orbitals (1δ or 9σ).[63] The D state resides at 1.89 eV and is attributed to excitation of the 4π electron, which is also from the Fe 3d-orbital.[63] The excited state accessed here, with 3.1 eV, arises from excitation of either the 3π or 8σ orbitals which have predominantly oxygen character. Thus, the excited electron moves from the low-lying orbitals that are predominantly O to a nonbonding Fe orbital.

Photoelectron spectroscopy performed on iron monoxides has shown only small changes in energy levels with increasing iron atoms.[61] The strong similarities with the photoelectron spectra of FeO[59,63] enables us to apply the spectra of the larger clusters to approximate the electronic structure of FeO. The larger $(FeO)_n$ clusters all present higher energy states following a ~1 eV gap above the Fe orbitals, where several less characterized states appear. A broad band is observed at ~3 eV above the ground state that is assigned as the G band in Fe_2O.[61] Thus, I tentatively assign the excitation of the stoichiometric clusters as G band excitations.

A similar argument can be applied to larger stoichiometric clusters, although their electronic structures are less known. The excited states of the clusters become more congested, and the density of states increases with size. Even clusters as small as Fe_3O_3 and Fe_4O_4 exhibit no sharp peaks in photoelectron studies, suggesting a high density of states.[62] Although assignments of the excited states are difficult, they also arise through transfer of an electron from the O atom to the Fe atom.

Table 3.1: Fitting coefficients for the stoichiometric iron oxide clusters showing lifetime (τ), fitting coefficient for the decay (C_E), plateau (C_P) and ratio of the functions as C_P/C_E (γ).

Species	C_E	τ (fs)	C_P	γ
FeO	1.010	352 ± 33	0.239	0.237
Fe_2O_2	1.042	266 ± 21	0.273	0.262
Fe_3O_3	1.175	185 ± 11	0.267	0.228
Fe_4O_4	1.251	154 ± 11	0.252	0.201
Fe_5O_5	1.309	138 ± 10	0.232	0.177
Fe_6O_6	1.341	143 ± 11	0.218	0.163
Fe_7O_7	1.502	133 ± 13	0.204	0.136
Fe_8O_8	1.563	115 ± 10	0.187	0.119
Fe_9O_9	1.390	150 ± 19	0.159	0.114
$Fe_{10}O_{10}$	1.447	135 ± 21	0.139	0.096
$Fe_{11}O_{11}$	1.601	80 ± 14	0.154	0.096
$Fe_{12}O_{12}$	1.622	103 ± 18	0.149	0.092

The ratio between the fitting coefficients, γ (C_P/C_E), decreases linearly with cluster sizes above n = 2 for the stoichiometric clusters. For FeO, ~25% of the population remains in the excited state for > 20 ps. The excitation photon energy remains below the dissociation energy, and therefore the long decay is a consequence of populating a bound

state. Four probe photons can ionize an excited neutral state that is at least 2.26 eV above the ground state. Therefore, neither the A state nor the B/C states, which are ~0.5 eV and ~1 eV above the ground state, accounts for the long-lived signal. This suggests that the excited electron does not transfer back to the O atom within the 20 ps timescale. The γ for FeO is 0.237, increases to 0.262 for n =2, and then decreases almost linearly with the addition of each FeO unit. The increased density of states for larger clusters enables a larger proportion of the wavepacket to undergo electronic relaxation to low energy states that are inaccessible for ionization by the probe pulse.

3.2.3 Oxidation Effects on Cluster Lifetime

The Fe_2O_n cluster series is the most studied series of iron oxide clusters, and the nature of the excited state of Fe_2O can be assigned using data provided by photoelectron spectra discussed above. Fe_2O has an IP of 6.78 ± 0.05 eV and remains just below the $(FeO^+ + Fe)$ dissociation energy of 2.60 eV upon excitation with the 1 + 4 pulse sequence.[61]

Changes in the ultrafast relaxation dynamics due to oxidation state are observed by comparing the dynamics of clusters containing the same number of metal atoms but varying number of O atoms. Assuming that each O atom has an oxidation state of -2, then the oxidation state of the Fe atoms can be evaluated in each cluster such that in neutral $(FeO)_n$ all the Fe atoms have a +2 oxidation state. For Fe_2O, where the Fe atoms share the O atom equally, the oxidation state of each of the Fe atoms is +1

The excited state lifetime decreases with additional oxygen atoms, and therefore shows that the higher oxidation state of iron leads to faster electron relaxation back to the oxygen. The fs lifetimes of Fe_2O_2, Fe_2O, and Fe_2 are shown in Figure 3.4 to be 268 ± 22

fs, 404 ± 37 fs, and 699 ± 163 fs, respectively. Further, the γ values for the Fe_2O_n series decreases from 0.464 to 0.262 with additional O. Therefore, with the increase in oxidation state of the Fe, less of the population remains in the bound excited electronic state. The fitting coefficients for Fe_2O_n and the other non-stoichiometric clusters ($n < 7$) are summarized in Table 3.2.

The maximum signal intensity for the Fe_2O_n cluster series shifts in time delay with the number of O bound within the cluster (Figure 3.4). Fe_2 reaches its maximum signals at later time delays than the other clusters. However, the transient signal for Fe_2 requires a growth function, with a lifetime $\tau_g = 40 \pm 15$ fs, to accurately account for the dynamics. This growth is sufficiently fast to be attributed to direct dissociation of a larger neutral cluster's excited state. Fe_2^+ has a low IP (6.3 eV) and can be ionized directly by four probe photons. The delay in ion signal suggests that Fe_2 is not present in the neutral cluster beam, and instead highlights the dissociation dynamics of a larger neutral cluster after being exposed to the pump beam. Although I cannot identify the parent cluster from these experiments, one possibility is the facile dissociation of energetic isomers. For example, formation of Fe_2 occurs at ~0.5 eV from Fe_2O_2, attributed to a high energy isomer of Fe_2O_2.[65]
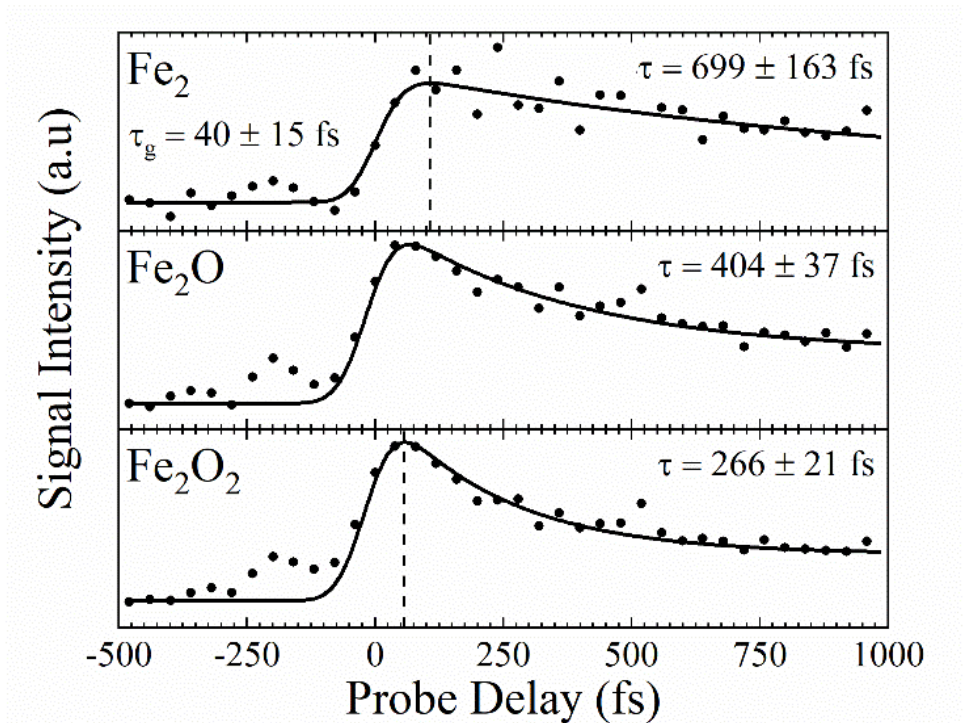
Figure 3.4: Transients of Fe_2O_n (n = 0-2) clusters with vertical lines drawn to emphasize the shift in peak maxima. Decay (τ) and growth (τ_g) lifetimes are shown in each frame.

Several ion transients are recorded in the Fe_3O_n (n = 1-4) series (Figure 3.5). Fe_3O_3 and Fe_3O_2 appear with strong signals, while Fe_3O and Fe_3O_4 are weak signals. Fe_3O_n (n > 4) clusters have a O_2 dissociative energy of < 0.6 eV[68] and are not expected to survive the ionization mechanism. Similar to the pattern described in the Fe_2O_n clusters, the lifetime of Fe_3O_n clusters also decrease with additional O content. The lifetime of Fe_3O_3 (185 ± 11 fs) is shorter than Fe_3O_2 (323 ± 43), and Fe_3O_4 exhibits the shortest lifetime of the series (85 ± 20 fs). Fe_3O is only observed under very low O concentrations, but also fits into this pattern with a long lifetime of 526 ± 104 fs.
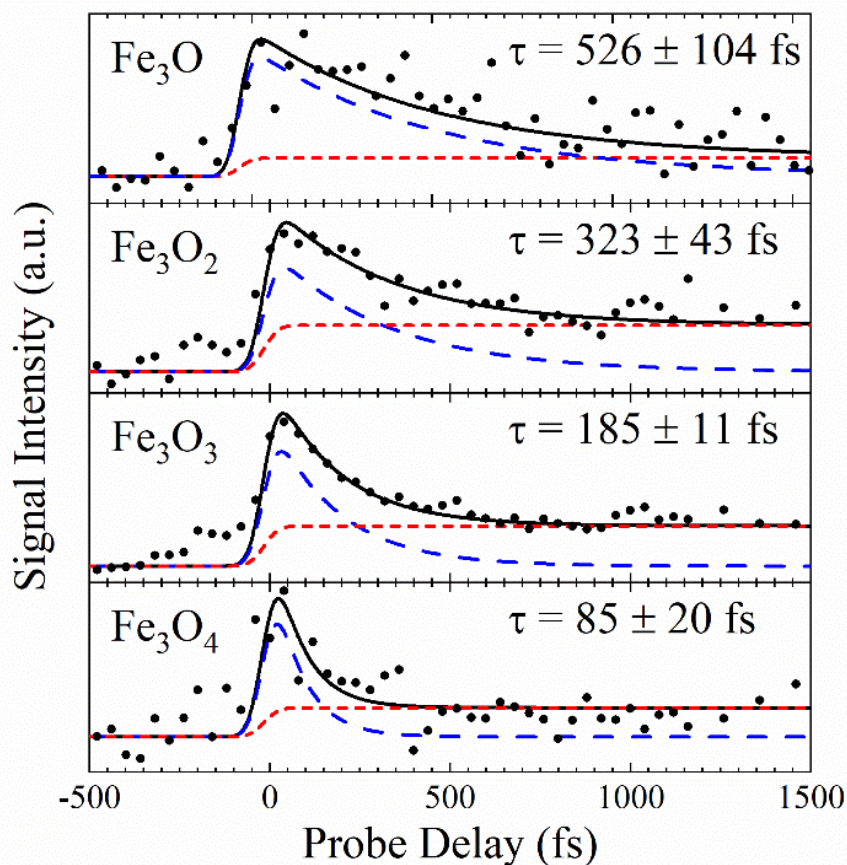
Figure 3.5: Pump-probe transients of the Fe_3O_n (n = 1-4) clusters with separate fitting function shown as the exponential decay (blue long dash) and long-lived state (red short dash). Decay lifetimes are shown in each frame.

With a higher Fe content, the O atoms are no longer shared equally among the Fe atoms as they were for the Fe_2O_n series. For Fe_3O_2, one of the Fe atoms is attached to two O atoms for a +2 oxidation state, and two of the Fe atoms only bind to one O to have +1 oxidation states. For Fe_3O, two of the Fe atoms are in a +1 oxidation state and one Fe has an oxidation state of 0. Fe_3O_4 has a structure similar to the Fe_3O_3, but contains an extra O bound to one of the terminal Fe atoms, making it a +4 oxidation state. Similar to the Fe_2O_n series, removing one O extends the lifetime of the state by ~150 fs, and removal of the second oxygen atom extends the lifetime by ~350 fs. This supports the argument that the lower oxidation state of the Fe atom extends the fs lifetime of the cluster transient.

38

With the decrease in oxidation state, the γ values for the Fe_3O_m series also decreases, with the exception of Fe_3O which is recorded with a $\gamma = 0.0$. Fe_3O_2 has a $\gamma = 0.305$ and drops steadily with the addition of each oxygen until reaching 0.110 for Fe_3O_4. This decrease in γ with O is consistent with Fe_2O_n clusters.

The lifetimes and patterns measured in the dynamics for the cluster series of Fe_4O_n, Fe_5O_n, and Fe_6O_n are similar to those determined in smaller clusters. These mid-range clusters represent the transition in geometry from 2D rings to 3D structures. Some calculations have predicted that Fe_5O_5 is planar,[47] while others have shown the 3D geometry is lower in energy.[48] 3D structures support a larger number of stable stoichiometries and enables stronger bonding arrangements with an extra oxygen atom. In Fe_nO_{n+1}, more Fe d-electrons transfer to the additional O atom. The extra O is likely bridged between two Fe atoms and therefore increases the oxidation state of two Fe atoms to +3 while the rest remain at +2. This change in oxidation state will be most profound in smaller clusters, where a single O makes the biggest adjustment to the overall cluster stoichiometry.

The Fe_4O_n cluster series contains only one dominant cluster, Fe_4O_4. The Fe_5O_n (n = 5-6) cluster series shows the presence of two clusters and is consistent with all other series, showing a Fe_5O_6 lifetime (116 ± 21 fs) slightly shorter than the Fe_5O_5 transient (142 ± 10 fs). Also, the γ of Fe_5O_5 decreases from 0.177 to 0.091 with the additional O atom. The ultrafast dynamics of the Fe_6O_n (n = 5-7) cluster series are consistent with the smaller clusters. However, the effect of the missing O on the relaxation dynamics is not as pronounced as in smaller clusters, and only extends the lifetime by ~6% for Fe_6. The lifetime of Fe_6O_6 is 158 ± 32 fs and decreases by ~54% with additional oxygen atoms.

39

Interestingly, Fe_6O_7 has the shortest lifetime of all clusters detected in this study with a lifetime of only 68 ± 10 fs. Further, γ decreases for Fe_6O_5 to Fe_6O_7 from 0.130 to 0.049 with additional O, but Fe_6O_6 breaks the trend having a value of 0.163.

Table 3.2 Fitting coefficients for suboxide Fe_nO_m clusters ($n < 7$).

Species	C_E	τ (fs)	C_P	γ
Fe_2	0.586	699 ± 163	0.272	0.464
Fe_2O	0.883	404 ± 37	0.299	0.339
Fe_3O	1.000	526 ± 104	0.000	0.000
Fe_3O_2	0.988	323 ± 43	0.301	0.305
Fe_3O_4	1.708	85 ± 20	0.187	0.110
Fe_5O_6	1.696	116 ± 21	0.154	0.091
Fe_6O_5	1.235	158 ± 32	0.160	0.130
Fe_6O_7	2.029	68 ± 10	0.099	0.049

For the Fe_7O_n series, the addition of a single O reduces the lifetime of the excited state by ~38% from 133 ± 13 fs to 96 ± 18 fs (Table 3.3). This difference in lifetime between the two series is consistent with the trend obtained in the smaller clusters. For neutral Fe_nO_{n+1} clusters, an excess O has a binding energy exceeding 5 eV and is often equal to the binding energy of FeO units at these large cluster sizes.[47,74] Therefore, the transient dynamics are recorded for the $(FeO)_n$ and Fe_nO_{n+1} series up to n = 12 and 15, respectively. For larger Fe_nO_{n+1} clusters, the fs lifetimes are comparable to the similar sized $(FeO)_n$ clusters. Small fluctuations are recorded in the fs lifetime of both series with changes in size but remain consistent within the error bars to be an average of ~115 fs. This suggests that the influence of the additional O and increase in oxidation state is small for these larger clusters. According to IVR, the fast component of the Fe_nO_{n+1} clusters should decrease with size because of the larger degrees of freedom to dissipate

the energy. However, as described earlier, these clusters have already exceeded the size

where a saturation in the relaxation dynamics was achieved.

Table 3.3: Fitting coefficients for the ultrafast transient dynamics of selected large Fe_nO_{n+1} clusters.

Species	C_E	τ (fs)	C_P	γ
Fe_7O_8	1.588	96 ± 18	0.116	0.073
Fe_8O_9	1.454	139 ± 22	0.081	0.055
Fe_9O_{10}	1.908	98 ± 14	0.126	0.066
$Fe_{10}O_{11}$	1.694	107 ± 15	0.066	0.039
$Fe_{11}O_{12}$	1.712	128 ± 18	0.092	0.054
$Fe_{12}O_{13}$	1.564	120 ± 15	0.061	0.039
$Fe_{13}O_{14}$	1.691	123 ± 17	0.070	0.041
$Fe_{14}O_{15}$	2.022	103 ± 18	0.048	0.024
$Fe_{15}O_{16}$	1.858	110 ± 20	0.021	0.011

The long-lived excited states remain accessible in larger clusters for both cluster

series (Table 3.3). For n = 8, the bound state accounts for ~10% of the total population

and decreases linearly with the addition of each FeO unit. This is consistent with the fact

that larger clusters contain a larger density of states than smaller clusters, thereby

enabling the electronic energy conversion into vibrational motion while returning to the

ground electronic state.

3.3 Conclusion

With fs ionization, stoichiometric $(FeO)_n$ clusters dominate the cluster distribution

for n < 10 and Fe_nO_{n+1} clusters dominate at n > 10. Weakly bound O rich clusters are not

observed with fs laser pulses, suggesting that the clusters detected in my mass spectra are

stable to within the energy of 1 probe photon. Although fragmentation is possible, it was

not observed with the exception of Fe_2.

Upon irradiation of a 400 nm fs pulse, an electron migrates from the O atom to

the non-bonding orbitals of the Fe atom within the cluster. This results in a large

proportion of the wavepacket relaxing on the fs timescale to a low-lying electronic state, assisted by IVR. A smaller fraction of the wavepacket remains in a bound long-lived (> 20 ps) state where the excited electron remains in the nonbonding Fe orbitals.

Transient signals of the neutral iron oxide clusters are compared as a function of growing cluster size and stoichiometric composition. The lifetime of the excited states of the clusters decreases rapidly from ~350 fs to ~140 fs until the clusters adopt a 3D stoichiometry, then remain roughly independent of cluster size. Changes in the oxidation state of the Fe atoms has a large effect on the lifetime of small clusters, where higher oxidation states have shorter lifetimes. The shortest lifetimes are obtained for mid-range clusters with an extra O (Fe_6O_7 and Fe_7O_8), which are among the smallest clusters recorded that contain excess O. As the cluster size grows, a smaller proportion of the wavepacket remains in the long-lived bound excited state.

CHAPTER 4

EFFECT OF OXIDATION ON ULTRAFAST CHARGE RECOMBINATION IN

NEUTRAL (NiO)$_n$ CLUSTERS (n < 6)

4.1 Introduction

NiO is a strongly correlated antiferromagnetic material with a high Néel

temperature of 523 K,[75–77] making it a strong candidate for spintronics and solar energy

applications as an efficiency-enhancing interfacial layer. Photoexcitation of NiO showed

that a ferromagnetic response of low-spin states in NiO may be achieved,[76–79] allowing

insulator-like properties to be altered.[80] Ultimately, the timescale that NiO materials

redistribute excitations and the dynamics of charge-carrier recombination dictate their

overall reactivity in photocatalytic solar cell applications and efficiency as magnetic

devices. NiO charge-carrier recombination in solar cell interfaces,[81] sensitized with

dyes,[82] nanoparticles,[83] and charge transfer from NiO to another substrate[84] may occur

over fs to ns. NiO redistributes photoexcitation via superexchange interactions and

coherent oscillations (phonons).[75,78] Although NiO has revealed phonon-related

relaxation, coherent lattice vibrations and uniform electronic properties typically ignore

the possibility of numerous dislocation sites, atomic vacancies, and grain boundaries that

result in complex charge carrier dynamics.

A local rearrangement of the 3d-electrons plays a crucial role in many properties

of correlated transition metal oxide materials and supplies important information on

magnetic interactions. Ni has the lowest excitation energy of the first-row transition metal

elements and an open 3d subshell nature, providing an extremely rich density of states

and typically short lifetimes. Excited state lifetimes in bulk NiO as short as 10 fs have

been identified as Hund excitations,[78] with sub-ps formation of polarons that localize at specific defect sites prior to recombination.[85] The d^8 ground state electron configuration of NiO formally consists of fully occupied t_{2g} and half-filled e_g orbitals, with strong hybridization between the 2p and 3d bands.[78] In strongly correlated transition metal oxides, such as NiO, the Mott insulator concept suggests that electron repulsion splits the d bands into an occupied and unoccupied Hubbard band.[80,86] NiO is an intermediate charge-transfer insulator, suggesting that charge transfer is smaller than the Hubbard U,[78] leaving O-2p bands located in the range of the occupied Hubbard band. However, the d-shell of Ni is the most compact of all transition metals, making d-bonding effects the least important of all metal oxide systems.[87]

The s character of the conduction band minimum was neglected in many studies, but recently found to be important in more detailed calculations.[86,88] Although NiO is considered an insulator with a commonly reported band gap of 4.1-4.3 eV,[79,80] the onset of absorption has been recorded as low as 3.1 eV.[89] This low-energy feature has been attributed to excitation between the valence Ni-3d and Ni-4s character of the conduction band minimum, allowed due to 3d bands containing significant O-2p character.[89] This challenges conventional knowledge that localized 3d (e_g) states dominate the conduction band edge.

Nickel oxide clusters are among the least studied transition metal oxide species and represent a challenge to theoretical computations because of the high number of energetically competitive structural isomers and spin configurations. Molecular-scale clusters possess electronic properties that change with the addition or subtraction of single atoms, enabling insights to the investigation of defect sites in bulk-scale reactions.

Here, femtosecond pump-probe spectroscopy coupled with theoretical calculations are used to interrogate the effects and magnitude of Ni-s, p, and d orbital photoexcited transitions on molecular-scale neutral NiO cluster lifetimes. Results from this study show a unique reliance on the Ni orbital contributions to the photoexcited cluster lifetimes, allowing for a deeper understanding of the bulk-scale electronic properties.

4.2 Results and Discussion

All spectra were recorded using 7.92×10^{14} W/cm^2 400 nm pump and 1.62×10^{15} W/cm^2 800 nm probe pulses. Neutral nickel oxide clusters were produced using a seeded He gas pulse (1% O_2) and an average of 1000 spectra at the temporal overlap of the two laser pulses. The 800 nm beam was temporally delayed 600 fs prior (-) to the 400 nm pulse and moved in 40 fs increments towards (+) the 400 nm pump pulse, taking an average of 500 shots per scan as the probe is delayed to 2.5 ps. The change in each ion signal with respect to the probe delay is then discussed, providing excited state dynamics unique to each cluster species. The changes in excited state dynamics are analyzed as a function of increasing size and changes in oxidation of stoichiometric $(NiO)_n$ clusters. Theoretical calculations are used to relate experimental lifetimes to complex electronic properties in each cluster.

4.2.1 Neutral Cluster Distribution

At temporal overlap, an ionized neutral nickel oxide distribution was produced (Figure 4.1). The most prominent peaks are the Ni_nO_{n-1} series from values of n < 8 and then Ni_nO_{n-2} for n > 7, consistent with previous experiments.[90] The binding energy per atom of small nickel oxide clusters increases with size from ~3.1 to 3.7 eV, while the binding energy per monomer for $(NiO)_n$ fluctuates between 4.1 eV for $(NiO)_2$ and ~3 eV

45

for $(NiO)_5$.[50] Therefore, stoichiometric $(NiO)_n$ clusters of $n > 5$ are not expected to survive a single pump photon of 3.1 eV due to the ease of dissociation.
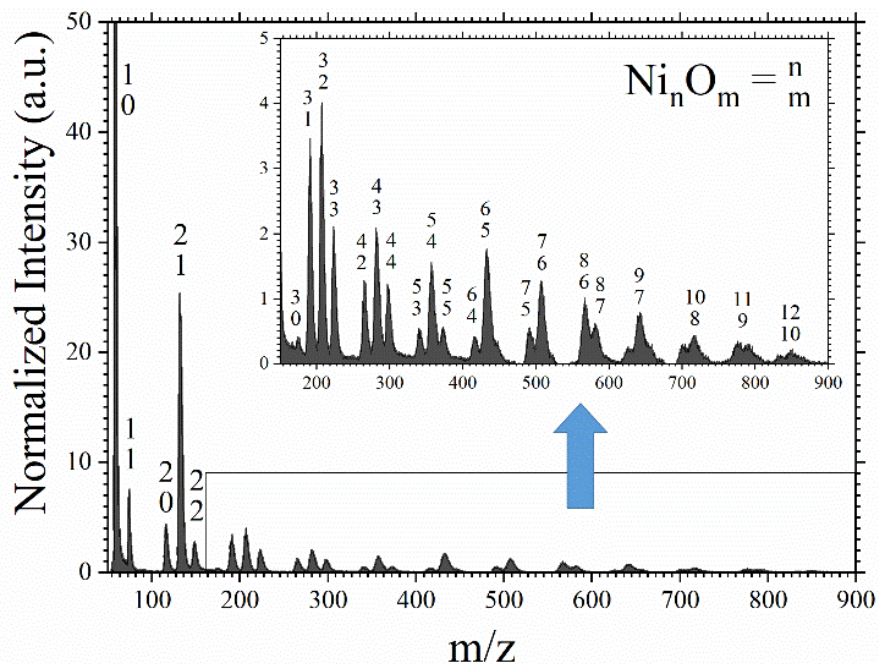
Figure 4.1: Neutral nickel oxide cluster distribution following ionization at temporal overlap from the pump and probe pulse.

Oxygen-rich nickel oxides easily lose O_2 upon excitation,[90] consistent with the lack of oxygen-rich clusters observed in my experiment. Bare Ni_2 and Ni_3 clusters appear in the neutral mass spectrum shortly after the arrival of the probe pulse, suggesting formation of these clusters from parent species or delayed ionization from a bound intermediate state. Structures of molecular nickel oxide clusters were previously calculated,[50,91] showing all NiO clusters have bridging O atoms, avoiding terminal O locations.

4.2.2 Size Effect of $(NiO)_n$ Clusters

The calculated potential energy curves of NiO reveal a rich density of excited states below the $X^3\Sigma^- \rightarrow {}^3\Sigma^-$ photoexcitation at 3.04 eV.[92] Photoelectron spectroscopy

(PES) of NiO shows several low-lying excited states below 3 eV.[93–96] My measurements show the $^3\Sigma^-$ state of NiO has a lifetime of 214 ± 12 fs, and may cross into a long-lived $^3\Sigma^+$ or $^3\Delta$ state which is represented by the plateau function. Conversely, the excited states of NiO have microsecond lifetimes under visible excitation.[97]
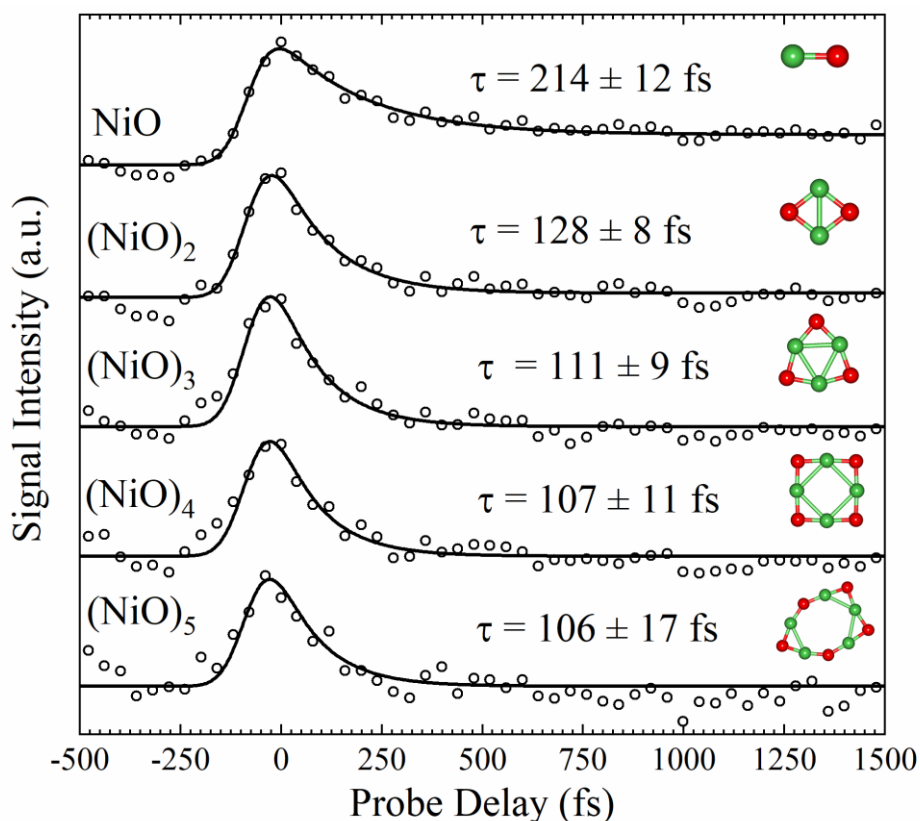
Figure 4.2: Pump probe transients of the $(NiO)_n$ (n < 6) cluster series with the lifetimes and cluster structures computed by Sayres shown above each cluster signal.

$(NiO)_{2-5}$ clusters all form similar 2D ring structures[50,91] that are reflected in the transients of the $(NiO)_n$ clusters (n = 1-5), showing a similar fast relaxation of ~110 fs following absorption of a 3.1 eV photon (Figure 4.2). Similar to bulk NiO, the fast relaxation is attributed to e-e scattering and rapid recombination. The slightly longer lifetime of NiO over the other stoichiometric clusters is due to a lower density of states and degrees of freedom. The ratio of the plateau (δ) and decay (κ) function amplitudes on

the total transient fit reveals a decrease in the long-lived component with size of stoichiometric cluster (Table 4.1). A long-lived (> 2.5 ps) state is accessible in NiO (δ = 0.18) and $(NiO)_2$ (δ = 0.02) but is not present in larger clusters. The decreasing plateau component of the transient signal suggests that the larger clusters contain sufficiently degrees of freedom to enable internal conversion for efficient charge recombination.

Table 4.1: The fitting parameters of neutral $(NiO)_n$ clusters (n = 1-5) with the decay lifetime (τ), percent decay (κ) and plateau (δ) fitting function amplitudes.

Cluster	τ	κ	δ
NiO	214 ± 12	0.82	0.18
$(NiO)_2$	128 ± 8	0.98	0.02
$(NiO)_3$	111 ± 9	1	0
$(NiO)_4$	107 ± 11	1	0
$(NiO)_5$	106 ± 17	1	0

4.2.3 Oxidation Effect on Cluster Lifetime

Stoichiometric $(NiO)_n$ clusters void of up to two O atoms are evaluated up to n = 5. Oxygen deficient clusters are shown to possess a longer lifetime, attributed to the change in cluster geometry with lower O atoms from the stoichiometric cluster which results in a broken symmetry of the cluster and more localized electrons and holes. All lifetimes and fitting parameters for the suboxide clusters are summarized in Table 4.2.

The Ni_2O_n (n = 0-2) series shows a change in the excited state transients with O content (Figure 4.3). The lowest energy configurations of the Ni_2O_n series are planar, with the spin states of Ni_2O and Ni_2O_2 both triplets. The IP for these clusters increases linearly with O content, increasing the DoS and facilitating a faster relaxation to the ground state.
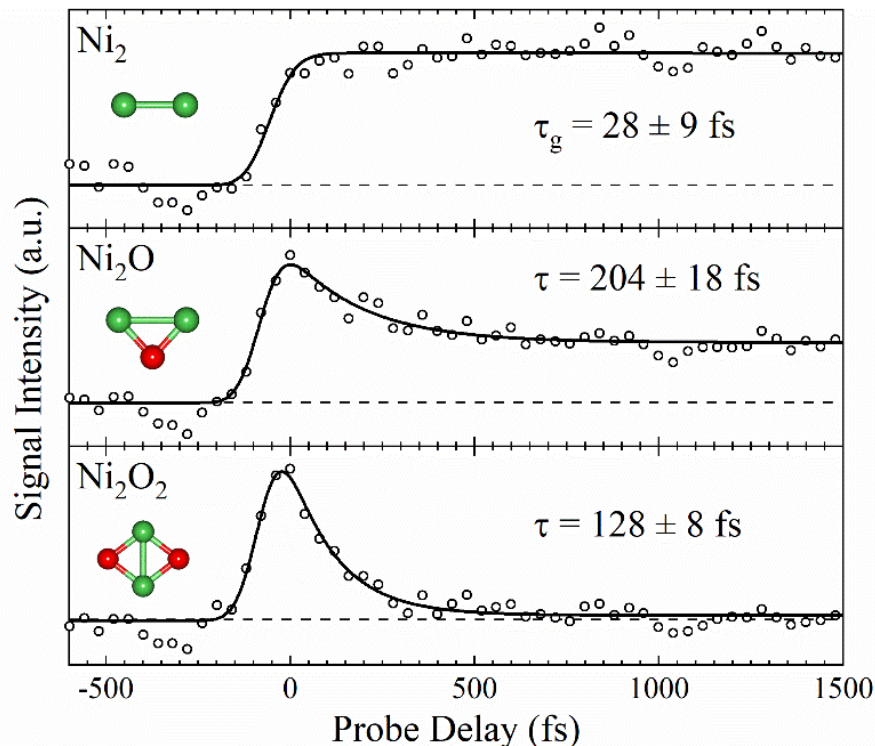
Figure 4.3: Pump-probe transient response of the Ni_2O_n (n < 3) series with lifetimes shown in each frame. Ni_2 is shown with the growth time (τ_g).

The transient signal for Ni_2 requires a growth function (τ_g) and shows the entire population reaches a long-lived (>2.5 ps) state, potentially arising from multiple channels. Ni_2 may be produced upon the release of O from Ni_2O after the interaction with the pump pulse, followed by subsequent ionization. However, Ni_2O is a common fragment and is suggested to be a particularly stable cation unit.[90] Additionally, the dissociation energy of Ni_2O is 4.38 eV[98] and Ni_2 has an IP of ~7.6 eV,[99] requiring a total of 12 eV to observe the Ni_2 cation. Dissociation from Ni_2O_2 to form Ni_2 is unlikely, requiring removal of two O atoms without the removal of a Ni atoms. The τ_g matches the cross correlation of the laser beams (28 ± 9 fs), suggesting an instantaneous ionization of neutral Ni_2 present in the neutral cluster population. Due to the low bond energy of ~2

49

eV,[98] Ni_2 is not expected to survive the excitation of a single 3.1 eV pump photon, but may reach a long-lived state above this dissociation energy.

The ground state of Ni_2 has been investigated with controversial results that arise from the interaction of two $3d^9 4s^1$ Ni atoms, forming a single bond between the 4s orbitals with little 3d involvement. The electronically excited states are less characterized and difficult to assign, but appear at wavelengths < 450 nm.[100] The UV-vis spectra of Ni_2 shows several absorption bands at ~3 eV.[101,102] The $d\sigma_g \rightarrow p\pi_u$ ($^3\pi_u$ or C state) is strongly bound,[101,103] but overlaps with the dissociative $s\sigma_g \rightarrow s\sigma_u$ ($^3\Sigma_u^-$ or B state).[103] A $d\delta_g \rightarrow p\pi_u$ transition ($^3\Phi_u$ state) may also exist nearby, but is suggested to have weak signal intensity. No decrease in the transient Ni_2^+ signal is recorded here, suggesting the C $^3\pi_u$ state of Ni_2 is accessed by the 3.1 eV pump photon and is long lived due to poor overlap with lower lying states.

Ni_2O contains a long-lived (>2.5 ps) excited state in addition to the slower (~172 fs) relaxation, suggesting multiple relaxation channels. With a single O, Ni_2O forms a cyclic ring rather than a bent linear structure. With the increase in O-2p character, the density of states becomes richer, facilitating relaxation to the ground state. However, with a δ = 0.42, almost 30% of the population still reaches a long-lived state which survives over 2.5 ps. Ni_2O_2 contains a single fast (~111 fs) decay from the increased symmetry (and higher stability) of the ring-like structure, and therefore more delocalized charge-carrier upon photoexcitation (e-e scattering). However, Ni_2O_2 does not possess any transient long-lived states, suggesting that the inclusion of additional O-2p electron character to the stoichiometric cluster is enough to cause a single fast decay of ~100 fs back to the ground state. The 4s orbitals have favorable exchange interactions with the Ni

3d electrons due to large spatial overlap and are therefore strongly coupled, enabling a rapid relaxation. Ni_2O_2 has a closed electronic shell from the two $3d^9 4s^1$ Ni configurations and four O-2p electrons, making photoexcitation akin to the bulk-scale e-e scattering process.

Table 4.2: Fitting parameters of suboxide neutral Ni_nO_x clusters with the relaxation lifetime (τ), percent decay (κ) and plateau (δ) fitting function amplitudes.

Cluster	τ (fs)	κ	δ
Ni_2	$28 \pm 9^*$	0	1
Ni_2O	204 ± 18	0.68	0.32
Ni_3	$170 \pm 51^*$	0	1
Ni_3O	191 ± 18	0.82	0.18
Ni_3O_2	202 ± 23	0.87	0.13
Ni_4O_2	187 ± 22	0.96	0.04
Ni_4O_3	176 ± 20	1	0
Ni_5O_3	117 ± 20	1	0
Ni_5O_4	151 ± 20	1	0
Ni_6O_4	225 ± 40	1	0
Ni_6O_5	173 ± 23	1	0
Ni_7O_5	167 ± 36	1	0
Ni_7O_6	142 ± 23	1	0

*Indicates growth lifetime instead of decay

In the Ni_3O_n (n = 0-3) series, the transient lifetime and long-lived (>2.5 ps) excited state component increases with decreased O character (Figure 4.4). The lowest energy configurations of the Ni_3O_n clusters are planar, containing a triangular Ni core similar for all clusters except Ni_3O, which has near degenerate pyramid structure that is not planar and spin quintet. The extra O atom creates slightly longer Ni-Ni bonds in Ni_3O_2 and is ferromagnetically coupled. However, the metal bonds recompress in Ni_3O_3. Typically, the O atoms contain a 1/3 spin ferromagnetically coupled to the Ni atoms. The

asymmetry of the cluster makes one Ni atom a higher spin (0.9). The stoichiometric cluster has the strongest binding energy per atom and also the shortest lifetime of the series (109 ± 8 fs). Similar to Ni_2, the bare Ni_3 cluster has considerable intensity after the arrival of the probe pulse, but is not likely to survive the ionization process with a binding energy of 3 eV or lower.[104,105] Unlike Ni_2, however, the growth lifetime of Ni_3 (~192 fs) matches closely to the lifetimes of Ni_3O (~172 fs) which may release O to form Ni_3.[91] Further, Ni_3O_2 and Ni_3O show similar lifetimes and γ values, suggesting a similar excited state landscape. The Ni_3O_3 cluster is ferromagnetically coupled, showing 0.3 spin on every atom.
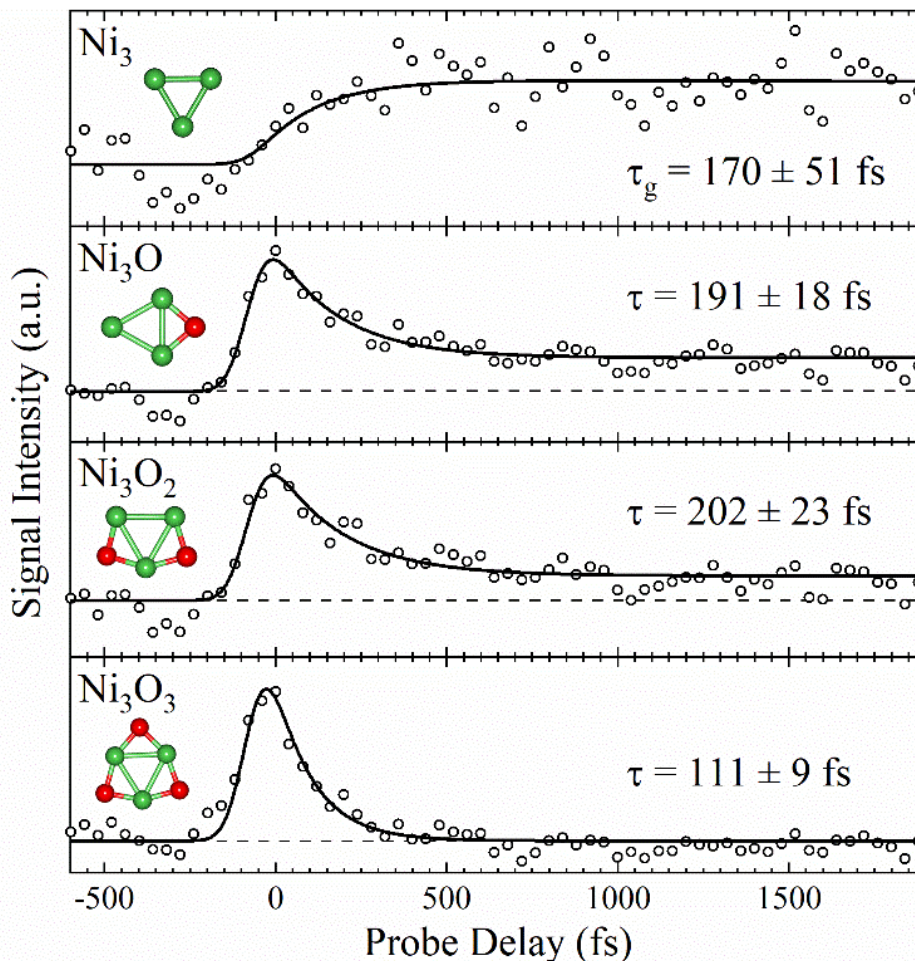
Figure 4.4: Pump-probe transients of the Ni_3O_n ($n < 4$) cluster series with lifetimes shown in each frame, and growth time (τ_g) shown for Ni_3.

Ni_3 was not observed from the photofragmentation of oxygen rich nickel oxide cations, suggesting that it is not a common product of direct dissociation.[90] Further, they looked at only O rich clusters. Ni_3O is not a particularly intense cation peak in other experiments and suggests that it is particularly fragile and has a low fragmentation energy matching the pump photon energy. The excited states of Ni_3 are suggested to be similar to Ni_2, [101,103] with $d\pi_g \rightarrow p\pi_u$ (bound) and $s\sigma_u \rightarrow s\sigma_g$ (dissociative) transitions near 400 nm. However, in contrast to Ni_2, the Ni_3 ion signal does not rise with the laser pulse but instead exhibits a delayed growth ($\tau_g \sim 170$ fs). This growth is a strong signature of an ion

that is not present in the neutral molecular beam but arises following the photodissociation of a larger cluster. My experiment cannot conclusively identify the parent cluster responsible for the growth recorded in Ni_3^+ signal, but several possibilities exist.

The growth lifetime of Ni_3 (170 ± 51 fs) matches closely with the decay lifetime of Ni_3O (~191 fs), suggesting that Ni_3O relaxes to an intermediate dissociative neutral state that releases O to form Ni_3 or remains bound before being ionized to Ni_3O^+ or Ni_3^+ + O. However, calculations predict a bond dissociation energy of 4.2 eV for Ni_3O and suggests it is stable.[106] This dissociation energy may be overestimated, or the Ni_3^+ could arise from fragmentation of a high energy isomer. However, the Ni_3 signal is only ~5% the intensity of the change in Ni_3O signal suggesting they are not related. Alternatively, the photodissociation of Ni_3O_2 to form Ni_3 is also unlikely, requiring removal of two O atoms. Higher energy isomers of Ni_3O_2 containing a bound O_2 unit show dissociation energies in this range.[107] However, Ni_3 is not observed as a product from the photofragmentation of oxygen rich nickel oxide cations.[90] Finally, the most likely situation is that Ni_3 dissociates at the temporal overlap of both laser beams where a dissociative cation state is reached. Ni_n clusters have binding energy per atom below the energy of a 400 nm photon.[104,105,108] Thus, Ni_3 may dissociate at the pulse overlap before decaying to a steady intermediate state in ~170 fs. Supporting calculations show that Ni_3 photoexcitation is strictly Ni-3d $\rightarrow$ Ni-4p, where the p electron density is equally distributed amongst the Ni atoms and supports the argument that Ni-p excitations are long lived.

Similar to Ni_2O_n and Ni_3O_n clusters, the Ni_4O_n (n = 2-4) series shows an increased relaxation time with decreased oxidation (Figure 4.5). The Ni_4O_n series is 3D, with the Ni atoms forming a tetrahedral core, except for the stoichiometric cluster which is planar and has a no net spin. The O atoms attach to the periphery of the cluster and bond to three Ni atoms. The suboxide clusters show strong Ni-Ni bonding, decorated with O atoms on the outside.
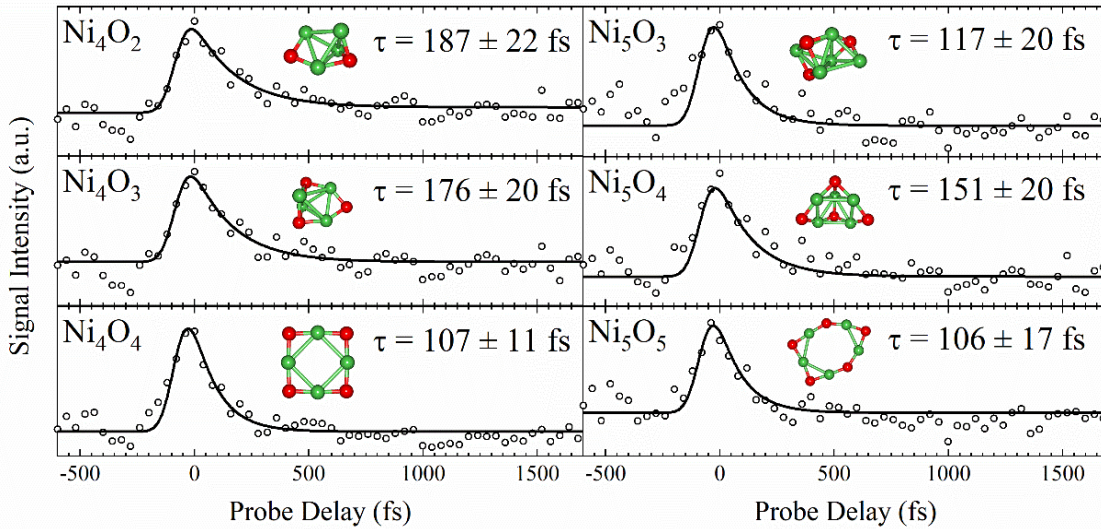
Figure 4.5: Pump-probe transients of the Ni_4O_n (n = 2-4) and Ni_5O_n (n = 3-5) cluster series with cluster geometry and sub-ps lifetime shown.

The Ni_5O_n (n = 3-5) cluster lifetimes generally increase with decreased O content (Figure 4.5), following the trend of smaller nickel oxides. Clusters with more than 5 Ni atoms contain a 3D structure, with larger stoichiometric clusters not recorded with significant intensity. Ni_6O_4 has an exceptionally long lifetime compared to the other clusters (225 ± 40 fs), and also forms a uniquely high C_3 or T_d symmetry,[91] which may facilitate the delocalization of charge carriers for a prolonged lifetime.

The stoichiometric clusters exhibit the shortest lifetime from Ni_{1-5} and conform to similar fast (~100 fs) lifetimes. Cluster geometries take on a similar form with less

55

geometric reconfiguration dependent upon oxidation. However, decreased O content results in reduced symmetry, causing more localized charge-carriers which extends both the fast sub-ps lifetime and allows for charge-trapping (long-lived state). As cluster grow in size, the delocalization of the excited electron and hole results in similar instantaneous excited state lifetimes on the order of 100 fs, similar to e-e scattering in bulk.

4.3 Conclusion

Neutral gas-phase NiO clusters were produced using laser ablation and the femtosecond response to two-color pump-probe photoexcitation was explored. Stoichiometric clusters possess ~100 fs lifetimes which are attributed to efficient charge-carrier recombination and e-e scattering from a Ni d-electron to Ni d- or s-electron orbital, similar to bulk-scale material lifetimes. With the absence of a single O atom from the stoichiometric $(NiO)_n$ cluster, all cluster lifetimes are shown to increase by over 20% and often include a long-lived state that is accessed for >2.5 ps, attributed to an increased Ni d→p transition character. Extended excited state lifetimes facilitate magnetic and chemical transformations and are therefore essential to bulk-scale materials. Due to the multiple states between 1 and 3 eV[92] which is below the pump energy of 3.1 eV, there is not a large deviation in relaxation lifetimes compared to other cluster experiments.[109,110]

This experiment suggests that a purely crystalline NiO lattice results in efficient instantaneous charge recombination, and O vacancies likely result in slower relaxation, allowing for chemical and magnetic manipulation. This experiment shows time-resolved excitation experiments of neutral nickel oxide clusters and will aid in the understanding of excited state lifetimes following UV photoexcitation, creating more advanced nickel oxide materials.

CHAPTER 5

OSCILLATION IN EXCITED STATE LIFETIMES OF

NEUTRAL $(TiO_2)_n$ ($n < 10$) CLUSTERS

Portions of this chapter reprinted with permission from the *J. of Phys. Chem. Lett*. 2021,

12, 16, 4098-4103. Copyright 2021 American Chemical Society and

portions reproduced from *J. Chem. Phys.* (in press) (2021);

https://doi.org/10.1063/5.0071264, with the permission of AIP Publishing

5.1 Introduction

Titania (TiO_2) is widely used due to its abundance, stability, low-cost and

nontoxicity. These properties make it favorable for applications such as water

splitting,[111,112] dye-sensitized solar cells,[113,114] white pigments,[115] environmental

degradation of organic pollutants,[116] and heterogeneous photocatalysis.[117] TiO_2 is an

archetypal photocatalytic materials and serves as a model system for fundamental studies

on the relationship between nuclear dynamics and the generation, transport, and trapping

of charge carriers (electrons and holes) following photoexcitation. Absorption of a photon

with energy exceeding the optical gap results in exciton formation, or bound electron-

hole pair. Excitons can radiatively recombine or return to the ground state via

nonradiative routes such as internal conversion, where excess energy dissipates as

phonons or vibrations. The formation of photogenerated electrons and holes in titania is

accompanied by lattice vibrations (phonons) that are quasiparticles collectively known as

polarons. Small polaron formation occurs spontaneously in perfect lattices and acts to

trap mobile carriers at recombination centers, decreasing their mobility[118] and affecting

57

photoconversion yields.[119] Polaron formation ultimately impacts excited state dynamics, yet its detailed influence over lifetimes is not resolved.

A major limitation for bulk titania is the large bandgap which limits electron transport. Defect engineering has become a major focus for titanium oxides, where oxygen deficient materials contain a smaller bandgap, increasingly delocalized density of states (DoS)[120,121] and therefore can utilize more of the sun's visible spectrum. Suboxides of titania, referred to as Ti_nO_{2n-x} (x > 0), are easily produced from bulk TiO_2 materials,[122–124] are non-toxic,[125] possess unique optical properties,[124,126] and may have increased catalytic activity over their stoichiometric counterpart.[123,127] In particular, Magnéli phase titanium oxides (Ti_nO_{2n-1}, n = 4-9) display enhanced electrical conductivity[128] and increased stability over stoichiometric titania.[129] The overall reactivity of bulk titanium oxides is thought to be heavily dependent on O vacancies and associated Ti^{3+} sites,[130] yet a precise understanding of their influence on the behavior of excitons, polarons, and free charge carriers in titania is needed.

Among the most important aspects of catalytic efficiency is the production of a photoexcited state with sufficient lifetime to enable chemical transformation. Ultrafast recombination of electrons and holes is the major efficiency loss mechanism and depends on strong electronic and electron-lattice correlations. Despite identical chemical compositions, the common polymorphs of bulk TiO_2 (rutile, anatase and brookite) exhibit different photocatalytic activities,[131] highlighting the critical role of local structure on the flow of energy. Polaron formation is favorable in the rutile phase, with carrier recombination two orders of magnitude faster than the anatase phase, where polaron formation is unfavorable and electrons remain delocalized.[132,133] Polaron formation in

58

nanomaterials can accelerate electron/hole recombination through exciton self-trapping. Quantum confinement effects have not been observed in titania nanoparticles[134] as the sub-nanometer exciton binding radius[135,136] is smaller than the particle. The small exciton binding radius in titania makes sub-nanometer clusters the ideal venue for identifying the structural factors that govern carrier dynamics, electron-hole recombination mechanisms and related excited state lifetimes.

Despite extensive research on TiO_2 nanoparticles, the excited state lifetimes at the ultimate size limit (clusters) had not yet been measured prior to this study. Femtosecond pump-probe spectroscopy is used to measure the excited state lifetimes of sub-nanometer titania clusters and apply computational studies to relate the dynamics to electron-hole separation and recombination.

5.2 Results and Discussion

Neutral clusters were produced through ablation of a Ti rod in the presence of a seeded He gas pulse (1% O_2). Mass spectra were recorded using 400 nm pump and 800 nm probe pulses of 9.9 x 10^{14} W/cm^2 and 3.1 x 10^{15} W/cm^2 intensity, respectively. An average of 200 shots per time step were recorded as the probe was delayed from -1.6 – 6.8 ps. All transient signals were fit using a combination of two Gaussian functions convoluted with an exponential decay to account for the relaxation lifetimes.[17,19]

5.2.1 Cluster Distribution

Ionization of the neutral titanium oxide molecular beam by the 400 nm pump and 800 nm probe lasers at temporal overlap produced a mass spectrum of Ti_2O to $(TiO_2)_{11}$ (Figure 5.1). The primary clusters recorded follow the series of Ti_nO_{2n-x} (x = 0-3) and grow through addition of TiO_2 units.
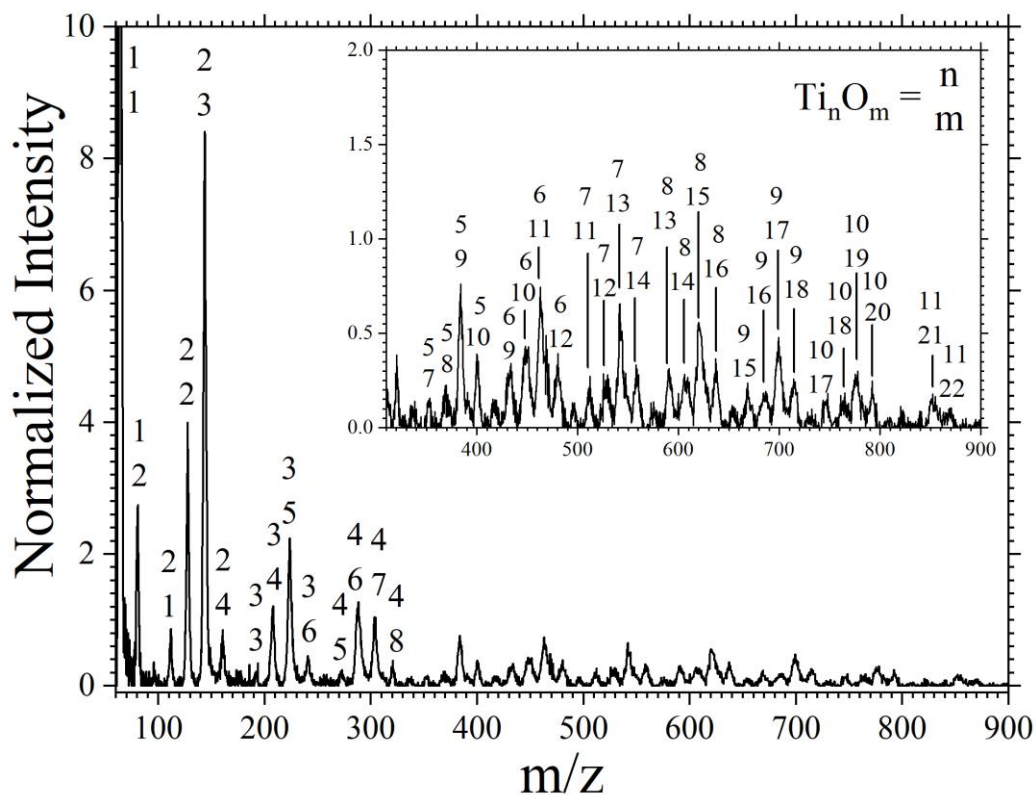
Figure 5.1: Ionized neutral titanium oxide cluster distribution at temporal overlap.

The cluster distribution is consistent with previous studies,[137] with the highest intensity peaks generally composed of Ti_nO_{2n-1} or Ti_nO_{2n-2}, and is in agreement with their stabilities.[138] Neutral stoichiometric (Ti_nO_{2n}) clusters have previously been recorded experimentally only using single photon (VUV) ionization thought to be void of fragmentation,[139] supporting that fragmentation is not significant in this experiment. Thus, the formation of O deficient clusters is due to kinetic limitations during the growth of clusters in the ablation plasma.

5.2.2 Size Effect on Stoichiometric $(TiO_2)_n$ Cluster Lifetimes

All clusters contain a fast (~35 fs) and a sub-picosecond relaxation component (Figure 5.2). The fast lifetime is attributed to an increase in signal that occurs through non-resonant excitation/ionization. As the laser pulses separate in time, the remaining ion

signal is proportional to the neutral cluster's intermediate excited state population. The sub-picosecond excited state lifetime (τ) is attributed to rapid internal conversion returning to the S_0 state. The signal returns to baseline for all clusters, suggesting that carrier recombination is efficient for these sub-nm materials. The measured excited state lifetimes oscillate with addition of TiO_2 units for cluster sizes from n = 1-7, with larger lifetimes observed for even-numbered clusters. Lifetimes gradually increase with size from 256 fs for n = 1 to ~550 fs for n > 6. Differences in excited state lifetimes are attributed to small changes in the local environment of each cluster that affect polaron formation.

All clusters contain two terminal O atoms bound to a tetrahedral Ti atom, in agreement with literature assignments for the global minimum structures of $(TiO_2)_n$.[112,140–147] The stable conformations of clusters n > 4 possess all tetra-coordinated Ti atoms. Odd numbered clusters adopt C_s symmetry and even clusters adopt C_{2v} or C_{2h} symmetry. Stoichiometric $(TiO_2)_n$ are characterized as closed shell systems, where each O atom withdrawals two d-electrons from the Ti atoms, leaving the cluster void of d-electrons. Photoexcitation moves an electron from the occupied O 2p orbitals back to the unoccupied Ti 3d orbitals, analogous to the band structure of bulk TiO_2. The cluster's ionization potentials (IPs) and optical gaps have not been experimentally measured but were calculated to be ~10.0 ± 0.5 eV[141] and ~4.5 eV,[140] respectively. These results are consistent with photoexcitation by two pump photons (6.3 eV). The probe beam is maintained at threshold intensities to ensure the excess energy in the cations is less than a single probe photon (1.55 eV) and below the cation fragmentation energy.[141,148]

Excited state lifetimes are governed by electron-hole interactions, the magnitude of the transition energy, and nuclear motion. Time-dependent density functional theory (TD-DFT) calculations were performed to explore the excited states at the ground state (S_0) and adiabatically optimized excited state geometry (S_1). For simplicity, I limit analysis to the S_1 state as a general description of photoexcitation. The S_1 state is the final state along the relaxation pathway and contains the biggest energy gap, suggesting it is the rate limiting step in relaxation. The large density of states and vibrational modes enables rapid internal conversion to the S_1 state in accordance with Kasha's rule.[149]
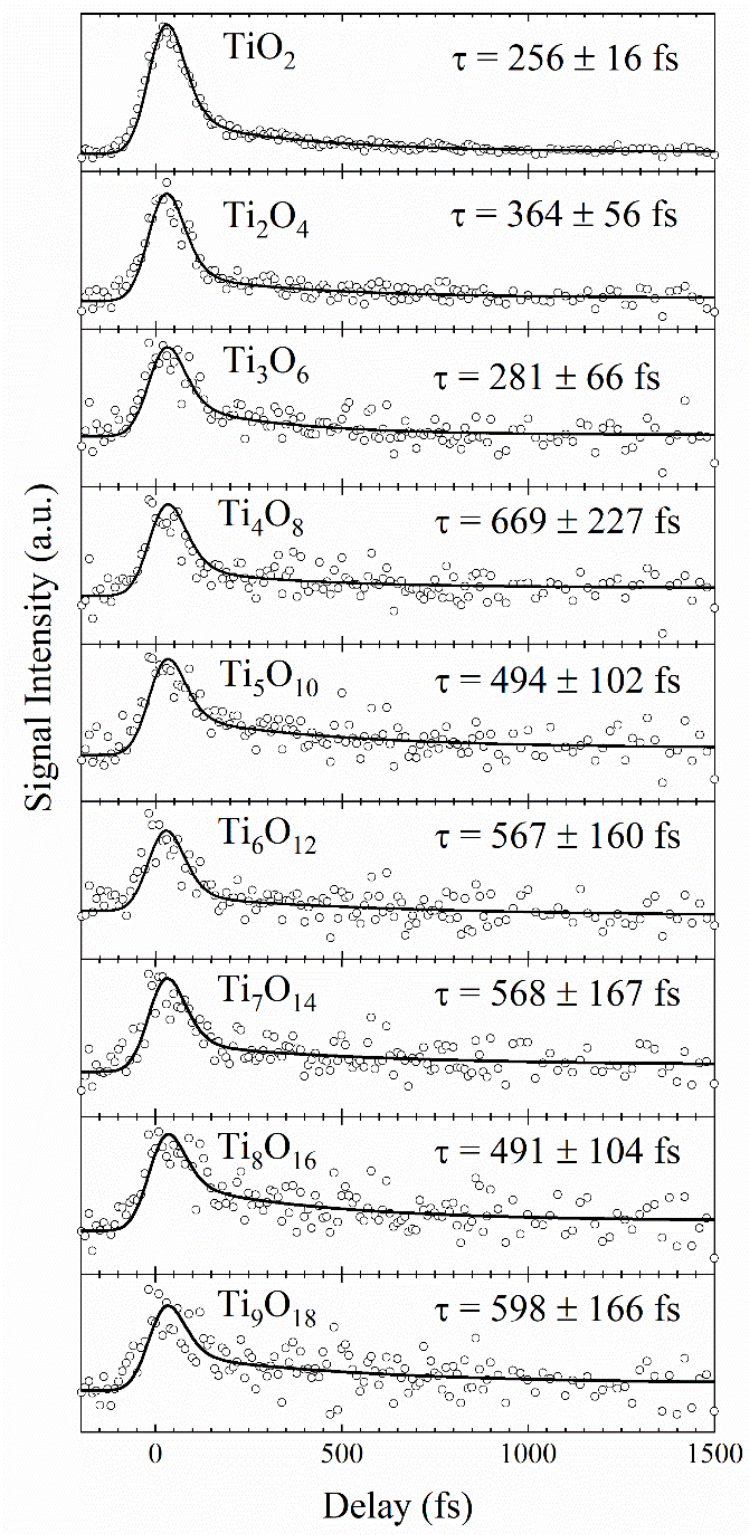
Figure 5.2: $(TiO_2)_n$ cluster (n < 10) pump-probe transients with lifetime shown in each frame.

63

To interpret the role of the electron-hole interactions on excited state lifetimes, several topological descriptors were calculated at both vertical excitation (S_0) and upon adiabatic relaxation to the S_1 minimum energy. Photoexcitation involves several molecular orbitals, making transition densities an efficient representation of the location and distribution of holes and electrons. The Λ index quantifies the charge-transfer character of excited states (Λ_1) as the spatial overlap of electron and hole wavefunctions,[150–152] and ranges between 0 and 1 to describe wavefunctions that share no common space or complete overlap, respectively. Low Λ values suggest that the exciton obtains a strong charge transfer character upon excitation and further increases on the S_1 landscape. The distance between electron and hole density centroids (d_{e-h}) is a complementary approach to measuring the charge-transfer length.[153] Although Λ and d_{e-h} are traditionally thought to relate to recombination lifetimes, neither parameter reconciles with the experimental lifetimes, shown in Table 5.1. Both values are small, revealing that charges often localize on neighboring atoms without overlapping, thus demonstrating a large ionic character. These parameters are not reliable for such ionic systems and are poor predictors of excited state lifetimes for $(TiO_2)_n$ clusters.

Upon photoexcitation, subtle changes in both the local geometry and electronic structure enable carrier localization and polaron formation which accounts for the measured lifetime oscillation. Theory shows the electronic structures of $(TiO_2)_n$ clusters exhibit an even/odd oscillation with additional TiO_2 units.[112,142,154] Even clusters have larger HOMO-LUMO gaps, IPs, optical excitation energies, and exciton binding energies (E_x). Larger energy spacings are indicative of more stable and rigid structures. The delocalization of each charge carrier is quantified by the total-root-mean-square density

(σ_e or σ_h). The charge carriers are all delocalized upon vertical excitation, but in all cases, they separate (increasing d_{e-h}) and localize (decreasing σ) on the S_1 potential. Pivotal energies and topological parameters with lifetimes are shown in Table 5.1. During adiabatic relaxation, both charge carriers show preference to localize on the least coordinated atoms. The under-coordinated Ti atom, typically found in the center of the cluster adjacent to a highly coordinated O atom, serves as the localization center for the electron density. If the hole overcomes the exciton binding energy, it migrates to a terminal O atom. The relaxation energy (E_R) is the final difference in vertical ionization potential and adiabatic relaxation energy.

Table 5.1: Experimental excited state lifetimes (τ) and calculated properties for $(TiO_2)_n$ clusters.

$(TiO_2)_n$	τ (fs)	Λ	d (Å)	σ_{av} (Å^3)	E_X (eV)	E_R (eV)
1	256 ± 16	0.26	1.73	3.31	5.33	0.11
2	364 ± 56	0.22	2.89	3.54	5.49	0.89
3	281 ± 66	0.14	4.16	2.83	2.69	1.29
4	669 ± 227	0.25	2.45	3.20	3.87	0.99
5	494 ± 102	0.24	1.81	3.11	3.75	0.86
6	567 ± 160	0.30	2.40	3.95	4.30	1.00
7	568 ± 167	0.25	3.90	4.40	4.08	1.00
8	491 ± 104	0.30	1.82	4.28	4.59	0.84
9	598 ± 164	0.35	2.50	4.31	3.89	1.10

Structural rearrangement accompanies charge localization as the clusters relax through a Jahn-Teller (J-T) type distortion on S_1, similar to polaron formation in bulk structures. Due to the tetrahedral coordination of the Ti atoms, this results in a Ti-O bond elongation (Δr_{Ti-O}) which is more pronounced in even numbered clusters. Although polarons are a bulk concept, the language is appropriate even for molecular-scale clusters

due to the local structure deformation and localization of charge carriers. The polaron couples to the vibrational motion of the cluster and facilitates rapid depopulation by a radiationless transition through a conical intersection on the femtosecond timescale. Dangling bonds are known to facilitate internal conversion.[155]

Variation in clusters provides a range of geometric configuration that mimic the active sites of bulk surfaces and can be utilized to understand the coupling between polaron formation and related lifetime changes. The formation of localized charge carriers and Coulomb attraction between the electron and hole drives relaxation. The averaged distribution of the electron and hole (σ_{e-h}) correlates with the measured lifetime of TiO_2 clusters (Figure 5.3). In general, the odd numbered clusters are more planar in nature and exhibit shorter lifetimes than the even clusters. The higher symmetry and rigidity of even numbered clusters presents a more delocalized energy landscape where the S_0 transition density is distributed across all atomic centers, except those directly bound to the terminal O. Upon relaxation, the even clusters show larger carrier delocalization (σ) that inhibits nonradiative decay pathways leading to longer lifetimes.

The smallest three clusters are planar, feature under-coordinated Ti atoms, and exhibit the shortest lifetimes. TiO_2 and $(TiO_2)_2$ are too small to enable separation and therefore have large E_X. Following excitation, $(TiO_2)_2$ adopts a more planar geometry as the hole localizes on a terminal O atom. $(TiO_2)_3$ is unique in that it contains a three-fold coordinated Ti and O. The electron density moves onto the 3d orbital of the under-coordinated Ti atom and the hole localizes on the opposite side of the cluster. $(TiO_2)_3$ has the smallest S_1 energy gap, and the largest E_R which are strong drivers for recombination.

Relaxation on the S_1 landscape localizes the hole to one terminal O and has the smallest bond extension of all clusters.
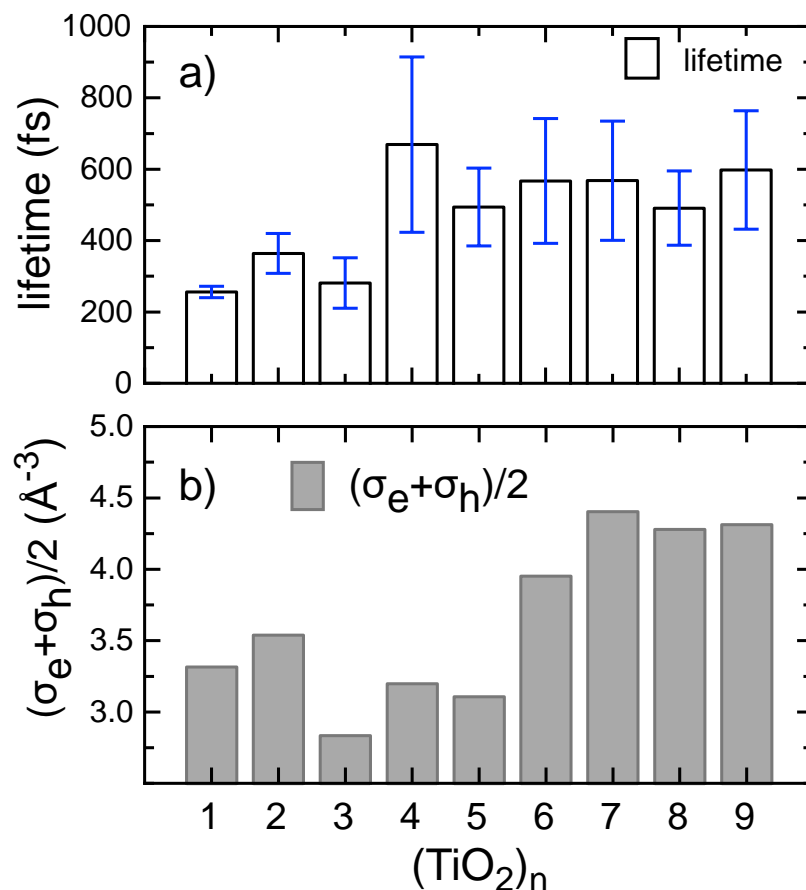
Figure 5.3: Comparison between a) the lifetime of $(TiO_2)_n$ clusters and b) the average delocalization between the electron and hole of each cluster.

An increase in lifetime occurs as the clusters move to a 3D structure and feature Ti atoms that are all tetracoordinated. Both $(TiO_2)_4$ and $(TiO_2)_5$ structures contain a tetra-coordinated O atom with ionic character which provides rigidity.[141] Upon adiabatic relaxation, the electron of $(TiO_2)_4$ localizes on one Ti, but the hole behaves as a multi-site polaron distributed about two O atoms causing a large local bond elongation. On the S_0 landscape of $(TiO_2)_5$, the electron resides on the Ti furthest from the terminal O, the hole arises from the three adjacent O atoms, while the majority of the cluster is inactive. Upon

adiabatic relaxation on S_1, the hole localizes to one O forming an exciton pair that reduces the excited state lifetime.

As the cluster size increases above $(TiO_2)_6$, the oscillation is less apparent, and lifetimes approach a similar value. $(TiO_2)_6$ exhibits a low number of vibrational bands,[147] highlighting a rigid structure that contains a tetra-coordinated O in its center. Despite having a collection of hole and electron on adjacent atoms following relaxation, the distortion appears localized to one bond elongation, while the remaining cluster is rigid, hindering localization. Similar to the $n = 4$, $(TiO_2)_6$ does not drive electron localization. $(TiO_2)_4$ and $(TiO_2)_6$ have large local bond elongations of 0.30 Å and 0.27 Å, respectively, prolonging the lifetime.

Both $(TiO_2)_5$ and $(TiO_2)_8$ exhibit relatively low E_R, resulting in a strong localization of both carriers into a bound exciton $(Ti^{3+}-O^-)$ pair, which facilitates internal conversion. The centrosymmetric S_0 state of $(TiO_2)_8$ contains delocalized charge carriers spread over the entire cluster. $(TiO_2)_8$ has the largest E_X, where the S_1 structure migrates the electron and hole to adjacent atoms in the middle of the cluster and contains a large Λ_1, supporting a shortened lifetime. Both of these clusters have a ''glassy'' energy landscape and exhibit a large number of low-energy isomers.[143] Their flexible structures enable charge localization and rapid relaxation.

In $(TiO_2)_7$ and $(TiO_2)_9$, the hole migrates to a trapped site, leaving a delocalized electron in the core of the cluster due to a small E_{ex}. In $(TiO_2)_7$, both charge carriers are delocalized, but on opposite ends of the cluster. The S_1 relaxation mechanism is similar to $(TiO_2)_2$, where the hole localizes on the terminal O and becomes more planar. The remaining cluster is unperturbed, inhibiting electron polaron formation ($\sigma_e = 5.86$ Å). This

separation reduces the electron-hole overlap ($\Lambda_1 = 0.25$) and slows recombination to break the oscillating trend, showing a similar lifetime to $(TiO_2)_6$. The breakdown in oscillation occurs at similar size regime as the onset of bulk-like energy gaps.[136] $(TiO_2)_9$ contains a highly coordinated center (six-fold coordinated Ti and several tri-coordinated O atoms) that attracts both charge carriers on S_1. The electron does not localize, but the hole forms a multicenter polaron with similar lifetime.

The cluster's excited-state lifetimes reach a steady value as they approach the ~1 nm size regime, with similar values (τ~550 fs) recorded for clusters of $n \geq 7$. The tightly bound electron-hole pairs are consistent with the sub-nanometer exciton binding radius found in bulk structures. The oscillation in lifetimes as clusters grow in size is attributed to structural differences between the clusters that control charge localization and polaron formation. Time-dependent density functional calculations show the increased lifetime for even clusters is associated with a more rigid structure, lower electron-hole pair localization, and extended bond lengths. Polaron formation is highly dependent on local structure and shortens excited state lifetimes. Therefore, the utilization of rigid structures accompanied by bond elongation and delocalized polarons is essential for the production of titanium oxide materials with longer excited state lifetimes.

5.2.3 Oxidation Effect on Titanium Oxide Lifetimes

Surprisingly, despite the large changes to the electronic and structural characteristics of the clusters as they gain and lose O atoms, their excited state dynamics remain roughly consistent. The transient signals for all clusters contain a fast (35 fs) response and a sub-ps relaxation lifetime (τ). No long-lived states are recorded, and the ratio of fast/sub-ps fitting coefficients (κ) are similar (Table 5.2). These similarities

suggest that the sub-nm scale is perhaps the most important feature, and that relaxation is dominated by exciton recombination, which is efficient in these sub-nm clusters due to the restricted proximity of their diameter. The fast component of the transient signal is attributed to a rapid relaxation of a nonresonant excited state. The remaining sub-ps transient ion signal is proportional to the neutral cluster's intermediate excited state population as it relaxes to the ground state.

Despite the similarities, each cluster series exhibits a unique trend as they grow in size. A near linear increase in lifetime occurs with size in Ti_nO_{2n-1} clusters up to n = 7, with the exception of Ti_6O_{11} (Figure 5.4b). All clusters in this series (except Ti_6O_{11}) contain all tetra-coordinated Ti atoms with Ti-Ti bonds forming to stabilize the reduced Ti atoms.[138] Thus, the tri-coordinated Ti site of Ti_6O_{11} may retain additional d-electrons that facilitate a faster decay, deviating from the trend. The Ti_nO_{2n-2} clusters are more compact, given the absence of any terminal O atoms, and universally have shorter lifetimes. The Ti_nO_{2n-2} cluster series of n ≥ 4 shows an oscillatory nature (Figure 5.4c), where odd-numbered clusters have a longer lifetime over even-numbered clusters due to a higher localization of charge carriers. The lifetimes of the Ti_nO_{2n-3} series also alternate with increasing cluster size and is most pronounced for the smallest cluster sizes (Figure 5.4d). Both oxygen-deficient series exhibit the opposite behavior from the Ti_nO_{2n} series, where even-numbered clusters exhibited longer lifetimes than odd-numbered clusters.[109]
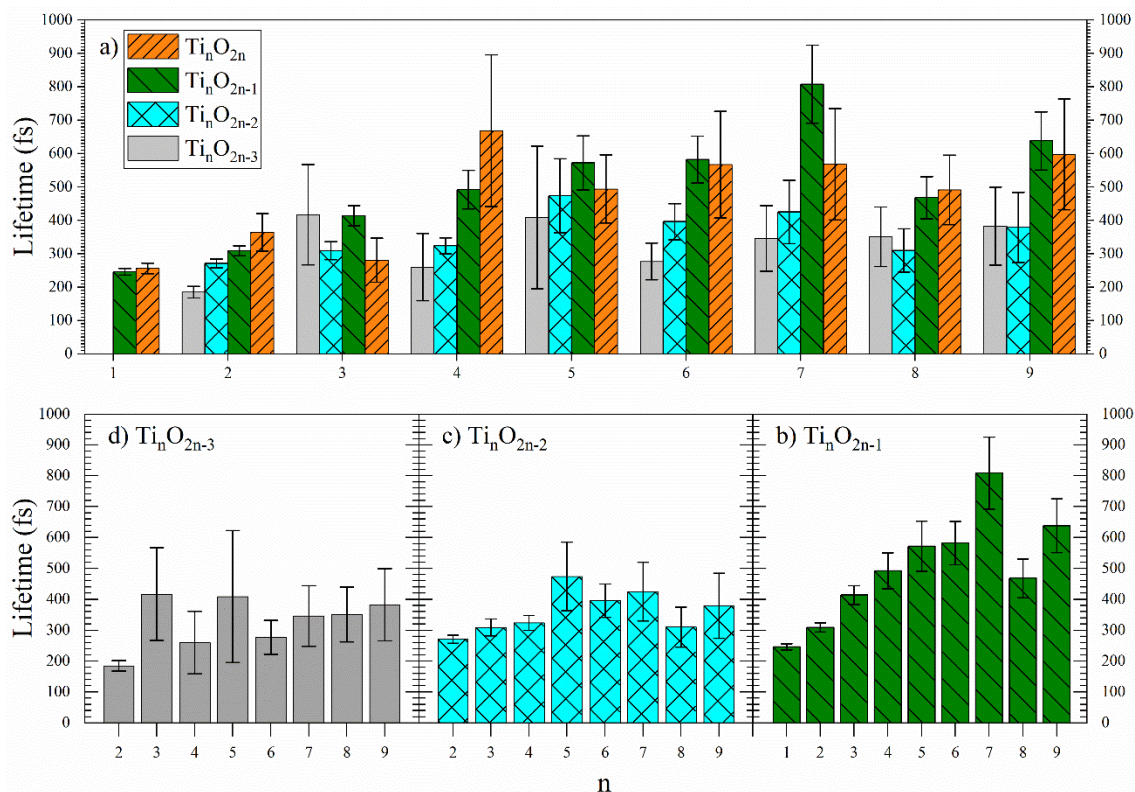
Figure 5.4: The lifetimes of all Ti_nO_{2n-x} clusters (a) showing the Ti_nO_{2n} (orange close slashed lines), Ti_nO_{2n-1} (green sparse slashed lines), Ti_nO_{2n-2} (cyan crossed lines), and Ti_nO_{2n-3} (solid grey) series. Separate plots are shown for b) Ti_nO_{2n-1}, c) Ti_nO_{2n-2}, and d) Ti_nO_{2n-3} series.

The oxidation states of the Ti atoms are commonly assumed to involve complete electron transfer, where each O atom removes 2 electrons from the Ti atoms. Removal of each O atom from the stoichiometric cluster returns two d-electrons to the Ti atoms. Therefore, the suboxides contain many delocalized d-electrons that should influence the metallicity and consequently relaxation dynamics of the cluster. Unfortunately, measurements of metallic behavior, such as conductivity, are not possible for clusters of just a few atoms. Another indicator for metallicity is short excited state lifetimes[21,25,156] and has been well established for small metal clusters.[157–161] Metallic and nonmetallic properties can be identified by the different relaxation behaviors of optically excited states. Strong interactions between delocalized valence d-electrons causes relaxation in

71

metallic species on the fs timescale via Auger-like electron–electron scattering, whereas a weak coupling between electronic excitation and nuclear motion facilitates long (picosecond or longer) lifetimes of electron-hole characteristics in non-metallic semiconductors. Metallic scattering processes dominate if there are many delocalized electrons and a sufficiently high DoS, such as is the case even in small clusters. Thus, the relaxation by electron scattering processes results in many electrons occupying low-lying excited states, similar to the bulk.

However, internal conversion is an alternative possible pathway of relaxation and cannot be ruled out as contributing here. Small molecules can exhibit excited state lifetimes on the order of 10s of fs, particularly when there is passage through a conical intersection between two potential energy surfaces. Despite the well-known role of dangling O atoms in facilitating energy relaxation through conical intersections,[155] clusters void of terminal O atoms exhibit similar lifetimes to those with them. This suggests that internal conversion is not driving the relaxation. Further, the clusters are sufficiently small such that electrostatic interactions between the hole and electron are efficient for recombination.

The transient signals of neutral Ti_2O_{4-x} (x < 4) clusters reveal an increase in excited state lifetimes with oxidation (Figure 5.5). Here, each O atom changes the oxidation state of the Ti atoms linearly, from a formal oxidation state of +3 (Ti_2O_3) and +2 (Ti_2O_2) which decreases the lifetime by 15% and 26% from the stoichiometric cluster, respectively. Geometries of Ti_2O_{4-x} (x < 4) clusters are well established.[138,148] Ti_2O_4 is the least rigid cluster (containing two terminal O) and therefore should be the easiest to traverse a conical intersection since internal conversion is less effective in rigid clusters.

72

Yet, it contains the longest lifetime of the series. In contrast, the more rigid ring structure of Ti_2O_2 contains no dangling O atoms and has a faster relaxation, suggesting that internal conversion is not the dominant relaxation mechanism occurring here. Although the number of relaxation pathways decrease with the removal of O atoms, the bond distances shorten[22] and d-orbital occupancy increases, resulting in a faster relaxation. This influence of O content on lifetime aligns with a metallic to insulator transition occurring with oxidation. Thus, my data supports that relaxation in clusters occurs via Auger-like electron scattering processes similar to bulk metals.
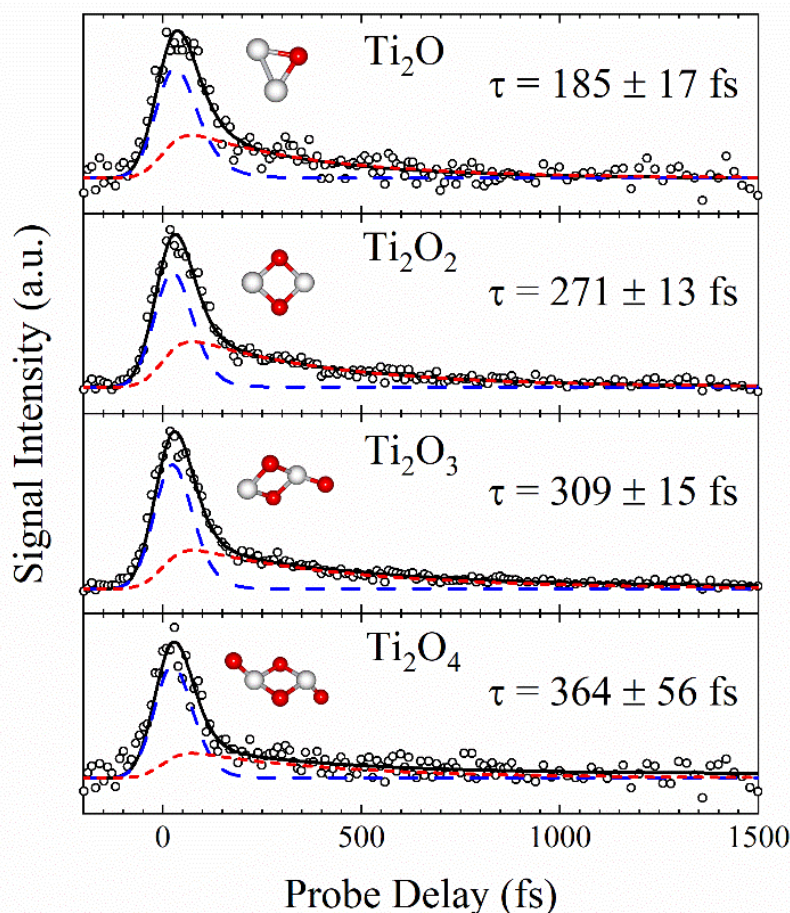
Figure 5.5: Ti_2O_{4-x} ($x < 4$) cluster transients with total fit (black), fast (35 fs) decay (blue long dash) and sub-ps (red short dash) component shown. The sub-ps lifetime is shown for each transient.

The transient response to O vacancies in the Ti_3O_{6-x} (x < 4) clusters is different than the other cluster series (Figure 5.6). The fully oxidized cluster, Ti_3O_6, has the shortest excited state lifetime in the Ti_3O_n series, while Ti_3O_3 shows a longer lifetime. However, the Ti_3O_3 transient contains an unreliable sub-ps component with high experimental error. Ti_3O_6 is unique among the stoichiometric clusters in that it contains a tri-coordinated Ti atom and tri-coordinated O atom, which are not present in other stoichiometric (n < 6) structures.[121,162,163] The tri-coordinated Ti atom sites are common in clusters exhibiting suppressed lifetimes. Ti_3O_5 exhibits a slightly longer lifetime, even though it is further undercoordinated, due to presence of partially filled d-orbitals which are delocalized across two Ti atoms. In general, the delocalization of the d-orbitals is correlated with extended lifetimes in suboxides.
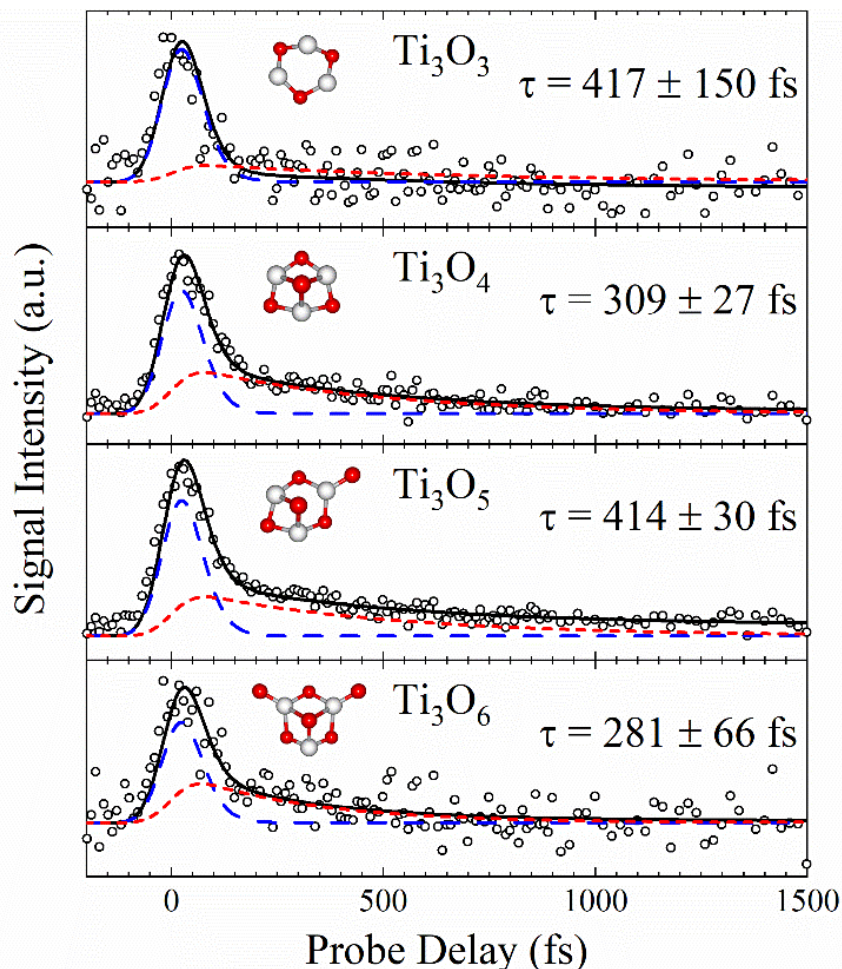
Figure 5.6: Transients of the Ti_3O_{6-x} (x < 4) cluster series with fast (35 fs) lifetime (blue long dash), sub-ps lifetime (red short dash) and total fit (solid black). The sub-ps lifetime is shown in each frame.

Similar to the Ti_2O_{4-x} clusters, Ti_4O_{8-x} (x < 4) clusters also highlight an increased lifetime with oxidation (Figure 5.4a), supporting a metallic to semiconducting transition. Ti_4O_{8-x} (x < 4) clusters have 3D structures with the Ti atoms forming a tetrahedron core and O atoms bridging the Ti atoms or as terminal groups for Ti_4O_7 and Ti_4O_8. The T_d symmetry of Ti_4O_6 lacks terminal O atoms and also contains an increased number of d-electrons which manifest in a large decrease in lifetime. Ti_4O_5 is similar to Ti_4O_6 but contains one less bridging O atom that reduces the Ti-O coordination and decreases the Ti-Ti bond length, resulting in a slightly shorter lifetime. Although there is minimal

75

Table 5.2: The observed lifetimes of the Ti_nO_{2n-x} $(x < 4)$ series from n = 1-9 and fitting function ratio (κ).

Cluster Series	n	Lifetime (fs)	κ
Ti_nO_{2n-1}	1	246 ± 10	3.4
	2	309 ± 15	4.6
	3	414 ± 30	5.7
	4	492 ± 58	6.0
	5	572 ± 81	5.5
	6	582 ± 70	5.8
	7	808 ± 117	5.7
	8	468 ± 63	4.4
	9	638 ± 87	4.6
Ti_nO_{2n-2}	2	271 ± 13	3.3
	3	309 ± 27	4.3
	4	324 ± 24	3.9
	5	474 ± 111	5.7
	6	396 ± 54	5.3
	7	425 ± 95	5.4
	8	310 ± 65	3.3
	9	379 ± 105	3.9
Ti_nO_{2n-3}	2	185 ± 17	1.4
	3	417 ± 150	14.8
	4	260 ± 101	5.3
	5	409 ± 214	9.0
	6	277 ± 55	4.0
	7	346 ± 98	5.1
	8	351 ± 89	6.4
	999	383 ± 117	5.8

change in geometry in Ti_4O_{8-x} $(x < 4)$ clusters, a higher d-orbital occupancy occurs with decreased O atoms from Ti_4O_8,[163] resulting in a linear decrease in the lifetime of charge carrier recombination.

Lifetimes of Ti_5O_{10-x} $(x < 4)$ clusters do not change significantly with O (Figure 5.4a). The similar lifetimes are due to a similar C_s symmetry and align with the size

transition between local and global excitations, where charge carrier delocalization no longer fills the cluster diameter. Further, Ti_5O_{10} exhibits a slightly reduced lifetime in the stoichiometric series, bringing the dynamics closer to Ti_5O_9. Interestingly, several stoichiometric clusters exhibit shortened lifetimes that deviate from the proposed metallic trend. Ti_nO_{2n} (n = 3, 5, 6) all contain a tri-coordinated Ti atom instead of the fully tetra-coordinated Ti atoms of the other clusters, and therefore may retain d-electrons that reduce their lifetimes. Such incomplete electron transfer leading to an atypical 3+ oxidation state is proposed for clusters as small as TiO_2.[164]

Larger clusters (Ti_nO_{2n-x}, n = 6-9) follow similar trends in excited state behavior (Figure 5.4a). Generally, the Ti_nO_{2n-1} and Ti_nO_{2n} clusters show longer lifetimes, and exhibit similar lifetimes due to related structures and possibly incomplete electron transfer, leading to retention of d-electrons on the stoichiometric cluster.[121] Further, in Ti_nO_{2n} clusters, the excited state avoids localization on the Ti atoms with terminal Ti-O bonds,[109] which ensures that the excited states behave similarly in the various O deficient clusters and accounts for the minimum influence of lifetime with oxidation. Clusters without terminal O atoms (Ti_nO_{2n-2} and Ti_nO_{2n-3}) show shorter lifetimes and increased Ti-Ti bonding, indicating that the d-electron scattering is a dominant mechanism affecting dynamics and that bridging O atoms have a minor effect on excited state lifetimes.

A particular outlier to the described trends is Ti_7O_{13}, which exhibits a significantly longer lifetime than Ti_7O_{14} (Figure 5.4a). This switched behavior is attributed to its unique structural features, where removal of an O atom from Ti_7O_{14} drives a significant compression of the local Ti-O bonds and creates a hexa-coordinated Ti site adjacent to a tetra-coordinated O atom. This high coordination site may account

77

for its exceptionally long lifetime, in opposition to tri-coordinated Ti sites facilitating fast

relaxation. Further, distinctive to Ti_7O_{13}, the HOMO is distributed across three

neighboring Ti atoms, and further supports the idea that this delocalization of d-electrons

is correlated with lifetime.

Clusters generally exhibit longer lifetimes with higher oxidation and shorter

lifetimes upon removal of O atoms. Although the optical gap of suboxides decreases by

~3 eV from the stoichiometric cluster,[121] it does not have a significant influence on the

excited state lifetime. This suggests that removal of O atoms develops metallic Ti-Ti

bonds of lower coordination, causing the system to transition into a fast scattering-type

electronic relaxation mechanism. This is consistent with the idea that as the clusters

become more metallic, the lifetimes decrease. Excited state lifetimes are modified by

electron-hole interactions which are influenced by Ti bond coordination and cluster size.

These results suggest that enhanced excited state lifetimes in bulk titania materials may

be achieved through manufacturing structures similar to the Ti_7O_{13} cluster that contain

delocalized d-electrons and higher Ti coordination.

5.3 Conclusion

This experiment identifies key molecular-level parameters that can be applied to

aid new synthetic strategies to design materials, surfaces, and coatings with extended

excited state lifetimes and improved photocatalytic performance. The tightly bound

carriers (d < 0.5 nm) are in agreement with simulations of larger nanoparticles.[165] Thus,

slightly increasing the cluster size into the few nanometer size regime will likely not

impact the excited state lifetimes significantly, as the carriers do not utilize all the space

in clusters this small. These clusters capture the important features and therefore are

adequate mimics of bulk systems. The electron localizes on the lowest coordinated Ti, analogous to the electron trapping on under-coordinated Ti^{3+} cation centers that accompany O defect sites on bulk surfaces. Additionally, the electron typically does not localize on a single site unless bound to a hole in an exciton pair. These results suggest that prolonged excited states lifetimes (and related excitons) can be achieved by preparing bulk surfaces that more closely mimic the structural features of the clusters.

The low-lying excited state lifetimes of neutral Ti_nO_{2n-x} (n = 1-9 and x < 4) clusters were measured using fs pump-probe spectroscopy, and trends in their transient signals related to the size and oxidation are presented. An oscillation in lifetimes as clusters grow in size is attributed to structural differences between the clusters that control charge localization and polaron-like formation. The signal returns to baseline for all clusters, suggesting that carrier recombination is efficient for these sub-nm materials. It is shown that the level of coordination increases with cluster size, further increasing excited state lifetimes related to charge carrier localization. The lifetimes show a behavior consistent with a metallic to semiconducting transition with oxidation and related removal of d-electrons from the system. The fundamental information provided herein leads to a deeper understanding of the factors affecting O vacancies in bulk-scale titania materials and will assist in the production of future catalysts of increased reactivity.

CHAPTER 6

INCREASED EXCITED STATE METALLICITY IN NEUTRAL $(CrO_2)_n$ CLUSTERS

(n < 5) UPON SEQUENTIAL OXIDATION

6.1 Introduction

Chromium oxides are widely studied for their magnetic and electronic properties, commonly being employed in magnetic storage devices. In particular, CrO_2 is a well-established half-metal with the highest spin polarization of any material,[166–168] attracting substantial research interest for potential spintronics and data storage applications. This unique half-metallic property in CrO_2 arises from a large energy spin gap, where the delocalized majority spin states close to the Fermi energy are metallic and the minority spins are semiconducting or insulating.[169] Therefore, isolating and controlling the separate spin states to induce (anti)ferromagnetic properties are of increasing interest. The ultimate speed at which its magnetic states can be manipulated is of key importance due to its attractive potential for use in spintronic heterostructures and magnetoelectronic devices requiring spin polarization, such as magnetic tunnel junctions[170] and spin valves.[171] The photodriven process of (de)magnetization and optical spin transport can be manipulated with light on the femtosecond timescale, but follows a complex route of intermediate states accompanying changes in spin and lattice parameters, and is not fully understood.[172] Despite its relevance to industrial technology, controlling the magnetic states in chromium oxides requires more detailed information on oxygen-dependent electronic state dynamics and electron transport.

Atomically precise clusters provide a superior avenue to examine the factors affecting the electronic properties of chromium oxide. Additionally, chromium oxide clusters may be uniquely suitable for spintronics due to a large array of energetically competitive spin configurations.[173–176] In particular, Cr_2O_n clusters have been heavily studied both experimentally and theoretically,[174–178] showing large changes in electronic structure with oxygen content via photoelectron spectroscopy (PES),[174,177,178] and structures in agreement with vibrationally resolved IR spectroscopy.[179–181] The electronic structures of Cr_2O_n clusters arise from a unique mixing of Cr half-filled s- and d-orbitals ($3d^5 4s^1$) with O 2p-orbitals. The properties of chromium oxides are driven partially by superexchange coupling,[173,182] suggesting the charge-transport processes are adiabatic in nature. Manipulation of spin in antiferromagnetic (AF) Cr_2O_3 bulk materials follows several relaxation channels dependent on excitation energy, proceeding over hundreds of femtoseconds to picoseconds.[172,183,184] However, the mixing of Cr and O electrons and their effect on the lifetimes of accessible magnetic states are still not well understood and may improve the manipulation of chromium oxide materials.

Although small Cr oxide clusters have been evaluated to understand the factors which influence their electronic and magnetic properties, time-resolved pump-probe spectroscopy may assist in the understanding of accessible excited states and the lifetimes following photoexcitation. The ultrafast dynamics, which ultimately dictate reactivity in small clusters, may be crucial in understanding the overall complex electronic properties. How the electronic configuration of Cr compared to other transition metals may also aid in a more complex understanding of d-shell reactivity. To this end, two-color pump-probe spectroscopy is used to elucidate the ultrafast excited state lifetimes of Cr_nO_{2n-x} (x = 0-4)

clusters as they grow in size and O content. The trends and lifetimes presented here can further the discussion on factors which influence electronic mixing of Cr and O atoms and their magnetism.

6.2 Results and Discussion

Neutral chromium oxide clusters were produced in the presence of a seeded He gas pulse (9% O_2) using 4.81×10^{14} W/cm^2 400 nm pump and 3.27×10^{15} W/cm^2 800 nm probe pulses. The 800 nm probe pulse was temporally delayed 600 fs prior (-) to the 400 nm pulse and moved in 40 fs increments towards (+) the 400 nm pump pulse, taking an average of 800 shots per time-delay as the probe is delayed 2.5 ps in time.

Chromium oxide clusters were analyzed using a combination of three fitting functions as described in previous sections. However, in addition to the plateau function, two decay dynamics were needed, a single fast (35 fs) and a variable sub-ps decay dynamic, to properly fit the cluster transients. The lifetimes and fitting functions are described in detail below.

6.2.1 Cluster Distribution

Using both the 400 nm pump and 800 nm probe beam at temporal overlap, the averaged neutral Cr_nO_m spectrum following ionization is shown in Figure 6.1.
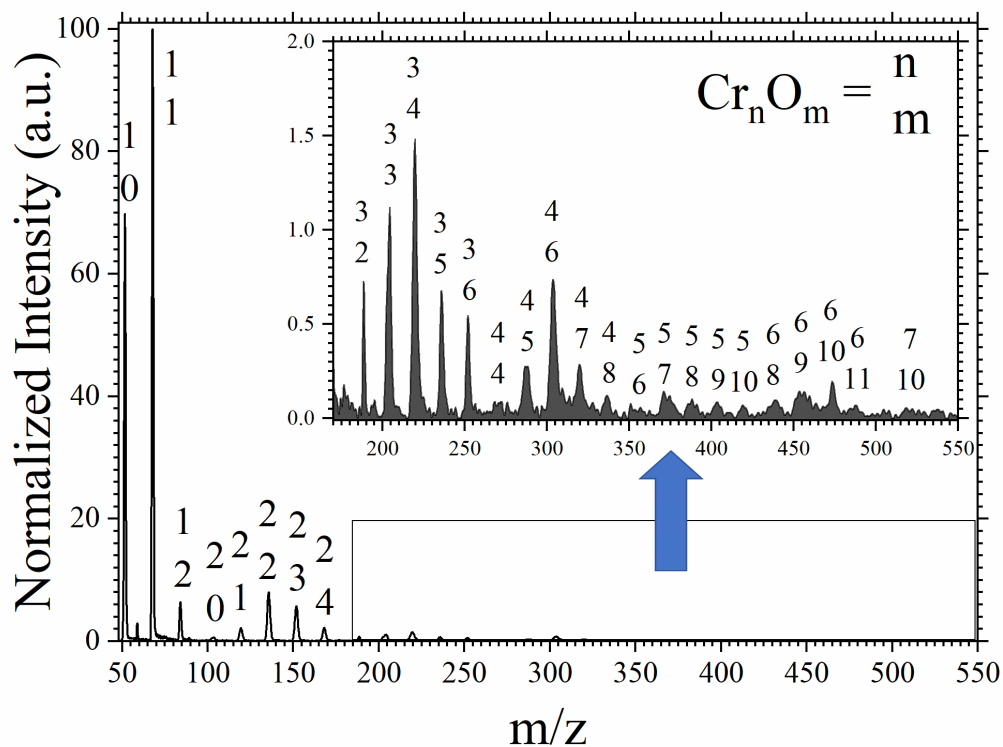
Figure 6.1: Neutral chromium oxide mass distribution at temporal overlap.

Chromium oxides of the composition Cr_nO_{2n} to Cr_nO_{2n-4} are observed up to n = 6.

To my knowledge, gas-phase Cr cluster distributions have primarily shown anions of

Cr_nO_{2n} to Cr_nO_{3n}[185] and cations of Cr_n (n = 3-50) bound to O/O_2.[186] Neutral $(CrO_3)_n$

clusters are highly stable and nonreactive to O_2,[187] while Cr_2O_n (n = 2, 4, 6) clusters form

readily with O_2 and possess multiple stable geometric isomers.[179] Additionally,

photoelectron experiments suggest stable clusters of Cr_nO_{2n} with the absence of O

atoms.[174,177] Therefore, this is the first neutral Cr_nO_m cluster distribution, which has a

preference to form CrO_2 clusters and suboxides with the absence of up to four O atoms.

Photodissociation experiments show $Cr_3O_7^+$, and $Cr_4O_{10}^+$ as major leaving

groups,[188] which are not observed in our mass distribution, supporting the absence of

major fragmentation in this experiment. Additional experiments discuss the alteration of chromium cluster species as a function of laser intensity, showing the production of chromium oxide cations generally composed of CrO_2 with the addition and subtraction of several O atoms.[189] The starting material, laser ablation power, and interaction of ions heavily influences cluster formation. It is expected that higher oxygen species of CrO_3 cluster ions are produced through neutral cluster interactions with O_2,[189,190] suggesting that neutral chromium suboxides of CrO and CrO_2 may be stable after ablation.

In my neutral cluster distribution, the Cr_nO_{2n-1} cluster has the highest intensity (CrO), which quickly drops off below the intensity of Cr_nO_{2n-2} above values of n = 1. The Cr_nO_{2n-2} cluster series remains the highest intensity for values of n = 2-6. $(CrO_2)_n$ clusters possess externally bound O atoms. Although the dissociation energy and ionization potential (IP) typically increases with higher O content in Cr clusters, neutral clusters form symmetrical structures with less dangling O atoms in the gas phase following ablation.

6.2.2 Cr_2O_n Cluster Dynamics

The transient signals of Cr_2O_n (n < 5) reveal three distinct relaxation mechanisms that change with additional O atoms (Figure 6.2). An instantaneous decay (on the timescale of the laser pulse, τ_1 = 30 fs) is attributed to e-e scattering correlated to the ligand-to-metal charge transfer (LMCT), or excitation from O-2p to Cr-3d orbitals. A sub-ps (τ_2) relaxation is attributed to vibrational relaxation of the initially formed charge-transfer state (electron-vibration relaxation). Finally, a plateau function represents a long-lived state (>2.5 ps) that is accessed only in sub-oxide clusters.
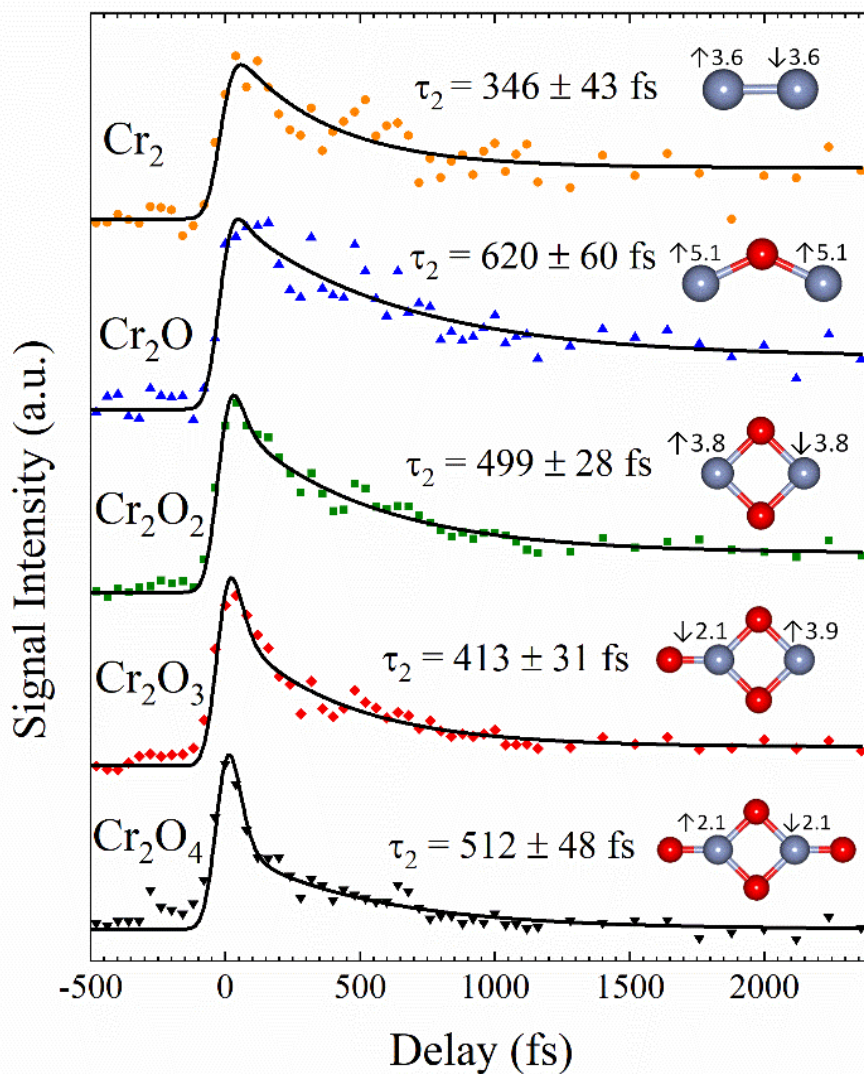
Figure 6.2: Pump-probe transients of Cr_2O_n (n < 5) clusters with total fit shown in black, sub-picosecond lifetime above each fit, and cluster geometry with magnetic moment of each Cr atom.

The Cr_2O_n clusters all exhibit similar instantaneous (τ_1) and sub-ps (τ_2) lifetimes. However, a change in amplitudes of the three fitting functions in each total transient signal with O content is revealed. The fraction of each fitting function amplitude of the total signal is represented as κ_1 (τ_1), κ_2 (τ_2), and δ (plateau function). The lifetimes and fitting coefficients for each cluster are shown in Table 6.1. The relative contributions of the various mechanisms change almost linearly with O content (Figure 6.3). The κ_1

component is not present for Cr_2 but grows to account for 84% of the signal in Cr_2O_4. In contrast, the κ_2 and δ values compose ~70% and ~30% of the total signal for Cr_2, respectively, and both decrease nearly linearly with oxidation.

Table 6.1: Lifetimes (τ_2), signal fractions of τ_1 (κ_1), τ_2 (κ_2) and long-lived plateau (δ) functions, and percent ligand-to-metal charge transfer (LMCT) for Cr_2O_n (n < 5) clusters.

Cluster	τ_2 (fs)	κ_1	κ_2	δ	LMCT
Cr_2	346 ± 43	0	0.724	0.276	0%
Cr_2O	620 ± 60	0.325	0.498	0.177	17%
Cr_2O_2	499 ± 28	0.560	0.344	0.095	31%
Cr_2O_3	413 ± 31	0.695	0.265	0.040	54%
Cr_2O_4	512 ± 48	0.838	0.162	0	63%

In metals, excess optically applied energy dissipates through e-e scattering within 10s of fs due to strong interactions between delocalized electrons. Limited excited state lifetime measurements have been reported for pure metal clusters, and range from ~20-200 fs,[157–159] comparable to the bulk values. In contrast, long lifetimes of electron-hole excitations are characteristic of semiconductors. Metal oxide clusters contain a larger splitting of the molecular orbitals (lower density of states), which decreases the number of unoccupied levels within the excitation energy, greatly reducing relaxation rates (longer lifetime). For example, the excited state lifetimes for $(TiO_2)_n$,[109] $(ZnO)^-_n$[160] and $(FeO)_n$[110] clusters depend strongly on both cluster size and charge carrier localization. The instantaneous O-2p to Cr-3d e-e scattering processes (κ_1 contribution) recorded in Cr_2O_n clusters increases with oxidation and suggests that they become more metallic with

increasing oxidation. This is a counterintuitive result until considering that the clusters are approaching the stoichiometry of the bulk half-metal, CrO_2.
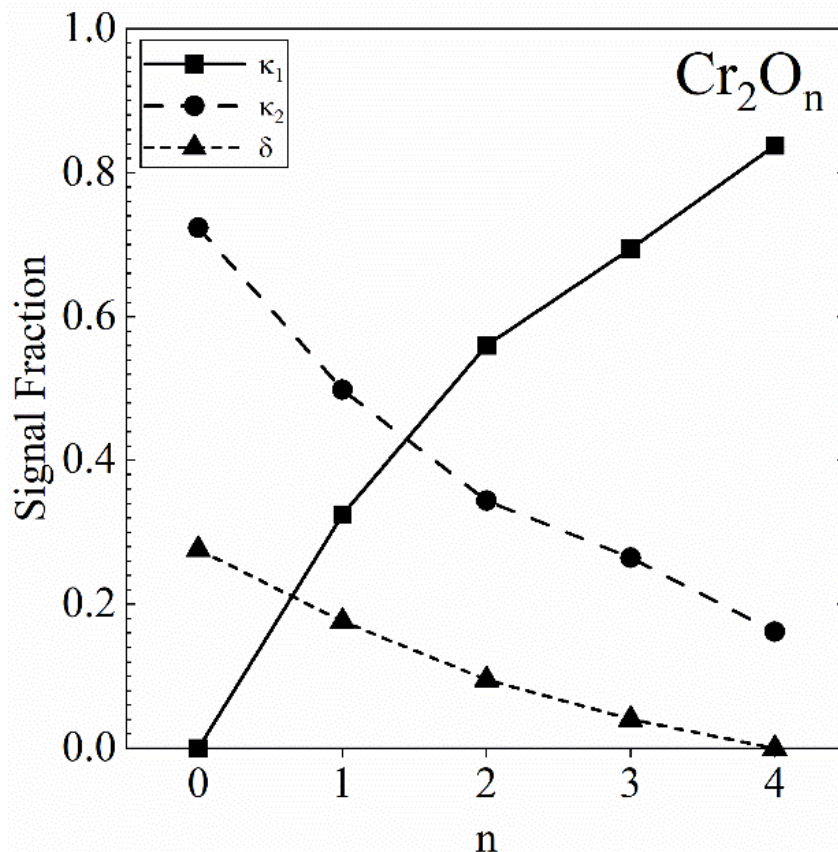
Figure 6.3: Plot of κ_1 (solid, squares), κ_2 (long dash, circles) and δ (short dash, triangles) of the neutral Cr_2O_n (n = 0-4) clusters

Insights on the relaxation dynamics are provided by changes in the theoretical electronic structure of clusters with oxidation.[162] In Cr_2O_n clusters, the first two O atoms bridge between the Cr atoms, and subsequent O atoms attach to the Cr atoms while maintaining a planar geometry, in agreement with previous calculations (Figure 6.2).[175,176,191] Electronic superexchange between Cr and O atoms in Cr_2O_n clusters (n = 1-4) makes them antiferromagnetically (AF) coupled, except for Cr_2O which is ferromagnetically (FM) coupled. Although the FM state of Cr_2O_3 has been suggested to

be degenerate,[174,175,181,191] the AF state is 0.5 eV in this study. Valence orbitals are Cr-3d dominated, with O-2p orbitals becoming important for high energy excitations or in clusters containing many O atoms. With increasing oxidation, the local magnetic moment on the Cr atoms steadily decreases from 5.1 μB in Cr_2O to 2.1 μB in Cr_2O_4, nearly matching the magnetic moment per Cr atom in bulk (~2.0 μB).[169,192]

Photoexcitation with a 3.1 eV pump photon shifts from d-d transitions between Cr atoms toward more LMCT character in Cr_2O_n clusters. As O atoms are included in the cluster, the Cr 3d-based spectral features diminish and the excited state shifts towards increasing involvement of O-2p orbitals with oxidation[177] as a result of charge transfer from Cr to O. The photoexcitation of Cr_2 is primarily a d-d transition in agreement with the transient signal that contains no κ_1 component and leads to an elongated bond. The excited state of Cr_2O contains up to 17% LMCT density and the transient signal contains 33% κ_1. The increased LMCT character (31%) of the photoexcited state in Cr_2O_2 matches the increased κ_1 (56%) of the total transient signal. Several excited states overlap around ~3.1 eV for Cr_2O_3, involving a maximum 54% LMCT character and increased experimental transient signal of 70% κ_1. Photoexcitation in Cr_2O_4 is up to 63% LMCT matching the largest κ_1 (84%) of the measured clusters and also contains no δ contribution. The LMCT projects an electron back onto the Cr-3d orbitals, inducing a rapid scattering on the few-fs timescale, similar to metallic excitations. In all cases, the bridging O act as electron donors, but the terminal O atoms act as both donors and acceptors. The electronic structures show a near-linear increase in the percent LMCT between O-2p and Cr-3d orbitals with oxidation (Figure 6.4), in excellent agreement to the increase in the measured κ_1 contribution.
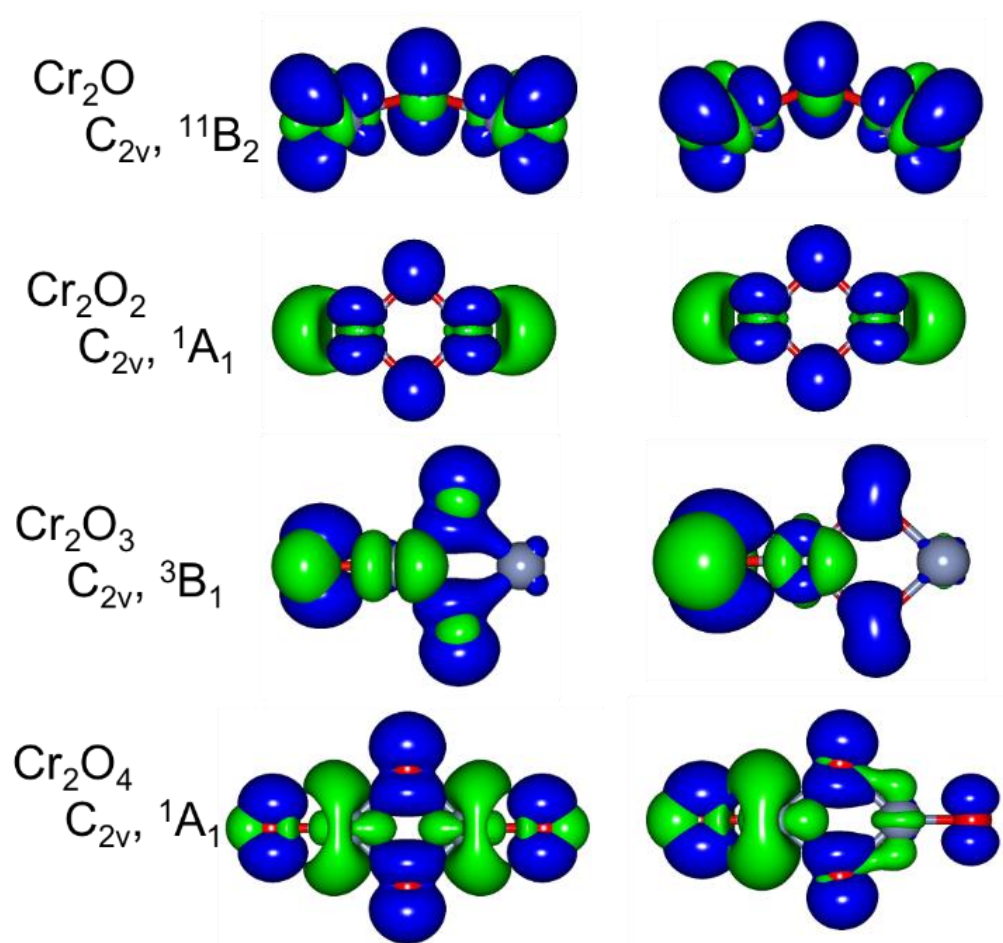
Figure 6.4: Charge carrier separation upon vertical excitation (left) and after adiabatic relaxation to the first excited state (right) for Cr_2O_n ($n < 5$) clusters. Electron density is shown in green and hole as blue.

Following vertical excitation, the clusters relax adiabatically, aligning with changes in their experimental transients. A linear decrease in δ with oxidation reveals that additional degrees of vibrational freedom improve each cluster's propensity to return to the ground state as vibrationally hot species. Although τ_2 is similar for all clusters, Cr_2O is ~20% longer (620 ± 60 fs), which may be related to FM coupling and an activated bending mode. In particular, terminal O atoms are well known to facilitate relaxation to the ground state through conical intersections,[155] and therefore reduces δ. The nuclear rearrangement for both Cr_2O_3 and Cr_2O_4 is primarily localized to the bending and

stretching motions of the terminal O atoms. Photoexcitation of Cr_2O_3 prepares a localized electron on the tri-coordinated Cr atom, while the other Cr is not involved due to the asymmetric O distribution in the cluster. Photoexcitation of Cr_2O_4 extends the bond length of one terminal O. Thus, Cr_2O_3 contains only 4% δ, while δ is absent from the transient signal of Cr_2O_4, revealing efficient recombination.

My results suggest that a fully oxidized Cr_2O_6 cluster that is void of d electrons will convert all photoexcited energy into vibrational energy within 10s of fs, similar to metallic systems. This inversed (counterintuitive) metallic behavior is explained by the transition from delocalized electronic states to strongly ionic LMCT upon oxidation, similar to the half-metal behavior of bulk CrO_2. Long-lived states are only present in chromium oxides that contain O vacancies, suggesting a single-crystalline bulk material may rapidly convert photonic excitation into heat within 10s of fs. The ultrafast dynamics reported herein show half-metal behavior at the molecular level. Such clusters can be formed over a range of compositions and stoichiometries, enabling a wide variation in magnetic behaviors and novel molecular spintronics materials.

6.2.3 Larger Chromium Oxide Series

The change in larger cluster series with oxidation is highlighted in the Cr_3O_n (Figure 6.5) and Cr_4O_n (Figure 6.7) cluster series. Although Cr_2O_4 only had two dangling O atoms, Cr_3O_6 forms a cyclic ring with three dangling O atoms. With the subtraction of O atoms from Cr_3O_6 the lifetime is not drastically affected until there are no dangling O atoms and higher symmetry in Cr_3O_3. The lifetime increases by almost 200 fs with less O content in Cr_3O_3 (770 ± 95 fs).
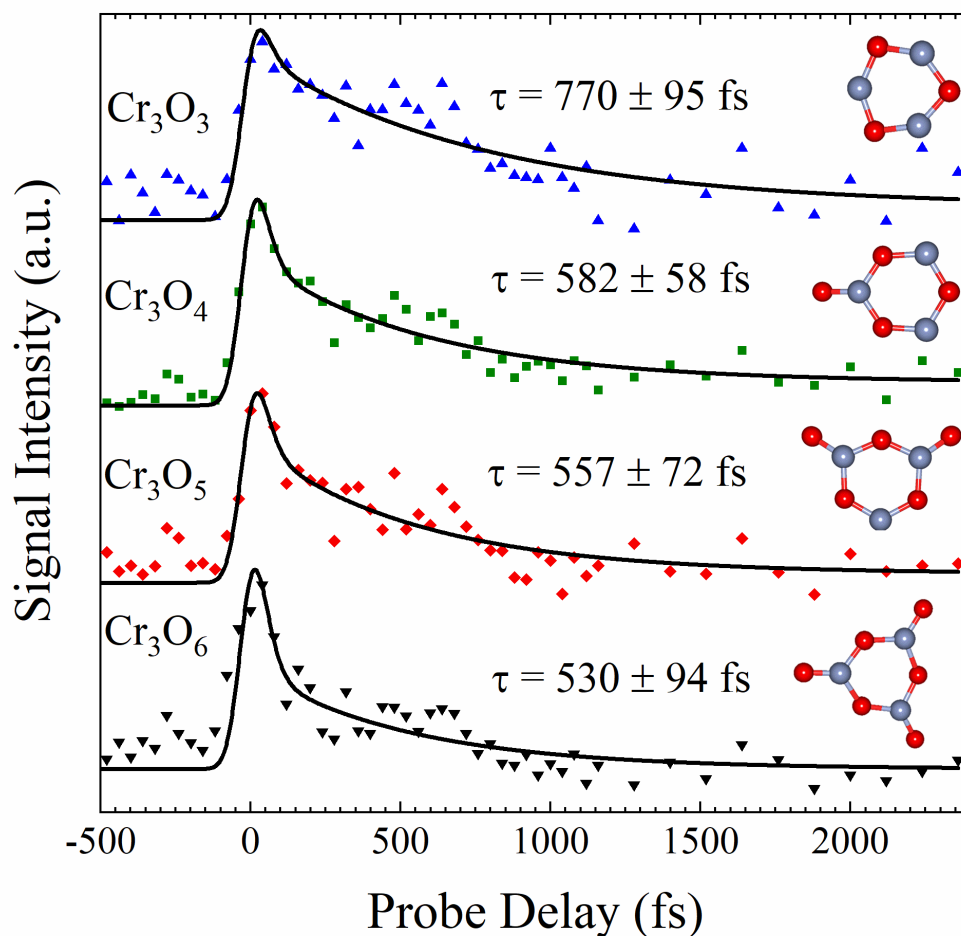
Figure 6.5: Cr_3O_n (n = 3-6) cluster series with cluster geometry and sub-ps lifetime shown above each fit.

The calculated structures of Cr_3O_n clusters are consistent with previous investigations,[182,193] forming a cyclic internal Cr_3O_3 ring of interchanging Cr-O bonds, and additional O binding externally to each Cr in planar structures. Cr_3O_n (n = 2-6) clusters increase in lifetime with decreased O character. Similar to Cr_2O_4 which is predominantly a LMCT from the O p-orbital to Cr d-orbitals,[162] Cr_3O_6 possesses a similar excited state transition and large contribution (83%) of the fast (35 fs) fitting component (Figure 6.6). Cr_3O_5 reduces in symmetry with only two dangling O atoms, resulting in a higher DoS below 3.5 eV and an excitation that has a lower MLCT character of Cr-d to

O-p transition. Cr_3O_4 has the largest average electron-hole delocalization following excitation (σ_{avg}), but shows a faster lifetime over $Cr_3O_{2,3}$ due. The sub-ps lifetimes are all roughly the same value, but the relative contribution of fast to sub-ps dynamics changes with the number of oxygen atoms. All sub-ps lifetimes, fast (30 fs) function contribution, average charge carrier delocalization (σ_{avg}) and calculated percent LMCT for each chromium cluster is shown in Table 6.2.
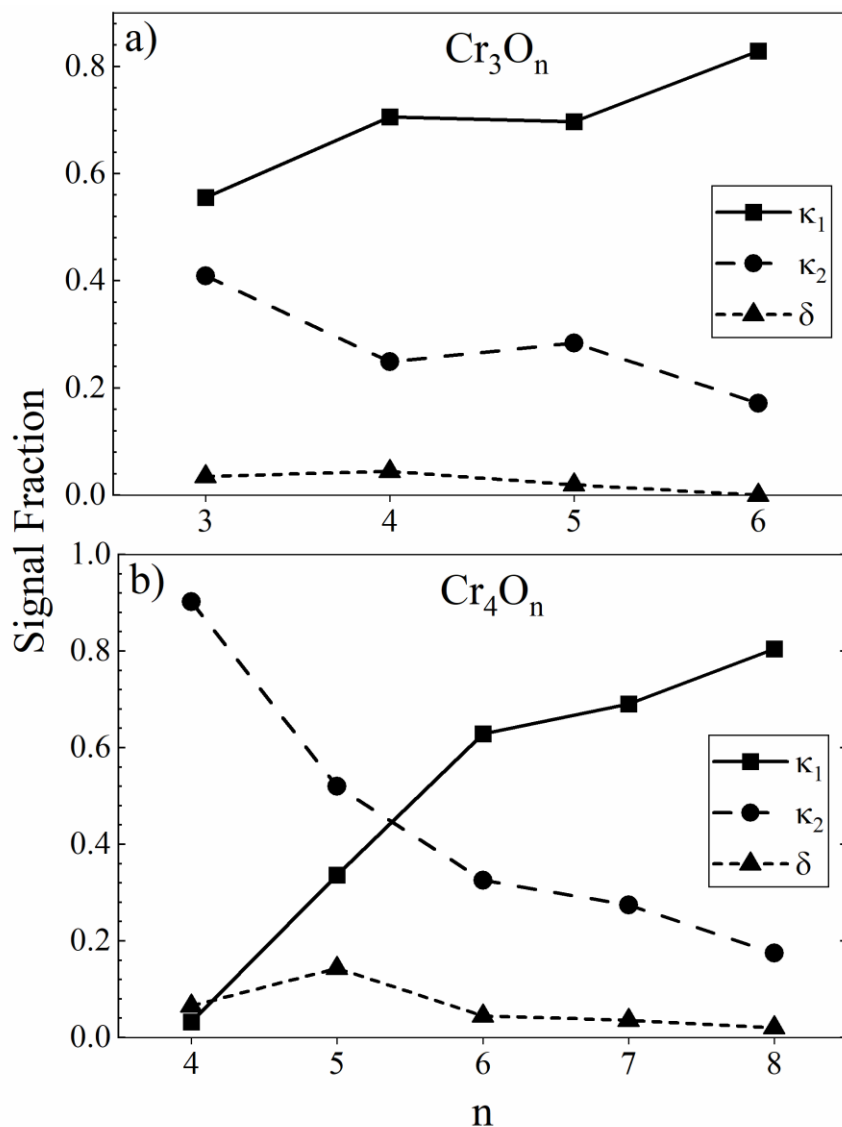
Figure 6.6: Fitting function ratio comparisons for a) Cr_3O_n (n = 3-6) and b) Cr_4O_n (n = 4-8) clusters.

Cr$_4$O$_4$ has a 3D structure void of dangling O atoms, consistent with previous results.[182] Cr$_4$O$_6$ remains compact but with additional bridging O atoms. Cr$_4$O$_7$ and Cr$_4$O$_8$ acquire one and two terminally bound O atoms, respectively, resulting in tetracoordinated Cr atoms. Transient signals of Cr$_4$O$_n$ (n = 4-8) clusters (Figure 6.7), akin to Cr$_3$O$_n$ clusters, have a decrease in the excited state lifetime with lower O content from the stoichiometric Cr$_4$O$_8$ cluster. Cr$_4$O$_7$ has the shortest lifetime in the Cr$_4$O$_n$ series of 458 $\pm$ 74 fs and has a larger contribution from τ_2 and plateau in the total signal over Cr$_4$O$_8$. The contribution of τ_2 and plateau function increases with decreased O content, with Cr$_4$O$_4$ showing the signal dominated by the τ_2 fitting function (90%) and long-lived plateau function (7%) (Figure 6.6).
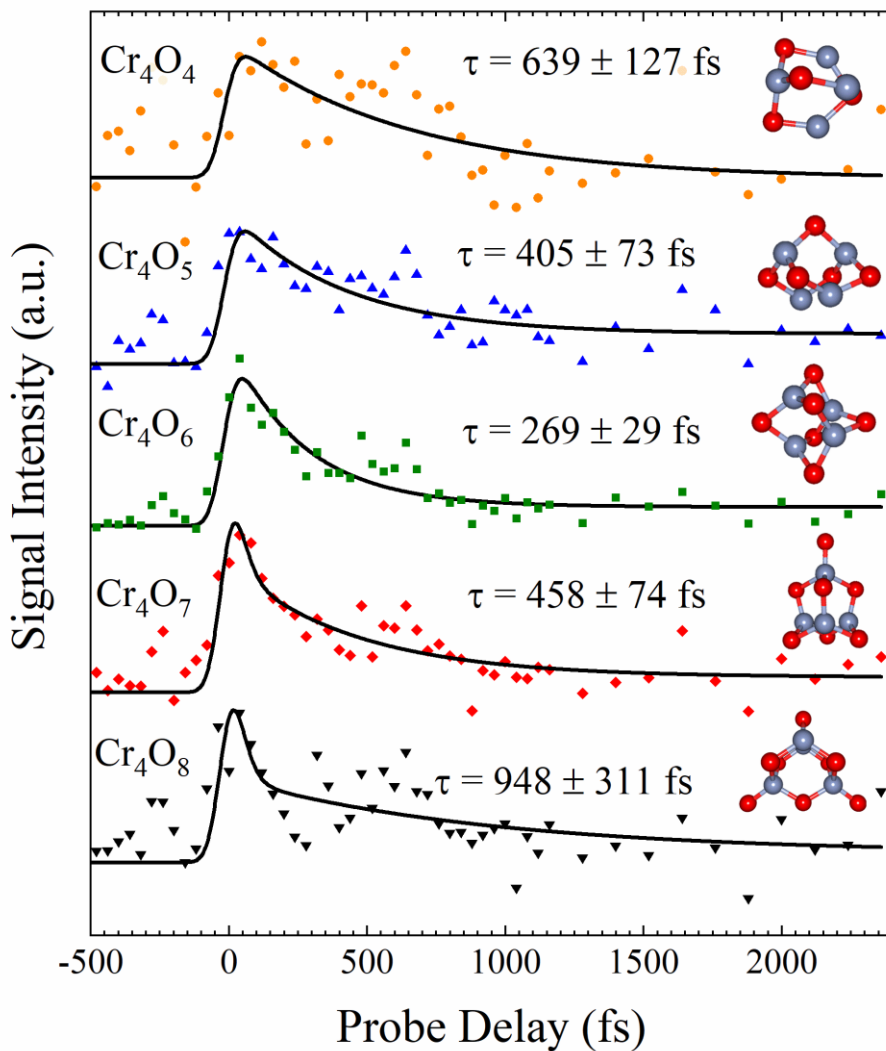
Figure 6.7: Cr_4O_{8-x} (x < 5) cluster transients with cluster geometry and sub-ps lifetime shown.

Cr_4O_8 has the longest lifetime of the series (948 ± 311 fs), due, in part, to a larger σ_{avg} (4.39). With one less O from Cr_4O_8, a dangling O is missing in Cr_4O_7, leading to a shorter relaxation lifetime due to a tighter bonding structure, resulting in a decreased σ_{avg} (3.66). Cr_4O_6 has a high symmetry without any terminal O atoms, resulting in a further decrease in σ_{avg} (3.46) and with a comparable lifetime to Cr_4O_7.

Table 6.2: Sub-ps lifetimes (τ_2), fast (30 fs) fitting function amplitude fraction (κ_1), average charge carrier delocalization (σ_{avg}) and percent LMCT for all neutral Cr_nO_{2n-x} ($n < 5$) cluster species.

Series	n	τ_2 (fs)	κ_1	σ_{avg}	LMCT (%)
	0	395 ± 25	0	-	0
CrO_n	1	373 ± 19	0.54	2.54	68
	2	333 ± 26	0.68	2.51	68
	0	346 ± 43	0	4.51	0
	1	620 ± 60	0.325	4.94	18
Cr_2O_n	2	499 ± 28	0.560	2.88	31
	3	413 ± 31	0.695	2.94	50
	4	512 ± 48	0.838	3.22	63
	3	775 ± 103	0.56	3.28	5
	4	582 ± 58	0.71	4.77	37
Cr_3O_n	5	557 ± 72	0.70	4.11	33
	6	530 94	0.83	4.24	46
	4	639 ± 127	0.03	4.10	5
	5	405 ± 73	0.34	3.76	6
Cr_4O_n	6	269 ± 29	0.59	3.46	11
	7	458 74	0.69	3.66	15
	8	948 311	0.80	4.39	30

Most excitations are a metal-to-metal transition in chromium oxide clusters. Smaller clusters with less O character have a decreased DoS, increased ferromagnetic coupling between Cr atoms, and therefore greater propensity to possess long-lived excited states. This is reflected in the measured increase in plateau function and τ_2 character with decreased O in Cr_4O_n ($n = 4$-8), Cr_3O_n ($n = 2$-6), and Cr_2O_n ($n = 0$-4) clusters.

This increasing metallic behavior of the chromium oxide clusters with oxygen content is counterintuitive and is explained as approaching the half-metal stoichiometry

and behavior of bulk CrO_2. Therefore, the half-metal behavior is shown at the molecular level and suggests that the wide variety of cluster geometries and structures will enable new molecular scale spintronic materials to be developed.

6.3 Conclusion

Time-resolved excitation experiments of neutral Cr_nO_{2n-x} ($n < 5$) clusters were performed and show that the relative contribution of three separate pathways changes almost linearly with oxidation at small cluster sizes. The involvement of the near instantaneous, or metallic relaxation component, is related to the theoretically determined electronic properties. The lifetimes show that LMCT excitations relax on an almost-instantaneous timescale and that d-d excitations relax on a sub-ps timescale. Significant long-lived excited states are only observed in suboxide systems, suggesting that carrier recombination is efficient only in closed systems. This simple picture of sequential oxidation reveals a trend in the excited state dynamics related to a shifting metallic behavior with O character.

As each cluster series decreases in O character, the clusters have similar structures but without externally bound O atoms. The change in structure and reduction in O causes a decrease in the DoS in each series, resulting in a larger propensity for the clusters to reach bound vibrational wells and is shown by the steady increase of τ_2 and plateau function in each series. Cr_2O_n ($n = 0$-4) clusters show minor changes in lifetime and linear changes to the fitting function contributions associated to structure, spin, percent LMCT and σ_{avg}. Similarly, Cr_3O_n ($n = 2$-6) and Cr_4O_n ($n = 4$-8) clusters have lifetimes associated to the structure, HL gap, percent LMCT and σ_{avg} with oxidation. The presence of dangling atoms results in a variance in the DoS, which ultimately changes the

electronic properties and reflects on the lifetimes of excited states in chromium oxide clusters. Loss of externally bound O atoms results in a smaller average charge carrier delocalization (σ_{avg}), with smaller HL gaps and σ_{avg} in suboxides facilitating faster relaxation. Excitations are primarily ligand-to-metal transitions in stoichiometric Cr_nO_{2n} (n = 2-4) chromium oxide clusters, affecting each clusters' propensity to have a long decay (τ_2) or long-lived (> 2 ps) plateau.

This experiment reports the first neutral cluster distribution, time-resolved excitation experiments of neutral small sized chromium oxide clusters, and electronic information on sub-nm $(CrO_2)_n$ clusters (n < 5) and their suboxides, aiding in the understanding of chromia excited state lifetimes following low energy photoexcitation. The information provided here will assist in the understanding of electronic transitions effects on excited state lifetimes in chromium oxides as they evolve to their bulk counterparts, inevitably leading to chromium materials of increased reactivity.

CHAPTER 7

CONCLUSIONS AND FUTURE DIRECTIONS

7.1 Occupied d-shell Effects on Cluster Dynamics

Neutral first-row transition metal oxide clusters of Ti, Cr, Fe and Ni were

produced using laser ablation and the femtosecond excited state dynamics were compared

using pump-probe spectroscopy in each system as a function of size and oxidation.

Experimental measurements coupled with theoretical calculations reveal that the

electronic properties and excited state relaxation dynamics of neutral transition metal

oxide clusters are influenced by cluster geometry, atomic composition, and the electron

contributions from O-2p and metal 3d-orbitals. Cr oxides indicate that the LMCT

character is directly related to metallic properties, with a linear increase in the

instantaneous metallic relaxation with a higher percent p-d excited state transition. $(NiO)_n$

clusters show that the large density of states facilitates internal vibrational relaxation

(IVR) through conical intersections, having minor changes to the relaxation dynamics

with O vacancies due to changes in the metal s- or d-orbital transition. $(FeO)_n$ clusters are

sensitive to oxidation and size, showing a high contribution of O-2p electrons at smaller

cluster sizes and increased IVR at larger cluster sizes, causing faster excited state

relaxation. $(TiO_2)_n$ clusters show an oscillating increase in the excited state lifetime with

size related to the cluster symmetry, which changes upon loss of O to form open-shelled

structures, dictating charge carrier delocalization.

It is concluded that cluster symmetry facilitated by O-2p electrons play an

important part in charge carrier dynamics in highly correlated first-row transition metal

oxide clusters. Higher average charge carrier delocalization, larger d-d electron transition

character, and lower density of states allows for longer excited state lifetimes. Additionally, the types of transitions and orbitals involved may be crucial in extending excited state lifetimes. Highly correlated materials have a high level of interactions between the metal and the ligand electronic orbitals. Although there are numerous explorations on the charge carrier dynamics of thin films and bulk materials, there is little known about the fundamental properties of these materials which dictate their reactivity. Inevitably, with slower excited state relaxation (longer lifetime), chemical, magnetic, and catalytic properties of materials may be enhanced due to the larger window of time to acquire desired transformations.

7.2 Future Directions

Measuring the excited state lifetimes of finite-sized atomic clusters is a blossoming field with innumerable applications. As laser pulses continue to decrease in their temporal profile, the mechanisms which dictate chemical reactions, and their fundamental properties will become resolved with higher clarity. The atomic changes to molecular structures, bulk lattices and interfacial layers remains a highly unexplored field. The study of cluster systems will assist in understanding charge carrier dynamics and the ability to modify materials to satisfy specific purposes, such as solar cell application, magnetic switching devices for memory storage, and catalysts.

This thesis focused on four of the ten first-row transition metal oxide systems, providing valuable insights towards the evolution of excited state dynamics as the first d-shell is filled. Although information was gained on the dependence of excited state lifetimes on charge carrier localization and the type of electronic transition, there are still missing details about the change in lifetimes, density of states, and accessible excited

states as the d-shell is filled. Therefore, extending this study to the excited state dynamics and atomic composition-dependent relaxation mechanisms of the remaining transition metal oxides of Sc, V, Mn, Co, Cu, and Zn through femtosecond pump-probe spectroscopy would be highly beneficial. Additionally, traversing down the periodic table to compare Cr to Mo or W (as an example) may provide interesting insights to further d-shell properties and their universal excited state nature (or lack thereof). The excited state dynamics of early d-shell transition metal oxides may behave very differently based upon the types of electronic transitions and contribution of s- p- and d-electrons. Therefore, similar experimental and theoretical studies may resolve any similarities or changes to excited state dynamics with atomic size.

Chemical reactivity is dictated by excited state lifetimes which survive long enough to induce change. The experiments outlined in this thesis resolved excited state lifetimes of several first-row transition metal oxides but did not directly observe any propensity to react with other materials. After the production of a transition metal oxide system, another gas-phase molecule may be easily introduced, such as NO_x, CO, CO_2, and other hydrocarbons to observe cluster reactivity. The change in signal intensity and formation of new ions following ionization may provide valuable information about composition-dependent reactivity, leading to further insights. Applying pump-probe spectroscopy may further resolve the timeframe of cluster reactivity with other gas-phase species as ions dissociate and form over hundreds of femtoseconds in time. Whether the atomic composition or photoexcitation lifetime is important may be elucidated through these experiments. This may be compared to the pure cluster excited state dynamics and

directly related to the applicability of atomically precise cluster reactivity towards bulk-scale materials.

The excited state lifetimes measured in this thesis are also specific to electronic transitions which occur at ~3.1 eV, showing several resonantly accessed excited states. However, numerous other allowed transitions occur at energies above and below this excitation energy and will provide changes to excited state lifetimes in each system dependent upon the excited state reached. Using pump photons of lower energy, for example, may show a faster relaxation dependent upon the electronic transition or percent LMCT character. Accessing excited states with higher precision of the supplied energy will afford increased insights towards the factors affecting excited state lifetimes of specific cluster compositions.

There is immeasurable work still to be done on the fundamental atomic changes from cluster to bulk-scale materials, the changes to the electronic properties as a result of single atomic additions or subtractions, the effects of orbital occupancy on excited state transitions, and the subsequent effects on the lifetimes which clusters become excited and relax back down to their energetic ground state. An insurmountable degree of experimental and theoretical investigations may build upon the results within this thesis. With a better understanding of the properties that effect excited state relaxation in highly correlated materials, the fundamental mechanisms which dictate reactivity may be further manipulated, ultimately leading to highly advanced materials.

.

BIBLIOGRAPHY

(1)   Knight, W. D.; Clemenger, K.; de Heer, W. A.; Saunders, W. A.; Chou, M. Y.; Cohen, M. L. Electronic Shell Structure and Abundances of Sodium Clusters. *Phys. Rev. Lett.* **1984**, *52*, 2141–2143.

(2)   Jena, P.; Castleman, A. W. Clusters: A Bridge across the Disciplines of Physics and Chemistry. *Proc. Natl. Acad. Sci.* **2006**, *103*, 10560–10569.

(3)   Henderson, M. A. A Surface Science Perspective on TiO_2 Photocatalysis. *Surf. Sci. Rep.* **2011**, *66*, 185–297.

(4)   Thompson, T. L.; Yates, J. T. Surface Science Studies of the Photoactivation of TiO_2-New Photochemical Processes. *Chem. Rev.* **2006**, *106*, 4428–4453.

(5)   Lang, S. M.; Bernhardt, T. M. Gas Phase Metal Cluster Model Systems for Heterogeneous Catalysis. *Physical Chemistry Chemical Physics*. **2012**, 9255–9269.

(6)   Luo, Z.; Castleman Jr., A. W.; Khanna, S. N. Reactivity of Metal Clusters. *Chem. Rev.* **2016**, *116*, 14456–14492.

(7)   Popok, V. N.; Campbell, E. E. B. Beams of Atomic Clusters: Effects on Impact with Solids. *Reviews on Advanced Materials Science*. **2006**, 19–45.

(8)   Bernstein, E. R. Neutral Cluster Mass Spectrometry. *Int. J. Mass Spectrom.* **2015**, *377*, 248–262.

(9)   Parida, P.; Kashikar, R.; Jena, A.; Nanda, B. R. K. Universality in the Electronic Structure of 3d Transition Metal Oxides. *J. Phys. Chem. Solids* **2018**, *123*, 133–149.

(10)   Zhang, X.; Shen, J. X.; Van de Walle, C. G. First-Principles Simulation of Carrier Recombination Mechanisms in Halide Perovskites. *Adv. Energy Mater.* **2020**, *10*, 1-20.

(11)   Sousa, C.; Tosoni, S.; Illas, F. Theoretical Approaches to Excited-State-Related Phenomena in Oxide Surfaces. *Chem. Rev.* **2013**, *113*, 4456–4495.

(12)   Zimmermann, R.; Steiner, P.; Claessen, R.; Reinert, F.; Hüfner, S. Electronic Structure Systematics of 3d Transition Metal Oxides. *J. Electron Spectros. Relat. Phenomena* **1998**, *96*, 179–186.

(13)   Von Issendorff, B.; Cheshnovsky, O. Metal to Insulator Transitions in Clusters. *Annu. Rev. Phys. Chem.* **2005**, *56*, 549–580.

(14)   Dong, P. T.; Cheng, J. X. Pump-Probe Microscopy: Theory, Instrumentation, and

Applications. *Spectrosc. (Santa Monica)* **2017**, *32*, 24–36.

(15) Zewail, A. H. Femtochemistry: Atomic-Scale Dynamics of the Chemical Bond. *J. Phys. Chem. A* **2000**, *104*, 5660–5694.

(16) Hecht, J. Short History of Laser Development. *Opt. Eng.* **2010**, *49*, 091002, 1-23.

(17) Silfvast, W. T. *Laser Fundamentals (2nd Edition)*, 2nd ed.; Cambridge University Press, **2004**.

(18) Duncan, M. A. Invited Review Article: Laser Vaporization Cluster Sources. *Review of Scientific Instruments*. **2012**, 41101, 1-19.

(19) Ledingham, K. W. D.; Singhal, R. P. High Intensity Laser Mass Spectrometry — a Review. *Int. J. Mass Spectrom. Ion Process.* **1997**, *163*, 149–168.

(20) Badani, P. M.; Das, S.; Sharma, P.; Vatsa, R. K. Photoionization of Atomic and Molecular Clusters Doped with Low Ionization Energy Molecules: Effect of Laser Wavelength, Intensity and Cluster Composition. *Int. J. Mass Spectrom.* **2013**, *348*, 53–58.

(21) Wolf, M. Femtosecond Dynamics of Electronic Excitations at Metal Surfaces. *Surf. Sci.* **1997**, *377–379*, 343–349.

(22) Micha, D. A.; Burghardt, I. Quantum Dynamics of Complex Molecular Systems: Preface. *Springer Series in Chemical Physics*. Springer US **2007**.

(23) Zhirnov, V. V.; Cavin, R. K. Basic Physics of ICT. In *Microsystems for Bioelectronics*; **2015**; 19–49.

(24) Frischkorn, C.; Wolf, M. Femtochemistry at Metal Surfaces: Nonadiabatic Reaction Dynamics. *Chem. Rev.* **2006**, *106*, 4207–4233.

(25) Aeschlimann, M.; Bauer, M.; Pawlik, S. Competing Nonradiative Channels for Hot Electron Induced Surface Photochemistry. *Chem. Phys.* **1996**, *205*, 127–141.

(26) Chen, C.; Tao, Z.; Carr, A.; Matyba, P.; Szilvási, T.; Emmerich, S.; Piecuch, M.; Keller, M.; Zusin, D.; Eich, S.; et al. Distinguishing Attosecond Electron–Electron Scattering and Screening in Transition Metals. *Proc. Natl. Acad. Sci.* **2017**, *114*, E5300–E5307.

(27) Wiley, W. C.; McLaren, I. H. Time-of-Flight Mass Spectrometer with Improved Resolution. *Rev. Sci. Instrum.* **1955**, *26*, 1150–1157.

(28) Pedersen, S.; Zewail, A. H. Femtosecond Real Time Probing of Reactions XXII Kinetic Description of Probe Absorption Fluorescence Depletion and Mass Spectrometry. *Mol. Phys.* **1996**, *89*, 1455–1502.

(29) Dermota, T. E.; Hydutsky, D. P.; Bianco, N. J.; Castleman, A. W. Excited-State Dynamics of $(SO_2)_m$ Clusters. *J. Phys. Chem. A* **2005**, *109*, 8259–8267.

(30) Dermota, T. E.; Hydutsky, D. P.; Bianco, N. J.; Castleman Jr., A. W. Photoinduced Ion-Pair Formation in the $(HI)_m (H_2O)_n$ Cluster System. *J. Chem. Phys.* **2005**, *123*.

(31) Reilly, N. M.; Reveles, J. U.; Johnson, G. E.; Del Campo, J. M.; Khanna, S. N.; Köster, A. M.; Castleman Jr., A. W. Experimental and Theoretical Study of the Structure and Reactivity of $Fe_mO_n^+$ (m = 1, 2; n = 1-5) with CO. *J. Phys. Chem. C* **2007**, *111*, 19086–19097.

(32) Reilly, N. M.; Reveles, J. U.; Johnson, G. E.; Khanna, S. N.; Castleman, A. W. Influence of Charge State on the Reaction of $FeO_3^{+/-}$ with Carbon Monoxide. *Chem. Phys. Lett.* **2007**, *435*, 295–300.

(33) Reilly, N. M.; Reveles, J. U.; Johnson, G. E.; Khanna, S. N.; Castleman, A. W. Experimental and Theoretical Study of the Structure and Reactivity of $Fe_{1-2}O_{\leq 6}^-$ Clusters with CO. *J. Phys. Chem. A* **2007**, *111*, 4158–4166.

(34) Schröder, D.; Schwarz, H.; Clemmer, D. E.; Chen, Y.; Armentrout, P. B.; Baranov, V. I.; Böhme, D. K. Activation of Hydrogen and Methane by Thermalized FeO^+ in the Gas Phase as Studied by Multiple Mass Spectrometric Techniques. *Int. J. Mass Spectrom. Ion Process.* **1997**, *161*, 175–191.

(35) Schröder, D.; Wesendrup, R.; Schalley, C. A.; Zummack, W.; Schwarz, H. Gas-Phase Reactions of Aliphatic Alcohols with 'Bare' FeO^+. *Helv. Chim. Acta* **1996**, *79*, 123–132.

(36) Oliveira, M. C.; Marçalo, J.; Vieira, M. C.; Ferreiraac, M. A. A. Formation of Some Transition Metal Oxide Cluster Anions and Reactivity towards Methanol in the Gas Phase. *Int. J. Mass Spectrom.* **1999**, *185*, 825–835.

(37) Yumura, T.; Amenomori, T.; Kagawa, Y.; Yoshizawa, K. Mechanism for the Formaldehyde to Formic Acid and the Formic Acid to Carbon Dioxide Conversions Mediated by an Iron-Oxo Species. *J. Phys. Chem. A* **2002**, *106*, 621–630.

(38) Xue, W.; Wang, Z. C.; He, S. G.; Xie, Y.; Bernstein, E. R. Experimental and Theoretical Study of the Reactions between Small Neutral Iron Oxide Clusters and Carbon Monoxide. *J. Am. Chem. Soc.* **2008**, *130*, 15879–15888.

(39) Xie, Y.; Dong, F.; Heinbuch, S.; Rocca, J. J.; Bernstein, E. R. Investigation of the Reactions of Small Neutral Iron Oxide Clusters with Methanol. *J. Chem. Phys.* **2009**, *130*, 114306–114311.

(40) Lv, S. Y.; Liu, Q. Y.; Chen, J. J.; He, S. G. Oxidation of Isoprene by Neutral Iron Oxide Nanoclusters in the Gas Phase. *J. Phys. Chem. C* **2019**, *123*, 25949–25956.

(41)   Yin, S.; Xue, W.; Ding, X. L.; Wang, W. G.; He, S. G.; Ge, M. F. Formation, Distribution, and Structures of Oxygen-Rich Iron and Cobalt Oxide Clusters. *Int. J. Mass Spectrom.* **2009**, *281*, 72–78.

(42)   Maunit, B.; Hachimi, A.; Manuelli, P.; Calba, P. J.; Muller, J. F. Formation of Iron Oxides Clusters Induced by Resonant Laser Ablation/Ionization. *Int. J. Mass Spectrom. Ion Process.* **1996**, *156*, 173–187.

(43)   Yan, B.; Li, L.; Yu, Q.; Hang, W.; He, J.; Huang, B. High Irradiance Laser Ionization Mass Spectrometry for Direct Speciation of Iron Oxides. *J. Am. Soc. Mass Spectrom.* **2010**, *21*, 1227–1234.

(44)   Sakurai, M.; Sumiyama, K.; Sun, Q.; Kawazoe, Y. Preferential Formation of $Fe_{13}O_8$ Clusters in a Reactive Laser Vaporization Cluster Source. *J. Phys. Soc. Japan.* **1999**, *68*, 3497–3499.

(45)   Shin, D. N.; Matsuda, Y.; Bernstein, E. R. On the Iron Oxide Neutral Cluster Distribution in the Gas Phase. II. Detection through 118 Nm Single Photon Ionization. *J. Chem. Phys.* **2004**, *120*, 4157–4164.

(46)   Shin, D. N.; Matsuda, Y.; Bernstein, E. R. On the Iron Oxide Neutral Cluster Distribution in the Gas Phase. I. Detection through 193 Nm Multiphoton Ionization. *J. Chem. Phys.* **2004**, *120*, 4150–4156.

(47)   Jones, N. O.; Reddy, B. V.; Rasouli, F.; Khanna, S. N. Structural Growth in Iron Oxide Clusters: Rings, Towers, and Hollow Drums. *Phys. Rev. B - Condens. Matter Mater. Phys.* **2005**, *72*, 165411–165414.

(48)   Ju, M.; Lv, J.; Kuang, X.-Y.; Ding, L.-P.; Lu, C.; Wang, J.-J.; Jin, Y.-Y.; Maroulis, G. Systematic Theoretical Investigation of Geometries, Stabilities and Magnetic Properties of Iron Oxide Clusters $(FeO)_n^\mu$ ($n = 1$–8, $\mu = 0, \pm 1$): Insights and Perspectives. *RSC Adv.* **2015**, *5*, 6560–6570.

(49)   Erlebach, A.; Hühn, C.; Jana, R.; Sierka, M. Structure and Magnetic Properties of $(Fe_2O_3)_n$ Clusters ($n = 1$–5). **2014**, *16*, 26421–26426.

(50)   Gutsev, G. L.; Belay, K. G.; Bozhenko, K. V.; Gutsev, L. G.; Ramachandran, B. R. A Comparative Study of Small 3d-Metal Oxide $(FeO)_n$, $(CoO)_n$, and $(NiO)_n$ Clusters. *Phys. Chem. Chem. Phys.* **2016**, *18*, 27858–27867.

(51)   Ohshimo, K.; Komukai, T.; Moriyama, R.; Misaizu, F. Isomer Separation of Iron Oxide Cluster Cations by Ion Mobility Mass Spectrometry. *J. Phys. Chem. A* **2014**, *118*, 3899–3905.

(52)   Chertihin, G. V.; Saffel, W.; Yustein, J. T.; Andrews, L.; Neurock, M.; Ricca, A.; Bauschlicher, C. W. Reactions of Laser-Ablated Iron Atoms with Oxygen Molecules in Condensing Argon. Infrared Spectra and Density Functional

Calculations of Iron Oxide Product Molecules. *J. Phys. Chem.* **1996**, *100*, 5261–5273.

(53) Andrews, L.; Chertihin, G. V.; Ricca, A.; Bauschlicher, C. W. Reactions of Laser-Ablated Iron Atoms with Oxygen Molecules: Matrix Infrared Spectra and Density Functional Calculations of OFeO, FeOO, and Fe(O$_2$). *J. Am. Chem. Soc.* **1996**, *118*, 467–470.

(54) Kirilyuk, A.; Fielicke, A.; Demyk, K.; Von Helden, G.; Meijer, G.; Rasing, T. Ferrimagnetic Cagelike Fe$_4$O$_6$ Cluster: Structure Determination from Infrared Dissociation Spectroscopy. *Phys. Rev. B - Condens. Matter Mater. Phys.* **2010**, *82*, 10–13.

(55) Krauss, M.; Stevens, W. J. Electronic Structure of FeO and RuO. *J. Chem. Phys.* **1985**, *82*, 5584–5596.

(56) Sakellaris, C. N.; Miliordos, E.; Mavridis, A. First Principles Study of the Ground and Excited States of FeO, FeO$^+$, and FeO$^-$. *J. Chem. Phys.* **2011**, *134*, 234308.

(57) Hendrickx, M. F. A.; Anam, K. R. A New Proposal for the Ground State of the FeO$^-$ Cluster in the Gas Phase and for the Assignment of Its Photoelectron Spectra. *J. Phys. Chem. A* **2009**, *113*, 8746–8753.

(58) Chestakov, D. A.; Parker, D. H.; Baklanov, A. V. Iron Monoxide Photodissociation. *J. Chem. Phys.* **2005**, *122*, 1–4.

(59) Fan, J.; Wang, L. Photoelectron Spectroscopy of FeO$^-$ and FeO$_2^-$: Observation of Low-spin Excited States of FeO and Determination of the Electron Affinity of FeO$_2$. *J. Chem. Phys.* **1995**, *102*, 8714–8717.

(60) Engelking, P. C.; Lineberger, W. C. Laser Photoelectron Spectrometry of FeO$^-$: Electron Affinity, Electronic State Separations, and Ground State Vibrations of Iron Oxide, and a New Ground State Assignment. *J. Chem. Phys.* **1977**, *66*, 5054–5058.

(61) Gutsev, G. L.; Bauschlicher, C. W.; Zhai, H. J.; Wang, L. S. Structural and Electronic Properties of Iron Monoxide Clusters Fe$_n$O and Fe$_n$O$^-$ (n=2-6): A Combined Photoelectron Spectroscopy and Density Functional Theory Study. *J. Chem. Phys.* **2003**, *119*, 11135–11145.

(62) Wang, L. S.; Wu, H.; Desai, S. R. Sequential Oxygen Atom Chemisorption on Surfaces of Small Iron Clusters. *Phys. Rev. Lett.* **1996**, *76*, 4853–4856.

(63) Wu, H.; Desai, S. R.; Wang, L. S. Observation and Photoelectron Spectroscopic Study of Novel Mono- and Diiron Oxide Molecules: FeO$_y^-$ (y = 1-4) and Fe$_2$O$_y^-$ (y = 1-5). *J. Am. Chem. Soc.* **1996**, *118*, 5296–5301.

(64) Velegrakis, M.; Mihesan, C.; Jadraque, M. Collision-Induced Dissociation Studies on $Fe(O_2)_n^+$ (n = 1-6) Clusters: Application of a New Technique Based on Crossed Molecular Beams. *J. Phys. Chem. A* **2013**, *117*, 2891–2898.

(65) Armentrout, P. Reactoins and Thermochemistry of Small Transition Metal Cluster Ions. *Annu. Rev. Phys. chem.* **2001**, *52*, 423–461.

(66) Schröder, D.; Jackson, P.; Schwarz, H. Dissociation Patterns of Small $Fe_mO_n^+$ (m=1-4, n<6) Cluster Cations Formed Upon Chemical Ionization of $Fe(CO)_5/O_2$ Mixtures. *Eur. J. Inorg. Chem* **2000**, *2000*, 1171–1175.

(67) Li, M.; Liu, S. R.; Armentrout, P. B. Collision-Induced Dissociation Studies of $Fe_mO_n^+$: Bond Energies in Small Iron Oxide Cluster Cations, $Fe_mO_n^+$ (m=1-3, n=1-6). *J. Chem. Phys.* **2009**, *131*, 144310–144316.

(68) Koyama, K.; Kudoh, S.; Miyajima, K.; Mafuné, F. Dissociation Energy for O_2 Release from Gas-Phase Iron Oxide Clusters Measured by Temperature-Programmed Desorption Experiments. *Chem. Phys. Lett.* **2015**, *625*, 104–109.

(69) Molek, K. S.; Anfuso-Cleary, C.; Duncan, M. A. Photodissociation of Iron Oxide Cluster Cations. *J. Phys. Chem. A* **2008**, *112*, 9238–9247.

(70) Gutsev, G. L.; Belay, K. G.; Gutsev, L. G.; Ramachandran, B. R. Geometrical and Magnetic Structure of Iron Oxide Clusters $(FeO)_n$ for n > 10. *Comput. Mater. Sci.* **2017**, *137*, 134–143.

(71) Metz, R. B.; Nicolas, C.; Ahmed, M.; Leone, S. R. Direct Determination of the Ionization Energies of FeO and CuO with VUV Radiation. *J. Chem. Phys.* **2005**, *123*, 114313.

(72) Nieman, G. C.; Parks, E. K.; Richtsmeier, S. C.; Liu, K.; Pobo, L. G.; Riley, S. J. Multiphoton Ionization and Fragmentation of Transition-Metal Cluster Oxides. *High Temp. Sci.* **1986**, *22*, 115.

(73) Hildenbrand, D. L. Thermochemistry of Molecular FeO, FeO^+ and FeO. *Chem. Phys. Lett.* **1975**, *34*, 352–354.

(74) Gutsev, G. L.; Belay, K. G.; Gutsev, L. G.; Ramachandran, B. R. Structure and Properties of Iron Oxide Clusters: From Fe_6 to Fe_6O_{20} and from Fe_7 to Fe_7O_{24}. *J. Comput. Chem.* **2016**, *37*, 2527–2536.

(75) Huber, L.; Ferrer, A.; Kubacka, T.; Huber, T.; Dornes, C.; Sato, T.; Ogawa, K.; Tono, K.; Katayama, T.; Inubushi, Y.; et al. Coherent Acoustic Perturbation of Second-Harmonic Generation in NiO. *Phys. Rev. B - Condens. Matter Mater. Phys.* **2015**, *92*, 94304.

(76) Fiebig, M.; Duong, N. P.; Satoh, T.; Van Aken, B. B.; Miyano, K.; Tomioka, Y.;

Tokura, Y. Ultrafast Magnetization Dynamics of Antiferromagnetic Compounds. *J. Phys. D. Appl. Phys.* **2008**, *41*, 164005.

(77) Fiebig, M.; Duong, N. P.; Satoh, T.; Lottermoser, T. Ultrafast and Magnetoelectric Phase Transitions in Antiferromagnets. *J. Magn. Magn. Mater.* **2006**, *300*, e264–e269.

(78) Gillmeister, K.; Golež, D.; Chiang, C. T.; Bittner, N.; Pavlyukh, Y.; Berakdar, J.; Werner, P.; Widdra, W. Ultrafast Coupled Charge and Spin Dynamics in Strongly Correlated NiO. *Nat. Commun.* **2020**, *11*, 1-9.

(79) Gómez-Abal, R.; Ney, O.; Satitkovitchai, K.; Hübner, W. All-Optical Subpicosecond Magnetic Switching in NiO(001). *Phys. Rev. Lett.* **2004**, *92*, 1-4.

(80) Tancogne-Dejean, N.; Sentef, M. A.; Rubio, A. Ultrafast Transient Absorption Spectroscopy of the Charge-Transfer Insulator NiO: Beyond the Dynamical Franz-Keldysh Effect. *Phys. Rev. B.* **2020**, *102*, 115106.

(81) Corani, A.; Li, M. H.; Shen, P. S.; Chen, P.; Guo, T. F.; El Nahhas, A.; Zheng, K.; Yartsev, A.; Sundström, V.; Ponseca, C. S. Ultrafast Dynamics of Hole Injection and Recombination in Organometal Halide Perovskite Using Nickel Oxide as P-Type Contact Electrode. *J. Phys. Chem. Lett.* **2016**, *7*, 1096–1101.

(82) Dillon, R. J.; Alibabaei, L.; Meyer, T. J.; Papanikolas, J. M. Enabling Efficient Creation of Long-Lived Charge-Separation on Dye-Sensitized NiO Photocathodes. *ACS Appl. Mater. Interfaces.* **2017**, *9*, 26786–26796.

(83) Dhital, B.; Rao, V. G.; Lu, H. P. Probing Single-Molecule Electron-Hole Transfer Dynamics at a Molecule-NiO Semiconductor Nanocrystalline Interface. *Phys. Chem. Chem. Phys.* **2017**, *19*, 17216–17223.

(84) Brown, A. M.; Antila, L. J.; Mirmohades, M.; Pullen, S.; Ott, S.; Hammarström, L. Ultrafast Electron Transfer between Dye and Catalyst on a Mesoporous NiO Surface. *J. Am. Chem. Soc.* **2016**, *138*, 8060–8063.

(85) Biswas, S.; Husek, J.; Londo, S.; Baker, L. R. Ultrafast Electron Trapping and Defect-Mediated Recombination in NiO Probed by Femtosecond Extreme Ultraviolet Reflection-Absorption Spectroscopy. *J. Phys. Chem. Lett.* **2018**, *9*, 5047–5054.

(86) Gao, Y.; Sun, Q.; Yu, J. M.; Motta, M.; McClain, J.; White, A. F.; Minnich, A. J.; Chan, G. K. L. Electronic Structure of Bulk Manganese Oxide and Nickel Oxide from Coupled Cluster Theory. *Phys. Rev. B.* **2020**, *101*, 1–9.

(87) Friedman-Hill, E. J.; Field, R. W. Analysis of the $[16.0]^3\Sigma^-$-$X^3\Sigma^-$ and $[16.0]^3\Sigma^-$-$[4.3]^3\Pi_i$ Band Systems of the NiO Molecule. *J. Mol. Spectrosc.* **1992**, *155*, 259–276.

(88) Alidoust, N.; Toroker, M. C.; Carter, E. A. Revisiting Photoemission and Inverse Photoemission Spectra of Nickel Oxide from First Principles: Implications for Solar Energy Conversion. *J. Phys. Chem. B.* **2014**, *118*, 7963–7971.

(89) Li, J. L.; Rignanese, G. M.; Louie, S. G. Quasiparticle Energy Bands of NiO in the GW Approximation. *Phys. Rev. B - Condens. Matter Mater. Phys.* **2005**, *71*, 1–4.

(90) Dibble, C. J.; Akin, S. T.; Ard, S.; Fowler, C. P.; Duncan, M. A. Photodissociation of Cobalt and Nickel Oxide Cluster Cations. *J. Phys. Chem. A.* **2012**, *116*, 5398–5404.

(91) Aguilera-Del-Toro, R. H.; Aguilera-Granja, F.; Balbás, L. C.; Vega, A. Structure, Fragmentation Patterns, and Magnetic Properties of Small Nickel Oxide Clusters. *Phys. Chem. Chem. Phys.* **2017**, *19*, 3366–3383.

(92) Walch, S. P.; W.A., G. I. Electronic States of the NiO Molecule. *J. Am. Chem. Soc.* **1978**, *100*, 1338–1348.

(93) Wu, H.; Wang, L. S. A Study of Nickel Monoxide (NiO), Nickel Dioxide (ONiO), and $Ni(O_2)$ Complex by Anion Photoelectron Spectroscopy. *J. Chem. Phys.* **1997**, *107*, 16–21.

(94) Tjernberg, O.; Chiaia, G.; Karlsson, U. O.; De Groot, F. M. F. Resonant Photoelectron Spectroscopy on CoO. *J. Phys. Condens. Matter* **1997**, *9*, 9863–9871.

(95) Ho, J.; Polak, M. L.; Ervin, K. M.; Lineberger, W. C. Photoelectron Spectroscopy of Nickel Group Dimers: Ni^-_2, Pd^-_2, and Pt^-_2. *J. Chem. Phys.* **1993**, *99*, 8542–8551.

(96) Ramond, T. M. M.; Davico, G. E. E.; Hellberg, F.; Svedberg, F.; Salén, P.; Söderqvist, P.; Lineberger, W. C. C. Photoelectron Spectroscopy of Nickel, Palladium, and Platinum Oxide Anions. *J. Mol. Spectrosc.* **2002**, *216*, 1–14.

(97) Qin, C.; Zang, J.; Zhang, D.; Zhang, Q.; Chen, Y. Laser-induced Fluorescence Spectroscopy of NiO between 510 and 650 Nm. *Chinese J. Chem. Phys.* **2013**, *26*, 512–518.

(98) Vardhan, D.; Liyanage, R.; Armentrout, P. B. Guided Ion Beam Studies of the Reactions of Ni_n^+ (n=2-18) with O_2: Nickel Cluster Oxide and Dioxide Bond Energies. *J. Chem. Phys.* **2003**, *119*, 4166–4178.

(99) Gutsev, G. L.; Bauschlicher, C. W. Chemical Bonding, Electron Affinity, and Ionization Energies of the Homonuclear 3d Metal Dimers. *J. Phys. Chem. A* **2003**, *107*, 4755–4767.

(100) Ahmed, F.; Nixon, E. R. The A→X System of Ni_2 in Argon Matrices. *The Journal of Chemical Physics.* **1979**, 3547–3549.

(101) Moskovits, M.; Hulse, J. E. The Ultraviolet–Visible Spectra of Diatomic, Triatomic, and Higher Nickel Clusters. *J. Chem. Phys.* **1977**, *66*, 3988–3994.

(102) Wang, H.; Haouari, H.; Craig, R.; Lombardi, J. R.; Lindsay, D. M. Raman Spectra of Mass-Selected Nickel Dimers in Argon Matrices. *J. Chem. Phys.* **1996**, *104*, 3420–3422.

(103) Anderson, A. B. Theory of Ultraviolet Spectra for Ni_2 and Ni_3 and Hypothesis for Argon Matrix Frequency Shifts for Ni Atoms. *J. Chem. Phys.* **1977**, *66*, 5108–5111.

(104) Goel, S.; Masunov, A. E. Density Functional Theory Study of Small Nickel Clusters. *J. Mol. Model.* **2012**, *18*, 783–790.

(105) López-Estrada, O.; Orgaz, E. Transition States, Electronic Structure, and Magnetic Properties of Small-Sized Nickel Clusters. *Phys. Rev. B - Condens. Matter Mater. Phys.* **2015**, *91*, 75428.

(106) Bandyopadhyay, D. Chemisorptions Effect of Oxygen on the Geometries, Electronic and Magnetic Properties of Small Size Ni_n (n = 1-6) Clusters. *J. Mol. Model.* **2012**, *18*, 737–749.

(107) Pakiari, A. H.; Pahlavan, F. The Electronic Structures of Small Ni_n (n = 2-4) Clusters and Their Interactions with Ethylene and Triplet Oxygen: A Theoretical Study. **2014**, *15*, 4055–4066.

(108) Reddy, B. V; Nayak, S. K.; Khanna, S. N.; Rao, B. K.; Jena, P. Physics of Nickel Clusters. 2. Electronic Structure and Magnetic Properties. *J. Phys. Chem. A* **1998**, *102*, 1748–1759.

(109) Garcia, J. M.; Heald, L. F.; Shaffer, R. E.; Sayres, S. G. Oscillation in Excited State Lifetimes with Size of Sub-Nanometer Neutral $(TiO_2)_n$ Clusters Observed with Ultrafast Pump–Probe Spectroscopy. *J. Phys. Chem. Lett.* **2021**, *12*, 4098–4103.

(110) Garcia, J. M.; Shaffer, R. E.; Sayres, S. G. Ultrafast Pump-Probe Spectroscopy of Neutral Fe_nO_m Clusters (n, m < 16). *Phys. Chem. Chem. Phys.* **2020**, *22*, 24624–24632.

(111) Xu, H. G.; Li, X. N.; Kong, X. Y.; He, S. G.; Zheng, W. J. Interaction of TiO^+ with Water: Infrared Photodissociation Spectroscopy and Density Functional Calculations. *Phys. Chem. Chem. Phys.* **2013**, *15*, 17126–17133.

(112) Çakir, D.; Gülseren, O. Ab Initio Study of Neutral $(TiO_2)_n$ Clusters and Their Interactions with Water and Transition Metal Atoms. *J. Phys. Condens. Matter* **2012**, *24*, 305301.

(113) Oprea, C. I.; Gîrt, M. A. Structure and Electronic Properties of TiO₂ Nanoclusters and Dye-Nanocluster Systems Appropriate to Model Hybrid Photovoltaic or Photocatalytic Applications. *Nanomaterials*. **2019**, *9*, 357, 1-31.

(114) Chou, T. P.; Zhang, Q.; Russo, B.; Fryxell, G. E.; Cao, G. Titania Particle Size Effect on the Overall Performance of Dye-Sensitized Solar Cells. *J. Phys. Chem. C.* **2007**, *111*, 6296–6302.

(115) Siwi Nska-Stefa Nska, K.; Nowacka, M.; Ko1odziejczak-Radzimska, A.; Jesionowski, T. Preparation of Hybrid Pigments via Adsorption of Selected Food Dyes onto Inorganic Oxides Based on Anatase Titanium Dioxide. *Dyes and Pigments.* **2012**, 94, 338-348.

(116) Muraca, A. R.; Kershis, M. D.; Camillone, N.; White, M. G. Ultrafast Dynamics of Acetone Photooxidation on TiO₂(110). *J. Chem. Phys.* **2019**, *151*, 161103.

(117) Fernandes Fraceto, L.; Espirito Santo Pereira, A.; Lischka Sampaio Mayer, J.; Rastogi, A.; Brestic, M.; Zivcak, M.; Sytar, O.; Kalaji, H. M.; He, X.; Mbarki, S. Impact of Metal and Metal Oxide Nanoparticles on Plant: A Critical Review. *Impact Met. Met. Oxide Nanoparticles Plant A Crit. Rev. Front. Chem* **2017**, *5*, 78.

(118) Richter, C.; Schmuttenmaer, C. A. Exciton-like Trap States Limit Electron Mobility in TiO₂ Nanotubes. *Nat. Nanotechnol.* **2010**, *5*, 769–772.

(119) Shingai, D.; Ide, Y.; Sohn, W. Y.; Katayama, K. Photoexcited Charge Carrier Dynamics of Interconnected TiO2 Nanoparticles: Evidence of Enhancement of Charge Separation at Anatase-Rutile Particle Interfaces. *Phys. Chem. Chem. Phys.* **2018**, *20*, 3484–3489.

(120) Li, L.; Li, W.; Ji, A.; Wang, Z.; Zhu, C.; Zhang, L.; Yang, J.; Mao, L. F. Interaction of Oxygen Vacancy and Its Impact on Transmission Coefficient in Oxygen-Deficient Titanium Dioxide: Ab Initio Calculations. *Phys. Status Solidi Basic Res.* **2015**, *252*, 2735–2744.

(121) Du, H.; Jia, Y.; Niu, C.; Hu, K.; Li, H.; Yu, L. The Ratio Law of the Structure Evolution and Stability for Ti_nO_m (n = 3–18, m = 1–2n) Clusters. *Chem. Phys. Lett.* **2019**, *731*, 136574.

(122) Xu, B.; Sohn, H. Y.; Mohassab, Y.; Lan, Y. Structures, Preparation and Applications of Titanium Suboxides. *RSC Advances*. **2016**, 79706–79722.

(123) Nagao, M.; Misu, S.; Hirayama, J.; Otomo, R.; Kamiya, Y. Magneli-Phase Titanium Suboxide Nanocrystals as Highly Active Catalysts for Selective Acetalization of Furfural. *ACS Appl. Mater. Interfaces* **2020**, *12*, 2539–2547.

(124) Wang, Y.; Qin, Y.; Li, G.; Cui, Z.; Zhang, Z. One-Step Synthesis and Optical Properties of Blue Titanium Suboxide Nanoparticles. *J. Cryst. Growth.* **2005**, *282*,

402–406.

(125) Jemec Kokalj, A.; Novak, S.; Talaber, I.; Kononenko, V.; Bizjak Mali, L.; Vodovnik, M.; Žegura, B.; Eleršek, T.; Kalčikova, G.; Žgajnar Gotvajn, A.; et al. The First Comprehensive Safety Study of Magnéli Phase Titanium Suboxides Reveals No Acute Environmental Hazard. *Environ. Sci. Nano* **2019**, *6*, 1131–1139.

(126) Lee, J. H.; Cho, S.; Roy, A.; Jung, H. T.; Heeger, A. J. Enhanced Diode Characteristics of Organic Solar Cells Using Titanium Suboxide Electron Transport Layer. *Appl. Phys. Lett.* **2010**, *96*, 163303.

(127) Pei, X.; Zhang, T.; Zhong, J.; Chen, Z.; Jiang, C.; Chen, W. Substoichiometric Titanium Oxide Ti_2O_3 Exhibits Greater Efficiency in Enhancing Hydrolysis of 1,1,2,2-Tetrachloroethane than TiO_2 Nanomaterials. *Sci. Total Environ.* **2021**, *774*, 145705, 1-8.

(128) Yu, M.; Saunders, T.; Grasso, S.; Mahajan, A.; Zhang, H.; Reece, M. J. Magnéli Phase Titanium Suboxides by Flash Spark Plasma Sintering. *Scr. Mater.* **2018**, *146*, 241–245.

(129) Bell, C. N.; Lee, D. C.; Drexler, M. N.; Rouleau, C. M.; Sasaki, K.; Senanayake, S. D.; Williams, M. D.; Alamgir, F. M. Substoichiometric Tuning of the Electronic Properties of Titania. *Thin Solid Films.* **2021**, *717*, 138437.

(130) Weichman, M. L.; Debnath, S.; Kelly, J. T.; Gewinner, S.; Schöllkopf, W.; Neumark, D. M.; Asmis, K. R. Dissociative Water Adsorption on Gas-Phase Titanium Dioxide Cluster Anions Probed with Infrared Photodissociation Spectroscopy. *Top. Catal.* **2018**, *61*, 92–105.

(131) Luttrell, T.; Halpegamage, S.; Tao, J.; Kramer, A.; Sutter, E.; Batzill, M. Why Is Anatase a Better Photocatalyst than Rutile? - Model Studies on Epitaxial TiO_2 Films. *Sci. Rep.* **2015**, *4*, 1–8.

(132) Maity, P.; Mohammed, O. F.; Katsiev, K.; Idriss, H. Study of the Bulk Charge Carrier Dynamics in Anatase and Rutile TiO_2 Single Crystals by Femtosecond Time-Resolved Spectroscopy. *J. Phys. Chem. C.* **2018**, *122*, 8925–8932.

(133) Elmaslmane, A. R.; Watkins, M. B.; McKenna, K. P. First-Principles Modeling of Polaron Formation in TiO_2 Polymorphs. *J. Chem. Theory Comput.* **2018**, *14*, 3740–3751.

(134) Monticone, S.; Tufeu, R.; Kanaev, A. V.; Scolan, E.; Sanchez, C. Quantum Size Effect in TiO2 Nanoparticles: Does It Exist? *Appl. Surf. Sci.* **2000**, *162–163*, 565–570.

(135) Serpone, N.; Lawless, D.; Khairutdinov, R. Size Effects on the Photophysical Properties of Colloidal Anatase TiO_2 Particles: Size Quantization or Direct

Transitions in This Indirect Semiconductor? *J. Phys. Chem.* **1995**, *99*, 16646–16654.

(136) Zhai, H. J.; Wang, L. S. Probing the Electronic Structure and Band Gap Evolution of Titanium Oxide Clusters $(TiO_2)_n^-$ (n = 1-10) Using Photoelectron Spectroscopy. *J. Am. Chem. Soc.* **2007**, *129*, 3022–3026.

(137) Foltin, M.; Stueber, G. J.; Bernstein, E. R. On the Growth Dynamics of Neutral Vanadium Oxide and Titanium Oxide Clusters. *J. Chem. Phys.* **1999**, *111*, 9577–9586.

(138) Heald, L. F.; Garcia, J. M.; Sayres, S. G. Oxygen Deficiencies in Titanium Oxide Clusters as Models for Bulk Defects. **2021**, https://doi.org/10.33774/chemrxiv-2021-rj9cs.

(139) Matsuda, Y.; Bernstein, E. R. On the Titanium Oxide Neutral Cluster Distribution in the Gas Phase: Detection through 118 Nm Single-Photon and 193 Nm Multiphoton Ionization. *J. Phys. Chem. A* **2005**, *109*, 314–319.

(140) Berardo, E.; Hu, H. S.; Shevlin, S. A.; Woodley, S. M.; Kowalski, K.; Zwijnenburg, M. A. Modeling Excited States in TiO_2 Nanoparticles: On the Accuracy of a TD-DFT Based Description. *J. Chem. Theory Comput.* **2014**, *10*, 1189–1199.

(141) Qu, Z. W.; Kroes, G. J. Theoretical Study of the Electronic Structure and Stability of Titanium Dioxide Clusters $(TiO_2)_n$ with n = 1-9. *J. Phys. Chem. B* **2006**, *110*, 8998–9007.

(142) Ganguly Neogi, S.; Chaudhury, P. Structural, Spectroscopic Aspects, and Electronic Properties of $(TiO_2)_n$ Clusters: A Study Based on the Use of Natural Algorithms in Association with Quantum Chemical Methods. *J. Comput. Chem.* **2014**, *35*, 51–61.

(143) Marom, N.; Kim, M.; Chelikowsky, J. R. Structure Selection Based on High Vertical Electron Affinity for TiO_2 Clusters. *Phys. Rev. Lett.* **2012**, *108*, 106801.

(144) Li, S.; Dixon, D. A. Molecular Structures and Energetics of the $(TiO_2)_n$ (n = 1-4) Clusters and Their Anions. *J. Phys. Chem. A* **2008**, *112*, 6646–6666.

(145) Lamiel-Garcia, O.; Cuko, A.; Calatayud, M.; Illas, F.; Bromley, S. T. Predicting Size-Dependent Emergence of Crystallinity in Nanomaterials: Titania Nanoclusters: Versus Nanocrystals. *Nanoscale* **2017**, *9*, 1049–1058.

(146) Calatayud, M.; Maldonado, L.; Minot, C. Reactivity of $(TiO_2)_n$ Clusters (n = 1-10): Probing Gas-Phase Acidity and Basicity Properties. *J. Phys. Chem. C* **2008**, *112*, 16087–16095.

(147) Weichman, M. L.; Song, X.; Fagiani, M. R.; Debnath, S.; Gewinner, S.; Schöllkopf, W.; Neumark, D. M.; Asmis, K. R. Gas Phase Vibrational Spectroscopy of Cold $(TiO_2)_n^-$ (n = 3–8) Clusters. *J. Chem. Phys.* **2016**, *144*, 124308.

(148) Jeong, K. S.; Chang, C.; Sedlmayr, E.; Sülzle, D. Electronic Structure Investigation of Neutral Titanium Oxide Molecules Ti_xO_Y. *J. Phys. B At. Mol. Opt. Phys.* **2000**, *33*, 3417–3430.

(149) Kasha, M. Characterization of Electronic Transitions in Complex Molecules. *Discuss. Faraday Soc.* **1950**, *9*, 14–19.

(150) Berardo, E.; Hu, H. S.; Van Dam, H. J. J.; Shevlin, S. A.; Woodley, S. M.; Kowalski, K.; Zwijnenburg, M. A. Describing Excited State Relaxation and Localization in TiO_2 Nanoparticles Using TD-DFT. *J. Chem. Theory Comput.* **2014**, *10*, 5538–5548.

(151) Peach, M. J. G.; Benfield, P.; Helgaker, T.; Tozer, D. J. Excitation Energies in Density Functional Theory: An Evaluation and a Diagnostic Test. *J. Chem. Phys.* **2008**, *128*, 044118.

(152) Valero, R.; Morales-Garciá, Á.; Illas, F. Investigating the Character of Excited States in TiO_2 Nanoparticles from Topological Descriptors: Implications for Photocatalysis. *Phys. Chem. Chem. Phys.* **2020**, *22*, 3017–3029.

(153) Mewes, S. A.; Plasser, F.; Krylov, A.; Dreuw, A. Benchmarking Excited-State Calculations Using Exciton Properties. *J. Chem. Theory Comput.* **2018**, *14*, 710–725.

(154) Rana, T. H.; Kumar, P.; Solanki, A. K.; Skomski, R.; Kashyap, A. Ab-Initio Study of Free Standing TiO_2 Clusters: Stability and Magnetism. In *Journal of Applied Physics*; **2013**; *113*, 17–526.

(155) Peng, W. T.; Fales, B. S.; Shu, Y.; Levine, B. G. Dynamics of Recombination: Via Conical Intersection in a Semiconductor Nanocrystal. *Chem. Sci.* **2018**, *9*, 681–687.

(156) Frischorn, C.; Wolf, M. Femtochemistry at Metal Surfaces: Nonadiabatic Reaction Dynamics. *Chemical Reviews*. **2006**, 4207–4233.

(157) Pontius, N.; Lüttgens, G.; Bechthold, P. S.; Neeb, M.; Eberhardt, W. Size-Dependent Hot-Electron Dynamics in Small Pd_n^- Clusters. *J. Chem. Phys.* **2001**, *115*, 10479–10483.

(158) Pontius, N.; Bechthold, P. S.; Neeb, M.; Eberhardt, W. Time-Resolved Photoelectron Spectra of Optically Excited States in Pd_3^-. *J. Electron Spectros. Relat. Phenomena* **2001**, *114–116*, 163–167.

(159) Pontius, N.; Bechthold, P. S.; Neeb, M.; Eberhardt, W. Ultrafast Hot-Electron Dynamics Observed in Pt_3^- Using Time-Resolved Photoelectron Spectroscopy. *Phys. Rev. Lett.* **2000**, *84*, 1132–1135.

(160) Heinzelmann, J.; Koop, A.; Proch, S.; Ganteför, G. F.; Łazarski, R.; Sierka, M. Cage-Like Nanoclusters of ZnO Probed by Time-Resolved Photoelectron Spectroscopy and Theory. *J. Phys. Chem. Lett.* **2014**, *5*, 2642–2648.

(161) Koyasu, K.; Braun, C.; Proch, S.; Ganteför, G. The Metal-Semiconductor Transition Monitored by Excited State Lifetimes of $Al_4O_m^-$ Clusters. *Appl. Phys. A Mater. Sci. Process.* **2010**, *100*, 431–436.

(162) Garcia, J. M.; Sayres, S. G. Increased Excited State Metallicity in Neutral Cr_2O_n Clusters (n < 5) upon Sequential Oxidation. *J. Am. Chem. Soc.* **2021**, *143*, 15572–15575.

(163) Guo, Y.; Li, J. F.; Niu, X.; Markovits, A.; Zhang, R. Q. Composition Dependent Reactivity of Titanium Oxide Clusters. *Phys. Chem. Chem. Phys.* **2016**, *18*, 10594–10599.

(164) Koch, D.; Manzhos, S. On the Charge State of Titanium in Titanium Dioxide. *J. Phys. Chem. Lett.* **2017**, *8*, 1593–1598.

(165) Fazio, G.; Ferrighi, L.; Di Valentin, C. Photoexcited Carriers Recombination and Trapping in Spherical vs Faceted TiO_2 Nanoparticles. *Nano Energy* **2016**, *27*, 673–689.

(166) Müller, G. M.; Walowski, J.; Djordjevic, M.; Miao, G. X.; Gupta, A.; Ramos, A. V; Gehrke, K.; Moshnyaga, V.; Samwer, K.; Schmalhorst, J.; et al. Spin Polarization in Half-Metals Probed by Femtosecond Spin Excitation. *Nat. Mater.* **2009**, *8*, 56–61.

(167) Heffernan, K. H.; Yu, S.; Deckoff-Jones, S.; Zhang, X.; Gupta, A.; Talbayev, D. Role of Spin Fluctuations in the Conductivity of CrO_2. *Phys. Rev. B* **2016**, *93*, 165143.

(168) Solovyev, I. V; Kashin, I. V; Mazurenko, V. V. Mechanisms and Origins of Half-Metallic Ferromagnetism in CrO_2. *Phys. Rev. B - Condens. Matter Mater. Phys.* **2015**, *92*, 144407.

(169) Coey, J. M. D.; Venkatesan, M. Half-Metallic Ferromagnetism: Example of CrO_2 (Invited). *J. Appl. Phys.* **2002**, *91*, 8345–8350.

(170) Leo, T.; Kaiser, C.; Yang, H.; Parkin, S. S. P.; Sperlich, M.; Güntherodt, G.; Smith, D. J. Sign of Tunneling Magnetoresistance in CrO2-Based Magnetic Tunnel Junctions. *Appl. Phys. Lett.* **2007**, *91*, 252506.

(171) Singh, A.; Voltan, S.; Lahabi, K.; Aarts, J. Colossal Proximity Effect in a Superconducting Triplet Spin Valve Based on the Half-Metallic Ferromagnet CrO_2. *Phys. Rev. X* **2015**, *5*, 1–6.

(172) Guo, F.; Zhang, N.; Jin, W.; Chang, J. Model of Ultrafast Demagnetization Driven by Spin-Orbit Coupling in a Photoexcited Antiferromagnetic Insulator Cr_2O_3. *J. Chem. Phys.* **2017**, *146*, 244502.

(173) Paul, S.; Misra, A. Magnetic Properties of $Cr_2O_n^-$ Clusters: A Theoretical Study. *J. Mol. Struct. THEOCHEM.* **2009**, *895*, 156–160.

(174) Tono, K.; Terasaki, A.; Ohta, T.; Kondow, T. Chemically Induced Ferromagnetic Spin Coupling: Electronic and Geometric Structures of Chromium-Oxide Cluster Anions, $Cr_2O_n^-$ (n= 1-3), Studied by Photoelectron Spectroscopy. *J. Chem. Phys.* **2003**, *119*, 11221–11227.

(175) Reddy, B.; Khanna, S.; Ashman, C. Oscillatory Magnetic Coupling in Cr_2O_n (N=1-6) Clusters. *Phys. Rev. B - Condens. Matter Mater. Phys.* **2000**, *61*, 5797–5801.

(176) Gutsev, G. L.; Bozhenko, K. V; Gutsev, L. G.; Utenyshev, A. N.; Aldoshin, S. M. Transitions from Stable to Metastable States in the Cr_2O_n and $Cr_2O_n^-$ Series, n = 1-14. *J. Phys. Chem. A.* **2017**, *121*, 845–854.

(177) Zhai, H. J.; Wang, L. S. Probing the Electronic Properties of Dichromium Oxide Clusters Cr_2O_n- (n=1-7) Using Photoelectron Spectroscopy. *J. Chem. Phys.* **2006**, *125*, 164315.

(178) Tono, K.; Terasaki, A.; Ohta, T.; Kondow, T. Chemical Control of Magnetism: Oxidation-Induced Ferromagnetic Spin Coupling in the Chromium Dimer Evidenced by Photoelectron Spectroscopy. *Phys. Rev. Lett.* **2003**, *90*, 13, 1-4.

(179) Zhang, Q. Q.; Zhao, Y.; Gong, Y.; Zhou, M. Matrix Isolation Infrared Spectroscopic and Theoretical Study of Dinuclear Chromium Oxide Clusters: Cr_2O_n (n = 2, 4, 6) in Solid Argon. *J. Phys. Chem. A.* **2007**, *111*, 9775–9780.

(180) Bondybey, V. E.; English, J. H. Electronic Structure and Vibrational Frequency of Cr_2. *Chem. Phys. Lett.* **1983**, *94*, 443–447.

(181) Veliah, S.; Xiang, K. H.; Pandey, R.; Recio, J. M.; Newsam, J. M. Density Functional Study of Chromium Oxide Clusters: Structures, Bonding, Vibrations, and Stability. *J. Phys. Chem. B* **1998**, *102*, 1126–1135.

(182) Pham, L. N.; Claes, P.; Lievens, P.; Jiang, L.; Wende, T.; Asmis, K. R.; Nguyen, M. T.; Janssens, E. Geometric Structures and Magnetic Interactions in Small Chromium Oxide Clusters. *J. Phys. Chem. C* **2018**, *122*, 27640–27647.

(183) Sala, V. G.; Dal Conte, S.; Miller, T. A.; Viola, D.; Luppi, E.; Véniard, V.;

Cerullo, G.; Wall, S. Resonant Optical Control of the Structural Distortions That Drive Ultrafast Demagnetization in Cr_2O_3. *Phys. Rev. B.* **2016**, *94*, 014430, 1-6.

(184) Satoh, T.; Van Aken, B. B.; Duong, N. P.; Lottermoser, T.; Fiebig, M. Ultrafast Spin and Lattice Dynamics in Antiferromagnetic Cr_2O_3. *Phys. Rev. B - Condens. Matter Mater. Phys.* **2007**, *75,* 155406, 1-6.

(185) Moriyama, R.; Sato, R.; Nakano, M.; Ohshimo, K.; Misaizu, F. Geometrical Structures of Gas Phase Chromium Oxide Cluster Anions Studied by Ion Mobility Mass Spectrometry. *J. Phys. Chem. A* **2017**, *121*, 5605–5613.

(186) Wang, X.; Neukermans, S.; Vanhoutte, F.; Janssens, E.; Verschoren, G.; Silverans, R. E.; Lievens, P. Stability Patterns and Ionization Potentials of Cr_nO_m Clusters (n = 3 - 50, m = 0, 1, 2). *Appl. Phys. B Lasers Opt.* **2001**, *73*, 417–423.

(187) Morisato, T.; Jones, N. O.; Khanna, S. N.; Kawazoe, Y. Stable Aluminum and Chromium Oxide Clusters as Precursors to Nanoscale Materials. In *Computational Materials Science*; **2006**; *35*, 366–370.

(188) Molek, K. S.; Reed, Z. D.; Ricks, A. M.; Duncan, M. A. Photodissociation of Chromium Oxide Cluster Cations. *J. Phys. Chem. A* **2007**, *111*, 8080–8089.

(189) Aubriet, F.; Muller, J. F. About the Atypical Behavior of CrO_3, MoO_3, and WO_3 during Their UV Laser Ablation/Ionization. *J. Phys. Chem. A* **2002**, *106*, 6053–6059.

(190) Zhou, M.; Andrews, L. Infrared Spectra and Density Functional Calculations of the CrO_2^-, MoO_2^-, and WO_2^- Molecular Anions in Solid Neon. *J. Chem. Phys.* **1999**, *111*, 4230–4238.

(191) Wang, Y.; Gong, X.; Wang, J. Comparative DFT Study of Structure and Magnetism of TM_nO_m (TM = Sc-Mn, n = 1-2, m = 1-6) Clusters. *Phys. Chem. Chem. Phys.* **2010**, *12*, 2471–2477.

(192) Huang, D. J.; Jeng, H. T.; Chang, C. F.; Guo, G. Y.; Chen, J.; Wu, W. P.; Chung, S. C.; Shyu, S. G.; Wu, C. C.; Lin, H. J.; et al. Orbital Magnetic Moments of Oxygen and Chromium in CrO_2. *Phys. Rev. B - Condens. Matter Mater. Phys.* **2002**, *66*, 1–5.

(193) Kumari, I.; Gupta, S.; Goel, N. A DFT Based Investigation of NO Oxidation by $(CrO_3)_3$ Cluster. *Comput. Theor. Chem.* **2016**, *1091*, 107–114.

APPENDIX A

PERMISSION TO REPRODUCE PORTIONS OF CHAPTER 5

Authors do **not** need permission from AIP Publishing to:

- quote from a publication (please include the material in quotation marks and provide the customary acknowledgment of the source)

- reuse any materials that are licensed under a Creative Commons CC BY license (please format your credit line: "Author names, Journal Titles, Vol.#, Article ID#, Year of Publication; licensed under a Creative Commons Attribution (CC BY) license.")

- reuse your own AIP Publishing article in your thesis or dissertation (please format your credit line: "Reproduced from [FULL CITATION], with the permission of AIP Publishing")

APPENDIX B

PERMISSION TO REPRODUCE PORTIONS OF CHAPTER 6